



MINISTÉRIO DA CIÊNCIA, TECNOLOGIA, INOVAÇÕES E COMUNICAÇÕES
INSTITUTO NACIONAL DE PESQUISAS ESPACIAIS

sid.inpe.br/mtc-m21c/2019/08.28.23.03-TDI

**A 40-YEAR PERSPECTIVE ON THE CONTRIBUTION
OF OBSERVATIONS TO FORECAST ERROR
REDUCTION**

Fábio Luiz Rodrigues Diniz

Doctorate Thesis of the Graduate
Course in Meteorology, guided
by Drs. Dirceu Luis Herdies,
and Ricardo Todling, approved in
August 26, 2019.

URL of the original document:

<<http://urlib.net/8JMKD3MGP3W34R/3TTLN6B>>

INPE
São José dos Campos
2019

PUBLISHED BY:

Instituto Nacional de Pesquisas Espaciais - INPE
Gabinete do Diretor (GBDIR)
Serviço de Informação e Documentação (SESID)
CEP 12.227-010
São José dos Campos - SP - Brasil
Tel.:(012) 3208-6923/7348
E-mail: pubtc@inpe.br

**BOARD OF PUBLISHING AND PRESERVATION OF INPE
INTELLECTUAL PRODUCTION - CEPPII (PORTARIA N°
176/2018/SEI-INPE):****Chairperson:**

Dra. Marley Cavalcante de Lima Moscati - Centro de Previsão de Tempo e Estudos
Climáticos (CGCPT)

Members:

Dra. Carina Barros Mello - Coordenação de Laboratórios Associados (COCTE)
Dr. Alisson Dal Lago - Coordenação-Geral de Ciências Espaciais e Atmosféricas
(CGCEA)
Dr. Evandro Albiach Branco - Centro de Ciência do Sistema Terrestre (COCST)
Dr. Evandro Marconi Rocco - Coordenação-Geral de Engenharia e Tecnologia
Espacial (CGETE)
Dr. Hermann Johann Heinrich Kux - Coordenação-Geral de Observação da Terra
(CGOBT)
Dra. Ieda Del Arco Sanches - Conselho de Pós-Graduação - (CPG)
Sílvia Castro Marcelino - Serviço de Informação e Documentação (SESID)

DIGITAL LIBRARY:

Dr. Gerald Jean Francis Banon
Clayton Martins Pereira - Serviço de Informação e Documentação (SESID)

DOCUMENT REVIEW:

Simone Angélica Del Ducca Barbedo - Serviço de Informação e Documentação
(SESID)
André Luis Dias Fernandes - Serviço de Informação e Documentação (SESID)

ELECTRONIC EDITING:

Ivone Martins - Serviço de Informação e Documentação (SESID)
Cauê Silva Fróes - Serviço de Informação e Documentação (SESID)



MINISTÉRIO DA CIÊNCIA, TECNOLOGIA, INOVAÇÕES E COMUNICAÇÕES
INSTITUTO NACIONAL DE PESQUISAS ESPACIAIS

sid.inpe.br/mtc-m21c/2019/08.28.23.03-TDI

**A 40-YEAR PERSPECTIVE ON THE CONTRIBUTION
OF OBSERVATIONS TO FORECAST ERROR
REDUCTION**

Fábio Luiz Rodrigues Diniz

Doctorate Thesis of the Graduate
Course in Meteorology, guided
by Drs. Dirceu Luis Herdies,
and Ricardo Todling, approved in
August 26, 2019.

URL of the original document:

<http://urlib.net/8JMKD3MGP3W34R/3TTLN6B>

INPE
São José dos Campos
2019

Cataloging in Publication Data

Diniz, Fábio Luiz Rodrigues.

D615f A 40-year perspective on the contribution of observations to forecast error reduction / Fábio Luiz Rodrigues Diniz. – São José dos Campos : INPE, 2019.

xxx + 112 p. ; (sid.inpe.br/mtc-m21c/2019/08.28.23.03-TDI)

Thesis (Doctorate in Meteorology) – Instituto Nacional de Pesquisas Espaciais, São José dos Campos, 2019.

Guiding : Drs. Dirceu Luis Herdies, and Ricardo Todling.

1. Numerical weather prediction. 2. Data assimilation.
3. Observation impact. I.Title.

CDU 551.509.313.3



Esta obra foi licenciada sob uma Licença [Creative Commons Atribuição-NãoComercial 3.0 Não Adaptada](https://creativecommons.org/licenses/by-nc/3.0/).

This work is licensed under a [Creative Commons Attribution-NonCommercial 3.0 Unported License](https://creativecommons.org/licenses/by-nc/3.0/).

Aluno (a): **Fábio Luiz Rodrigues Diniz**

Título: "A 40-YEAR PERSPECTIVE ON THE CONTRIBUTION OF OBSERVATIONS TO FORECAST ERROR REDUCTION"

Aprovado (a) pela Banca Examinadora em cumprimento ao requisito exigido para obtenção do Título de **Doutor(a)** em

Meteorologia

Dr. José Antonio Aravéquia



Presidente / INPE / Cachoeira Paulista - SP

Participação por Vídeo - Conferência

Aprovado Reprovado

Dr. Dirceu Luis Herdies



Orientador(a) / INPE / Cachoeira Paulista - SP

Participação por Vídeo - Conferência

Aprovado Reprovado

Dr. Ricardo Todling

p/ 

Orientador(a) / NASA / Greenbelt - EUA

Participação por Vídeo - Conferência

Aprovado Reprovado

Dra. Simone Marilene Sievert da Costa Coelho



Membro da Banca / INPE / Cachoeira Paulista - SP

Participação por Vídeo - Conferência

Aprovado Reprovado

Dr. Pedro Leite da Silva Dias

p/ 

Convidado(a) / USP / São Paulo - SP

Participação por Vídeo - Conferência

Aprovado Reprovado

Dr. Fabrício Pereira Harter



Convidado(a) / UFPEL / Pelotas - RS

Participação por Vídeo - Conferência

Aprovado Reprovado

Este trabalho foi aprovado por:

maioria simples

unanimidade

*“I’m a greater believer in luck,
and I find the harder I work
the more I have of it.”*

THOMAS JEFFERSON

*To my parents, for their love, endless support and encouragement
throughout my life and to my wife, Aline, for the same.*

ACKNOWLEDGEMENTS

First, I would like to thank my two advisors, Dr. Dirceu L. Herdies and Dr. Ricardo Todling, for their support, guidance, and enthusiasm. I am grateful to them for allowing me to work on this thesis, and also grateful for the opportunity to have been associated with both of them. I would like also to thank the committee members: Dr. Fabrício P. Harter, Dr. José A. Aravéquia, Dr. Pedro L. da Silva Dias, and Dr. Simone M. S. C. Coelho; for taking the time to participate in my committee and provide valuable feedback and suggestions.

My thesis work benefited from the United States of America National Aeronautics and Space Administration (NASA) Global Modeling and Assimilation Office (GMAO) group effort in keeping a state-of-the-art data assimilation system. I would like to thank Dr. Steven Pawson, Dr. Oreste Reale, Dr. Stephen E. Cohn and the GMAO administrative team, for their support and generosity during my one-year visit at NASA GMAO while most of the results for this thesis have been obtained.

This work has been supported by grants 1474545 and 88881.134472/2016-01 from *Coordenação de Aperfeiçoamento de Pessoal de Nível Superior* (CAPES) of Brazil and 147298/2016-4 from *Conselho Nacional de Desenvolvimento Científico e Tecnológico* (CNPq) of Brazil. Support was also provided through the NASA's Modeling, Analysis and Prediction (MAP) program. The computational work was carried out on the Linux Discover Cluster through cooperation with the NASA Center for Climate Simulation (NCCS) at Goddard Space Flight Center (GSFC).

Last, but not least, I thank all of my family and many friends for providing constant support and encouragement.

Thank you very much!

ABSTRACT

Operational and quasi-operational weather prediction centers have been routinely assessing the contribution from various observing systems to reducing errors in short-range forecasts for a number of years now. The original technique, Forecast Sensitivity Observation Impact (FSOI), involves definition of a forecast error measure and evaluation of sensitivities with respect to changes in the observations that require adjoint operators of both the underlying tangent linear model and corresponding analysis technique. The present work applies FSOI to reanalysis and aims at providing an expanded view of the contribution of various observing systems over nearly 40 years of assimilation. Specifically, this study uses MERRA-2 given that its supporting software includes all ingredients necessary to calculate FSOI. Part of this work shows how the quality of forecasts improves over the course of the reanalysis, and examines forecast sensitivities relevant to FSOI. The global assessment here finds, for example, that: conventional observations are a major player in reducing forecast error throughout the 40 years of reanalysis, even when their volume reduces from 45% in the earlier periods to about 5% in the modern era; satellite radiances, especially microwave instruments, are major contributors to error reduction from the early single platform TIROS-N days to the current multi-platform scenario; though their fractional contribution reduces slightly from the early 2000's onward after the increased availability of wind observation from aircraft and atmospheric motion vector (AMV), and the introduction of GPSRO; infrared instruments play a secondary role to microwave but are significant still, with the peculiar result of fractional impacts contribution from modern hyperspectral instruments being roughly similar to those from early infrared instruments. This work also provides an assessment of these impacts over the Amazon basin. Over this region, under self-verification, forecast errors are found to slightly increase from the early data-sparse days to more recent years, when data dramatically increases. Throughout the reanalysis, satellite radiances dominate in volume, but only in before 1999 they dominate the impacts. Beyond 1999, over 50% of forecast error reduction is associated with conventional observations (radiosondes). AMVs are also found to be large contributors to error reduction, but their contribution reduces in dry periods. In opposition to AMVs, satellite radiances tend to contribute more in the dry season. Results provide motivation for additional conventional observations and the use of all-sky treatment of radiances. The dependence of results on the chosen error measure is emphasized throughout.

Keywords: Numerical weather prediction. Data assimilation. Observation impact.

UMA PERSPECTIVA DE 40 ANOS SOBRE AS CONTRIBUIÇÕES DAS OBSERVAÇÕES À REDUÇÃO DOS ERROS DAS PREVISÕES

RESUMO

Centros de previsão de tempo operacionais e quase-operacionais tem avaliado rotineiramente a contribuição de vários sistemas de observação para reduzir os erros das previsões de curto prazo há vários anos. A técnica original, denominada Impacto Observação Sensibilidade Previsão (FSOI), envolve a definição de uma medida de erro de previsão e a avaliação das sensibilidades com relação às condições iniciais e observações, as quais requerem operadores adjuntos de ambos: o modelo linear tangente e a técnica de análise correspondente. O presente trabalho aplica a técnica FSOI em uma reanálise e visa fornecer uma perspectiva da contribuição de vários sistemas de observação ao longo de quase 40 anos de assimilação. Especificamente, este estudo utiliza o MERRA-2, uma vez que seus utilitários incluem todos os ingredientes necessários para calcular a técnica FSOI. Parte deste trabalho mostra como a qualidade das previsões melhora ao longo da reanálise, e examina as sensibilidades das previsões relevantes para a técnica FSOI. A avaliação global aqui encontra, por exemplo, que: as observações convencionais são as mais importantes na redução dos erros de previsão ao longo dos 40 anos de reanálise, mesmo quando o seu volume diminui de 45% nos períodos iniciais para aproximadamente 5% na era moderna; radiâncias de satélites, especialmente instrumentos de microondas, são os principais contribuidores para a redução de erros desde a época da plataforma única TIROS-N até o atual cenário de multiplataformas; embora sua contribuição fracional diminua ligeiramente a partir do início dos anos 2000, após o aumento da disponibilidade de observação de vento de aviões e de Vetores de Movimento Atmosférico (AMVs) e a introdução das observações de Radio Ocultação do Sistema de Posicionamento Global (GPSRO); instrumentos infravermelho desempenham um papel secundário com relação aos instrumentos de microondas, mas ainda assim significativos, com o resultado peculiar da contribuição dos impactos fracionais dos instrumentos hiperespectrais modernos ser semelhante aos dos primeiros instrumentos infravermelho. Este trabalho também fornece uma avaliação desses impactos sobre a bacia amazônica. Nesta região, os erros de previsão aumentam ligeiramente desde os primeiros dias, os quais eram esparsos de dados até o período mais recente, quando os dados aumentam dramaticamente. Ao longo da reanálise, radiâncias de satélite dominam em volume, porém somente dominam os impactos antes no período prévio à 1999. A partir dos anos 2000, mais de 50% da redução dos erros das previsões está associada às observações convencionais (principalmente radiossondas). AMVs também são considerados grandes contribuidores para a redução dos erros, porém sua contribuição apresenta sazonalidade, reduzindo sua contribuição nos períodos secos. Ao contrário dos AMVs, as radiâncias de satélites tendem a contribuir mais durante a estação seca. Os resultados fornecem motivação para adição de observações convencionais e o tratamento das radiâncias por meio da técnica todo-o-céu (do inglês *all-sky*). A dependência dos resultados à medida de erro escolhida é enfatizada.

Palavras-chave: Previsão numérica de tempo. Assimilação de dados. Impacto das observações.

LIST OF FIGURES

	<u>Page</u>	
1.1	<p>Twelve-month running mean anomaly correlations of 3- (blue), 5- (red), 7- (green) and 10-day (yellow) 1200 UTC forecasts of 500 hPa geopotential height for the extratropical Northern (thick line) and Southern Hemispheres (thin line) from (a) ECMWF operational system from January 1980 to May 2013 and (b) two ECMWF reanalysis (ERA) datasets, the ERA-Interim (colored) from January 1979 to April 2013 and the ERA-40 (grey) from January 1973 to December 2001. The shading shows the difference in scores between the two hemispheres at the forecast ranges indicated. The units are %.</p>	3
2.1	<p>Schematic of the observation impact procedure. Relevant times in procedure are: analysis time (t_a), background time (t_b), and forecast verification time (t_v).</p>	14
2.2	<p>Schematic representation of a data assimilation scheme and its Forecast Sensitivity Observation Impact (FSOI) tool.</p>	15
2.3	<p>The (a) fractional and its (b) accumulated vertical mid-layer weights based on mass ($\Delta\sigma$, thin continuous curve) and on height (Δz, thick continuous curve). The dotted vertical line indicates the 72 model levels. All calculated at a point where $p_s = 1000$ hPa and model-top pressure is 0.01 hPa. Values of $\Delta\sigma$ and Δz are similar to those presented in Figure 1 of Errico (2007) and Figure 2 of Todling (2013). The units of fractional weight are %.</p>	17
2.4	<p>Timeline of the studies introducing the main variations of approaches for FSOI.</p>	18
2.5	<p>Time series of $e_a - e_b$ (Δe, dark solid line) and corresponding adjoint-based observation impact estimate (δe, grey solid line) calculated for the global domain in (a, left) for June and (b, right) for December of 2002. The units are J kg^{-1}.</p>	20

2.6	Summed global observation impact (δe , negative values) and observation counts (positive values) for June and December 2002, partitioned by instrument type. Includes all observations assimilated at 0000 UTC. The key is as follows: ATOVS temperature retrievals; RAOB, rawinsondes; SATW, cloud and feature-track winds; AIRW, commercial aircraft observations; LAND, land surface observations; SHIP, ship surface observations; AUSN, synthetic sea level pressure data (Southern Hemisphere only).	20
3.1	Time series of monthly mean stacked observation count (top) and its fractional (bottom) for 0000 UTC analyses during months of January and July. The scale factor for observation count is 10^6 and the units for fractional observation count are %. Numerical values in the legends represent the mean value of a given observation category over the course of its availability. The vertical shaded and non-shaded areas represent the four streams of MERRA-2. Numerical values in the legend represent mean. Observation count is similar, but not identical to Figure 1 of McCarty et al. (2016).	24
3.2	Spatial distribution of observations at 0001 UTC of 1 January 1980 (top) and 1 January 2018 (bottom).	29
4.1	Time series of 30- (violet) and 24-h (green) forecast errors, nonlinear (red) and linear (orange) impact estimates and the count of used observations (yellow, right axis). Lines represent monthly mean values with ± 1 standard deviation from the mean in shading for 0000 UTC analyses during months of January and July. The vertical shaded and non-shaded areas represent the four streams of MERRA-2. Numerical values in the legend represent mean ± 1 standard deviation in addition to the Pearson's correlation between linear and nonlinear impacts and its ratio. For reference, the time series of monthly averaged 500 hPa geopotential height anomaly correlations is also shown (grey curve) with scales on the far right vertical axis (%). The units of energy are J kg^{-1} and the scale factor for observation count is 10^6	39

4.2	Time series of (a) 30- (violet) and 24-h (green) forecast errors regionally partitioned into Northern Hemisphere Extratropics (NHX, thick), Southern Hemisphere Extratropics (SHX, thin), and Tropics (TRP, dashed), plotted in the form of annual running means. Values plotted for January (July) are averages over that month and the preceding July (January). The shading shows the differences in scores between the two extratropical hemispheres. The vertical shaded and non-shaded areas represent the four streams of MERRA-2. Numerical values in the legend represent mean ± 1 standard deviation. The units of energy are J kg^{-1}	42
4.3	Eighteen-year averaged 24-hour vertically integrated energy in forecast sensitivities for January [top: (a) and (b)] and July [bottom: (c) and (d)] over the pre-EOS [1982-1999; left: (a) and (c)] and the EOS [2000-2017; right: (b) and (d)] eras. The scale factor is 10^{-3} and the units are J kg^{-1}	44
4.4	As in Figure 4.2 (page 42), but for nonlinear impacts.	45
4.5	As in Figure 4.2 (page 42), but for linear impacts.	46
4.6	Heatmap of monthly mean total observation impact for each assimilated variable type. Values are for 0000 UTC analyses during months of January and July. Patched boxes represent monthly mean values with ± 3 standard deviations from the total mean impact displayed in the figure and dots represent boxes with negative values. The units are J kg^{-1}	47
4.7	As in Figure 4.6 (page 47), but for fractional of beneficial observations. The units are %	48
4.8	Total impact during the pre-EOS (1982-1999, light grey bars) and EOS (2000-2017, dark grey bars) eras. The numbers on the right vertical axis represent fractional of beneficial observations. Note that there are no bending angle observations in the pre-EOS era. The units of total impact are J kg^{-1} and of beneficial impact are %	49
4.9	As in Figure 4.6 (page 47), but for the major observing systems assimilated in MERRA-2. The categories presented here are the same used in Figure 3.1 (page 24).	50
4.10	As in Figure 4.9 (page 50), but for fractional of beneficial observations. The units are %	51
4.11	Fractional impact during January of 1989. The horizontal axis represents fractional impact; the right vertical axis indicates fraction of beneficial observations for each category. The units of fractional and beneficial impacts are %	53
4.12	As in Figure 4.11 (page 53), but for January of 2015. For reference, the fractional impact for GEOS FP is also shown (dark grey bars).	54

4.13	Heatmap of monthly mean impact per observation for Conventional, Aircraft, AMV and Surface Wind observations presented in Figure 3.1 (page 24) during the pre-EOS era (1980-1999). The Conventional category is split into three subcategories: Surface, Drifting Buoy, Upper-Air, and MLS; the Aircraft into two: Manual and Automated; the AMV into two: Geostationary and Polar; and the Surface Wind into five: SSM/I & SSMIS, ERS & ERS-2, QuikSCAT, WindSat and ASCAT. Values are for 0000 UTC analyses during months of January and July. Patched boxes represent monthly mean values with ± 3 standard deviations from the total mean impact displayed in the figure and dots represent boxes with negative values. The scale factor is 10^{-5} and the units are J kg^{-1}	55
4.14	As in Figure 4.13 (page 55), but for the EOS era (2000-2017).	56
4.15	Monthly mean vertical profiles of total impact [left: (a) and (c)] and standard deviation [right: (b) and (d)] of observation-minus-background (OmB) residuals for temperature [top: (a) and (b)] and zonal wind component [bottom: (c) and (d)]. The column on the right represents mean number of observations per analysis in each layer. The units of energy are J kg^{-1} and of standard deviation of temperature and zonal wind component are K and m s^{-1} , respectively.	59
4.16	Vertical profiles of estimates of background (green and black) and observation (blue and red) error standard deviations for (a) temperature and (b) zonal wind obtained from the radiosondes during the pre-EOS (1982-1999; red and black) and the EOS (2000-2017; blue and green) eras. Lines represent mean values with ± 1 standard deviation from the mean in shading for 0000 UTC analyses during months of January and July. The column on the right represents mean number of observations per analysis in each layer for the pre-EOS era and in parenthesis the difference subtracting EOS from pre-EOS era. The dots represent the statistical significance between the eras. The units of standard deviation of temperature and zonal wind component are K and m s^{-1} , respectively.	60
4.17	Vertical profiles of estimates of Kalman gain, $\sigma_b^2/(\sigma_b^2 + \sigma_o^2)$, in observation-space for radiosonde residuals of (a) temperature and (b) zonal wind obtained for the 0000 UTC analyses of the January and July months of the pre-EOS (1982-1999; red) and the EOS (2000-2017; blue) eras. Curves represent mean values; shading represents ± 1 standard deviation from the mean. The column on the right represents mean number of observations per cycle in a particular layer for the pre-EOS era and in parenthesis the differences from the pre-EOS era.	62

4.18	Monthly mean fractional observation impact for all radiance grouped as satellite platforms. Only results for 0000 UTC analyses during months of January and July are included. The line represents the sum of all bubble values for each month. The size of the bubbles is proportional to the monthly mean observation count for each partition of the observing system. The units of fractional observation impact are %.	63
4.19	As in Figure 4.18 (page 63), but for sensors. The size of the bubbles is proportional to the inverse of the observation error variance assigned before the assimilation for each partition of the observing system. The units of fractional observation impact are % and of the inverse of the observation error variance are K^{-2} .	65
4.20	As in Figure 4.6 (page 47), but for all GPSRO observations grouped as satellite platforms.	66
4.21	Vertical profile of mean (red, bottom axis) and standard deviation (blue, bottom axis) of fractional observation-minus-background (OmB) residuals, and mean observation impact (bars, top axis). Lines (bars) represent mean values with ± 1 standard deviations from the mean in shading (whiskers) for 0000 UTC analyses during months of January and July. The column on the right represents mean number of observations per analysis in each layer. The units of mean and standard deviation of fractional background residuals are % and of energy are $10^{-3} J kg^{-1}$.	68
4.22	As in Figure 4.18, but for various sources of wind observations. The thin light grey curve represents the sum of fractional impact from all wind observation sources. The thick dark grey curve adds the contribution from GPSRO to those of wind observations.	70
5.1	Time series of 24-h forecast errors in the Northern Hemisphere Extratropics (north of $20^{\circ}N$; thick continuous line), Southern Hemisphere Extratropics (south of $20^{\circ}S$; thin continuous line), Tropics (between $20^{\circ}S$ and $20^{\circ}N$; dashed line), and Amazon basin (dotted line). Lines represent monthly mean values during January and July. The shading shows the differences in scores between the two extratropical hemispheres. Values are plotted in the form of annual running means, resulting in that values plotted for January (July) are averages over that month and the preceding July (January), and, as a consequence, we omit values for January 1980 for consistency with the whole time series. The units of energy are $J kg^{-1}$.	74
5.2	As in Figure 5.1 (page 74), but for linear impacts.	75

5.3	As in Figure 5.2 (page 75), but only the Tropics (between 20°S and 20°N; dashed line), and the Amazon basin (dotted line).	76
5.4	Time series of the monthly mean stacked observation count (top) and corresponding fractional count (bottom) for the 0000 UTC MERRA-2 analyses during January and July over the Amazon basin. The scale factor for observation count is 10^6 , and the units for fractional counts are %. Numerical values in the legends are the mean non-scaled number of observations and the mean fractional counts during the availability of each observing system. The vertical shaded and non-shaded areas separate the four streams of MERRA-2.	77
5.5	Eighteen-year averaged 24-hour vertically integrated energy in forecast sensitivities for January [top: (a) and (b)] and July [bottom: (c) and (d)] over the pre-EOS [1982-1999; left: (a) and (c)] and the EOS [2000-2017; right: (b) and (d)] eras. The Amazon basin is represented by polygons in black contour. The scale factor is 10^{-3} and the units of energy are J kg^{-1}	79
5.6	Time series of the monthly mean total impacts for all observations over the Amazon basin, grouped according to classes presented in Figure 5.4 (page 77). The grey line represent the sum of all bubble values for each month and is referred to as the dotted line in Figures 5.2 and 5.3 (pages 75 and 76, respectively), with a single modification related to the moving average that is not being applied here. The size of the bubbles is proportional to the monthly mean observation count for each partition of the observing system. The units of total impact are J kg^{-1}	81
5.7	As in Figure 5.6 (page 81), but for fractional impacts. The grey line represent the sum of all bubble values for each month. The units of fractional impacts are %.	82
5.8	Time series of the monthly mean number of radiosonde reports per analysis at 0000 UTC in the Northern Hemisphere Extratropics (north of 20°N; thick continuous line), Southern Hemisphere Extratropics (south of 20°S; thin continuous line), Tropics (between 20°S and 20°N; dashed line), and Amazon basin (dotted line). Lines represent monthly mean values during January and July. Only reports including temperature are account for.	83
5.9	As in Figure 5.8 (page 83), but only the Tropics (between 20°S and 20°N; dashed line) and the Amazon basin (dotted line).	84
5.10	As in Figure 5.8 (page 83), but only the Amazon basin.	84

5.11	Barplot of monthly mean observation counts for January (orange) and July (blue) during the EOS era (2000-2017). The scale factor for observation count is 10^6	85
5.12	As in Figure 5.11 (page 85), but for total impact. The units of total impact are J kg^{-1}	87
5.13	Vertical profile of mean (continuous line, bottom axis) and standard deviation (dashed line, bottom axis) of fractional observation-minus-background (OmB) residuals, and total impact (bars, top axis) for GP-SRO observations over the Amazon basin. Values represent 13-year average, from 2005 to 2017, during January. The whiskers correspond to the standard error of the mean with 95% confidence intervals calculated using the standard deviation as in Figure 5.12. The column on the right represents mean number of observations per analysis in each layer. The units of mean and standard deviation of fractional OmB residuals are % and of total impact and their standard errors are 10^{-3}J kg^{-1}	88
5.14	As in Figure 5.13 (page 88), but for July.	89

LIST OF TABLES

	<u>Page</u>
3.1 Production dates of the four streams of MERRA-2.	26
3.2 Boxes corners of the defined regions and the main chapters in which they are used.	28
3.3 Dates of observation data types assimilated in MERRA-2. Underlined rows refer to instruments not considered in this study.	30
3.4 Descriptions of the main abbreviated observation categories.	32
3.5 As in Table 3.4 (page 32), but for brightness temperature (T_b) variable obtained through radiance satellites.	33
3.6 As in Table 3.4 (page 32), but for brightness temperature (T_b) variable obtained through radiance sensors.	34
3.7 Nominal channel selections for satellite radiances according to each sensor presented in Table 3.6 (page 35). Channels in bold denote those that are assimilated without any bias correction (only AMSU-A, ATMS, and SSU) and underlined channels were used through 31 July 2012 (only CrIS). . .	35

LIST OF ABBREVIATIONS

3D-Var	–	Three-Dimensional Variational
4D-Var	–	Four-Dimensional Variational
4D-EnVar	–	Four-Dimensional Ensemble-Variational
ADAS	–	Atmospheric Data Assimilation System
AGCM	–	Atmospheric Global Circulation Model
AM	–	Before Midday, from Latin <i>Ante Meridiem</i>
ATMS	–	Advanced Technology Microwave Sounder
AIRS	–	Atmospheric Infrared Sounder
AMSU-A	–	Advanced Microwave Sounding Unit-A
AMSU-B	–	Advanced Microwave Sounding Unit-B
AMV	–	Atmospheric Motion Vector
AOD	–	Aerosol Optical Depth
ASCAT	–	Advanced Scatterometer
ATOVS	–	Advanced TIROS-N Operational Vertical Sounder
CHAMP	–	Challenging Minisat Payload
C/NOFS	–	Communications/Navigation Outage Forecasting System
COSMIC	–	Constellation Observing System for Meteorology, Ionosphere & Climate
CrIS	–	Cross-track Infrared Sounder
CTRM	–	Community Radiative Transfer Model
DA	–	Data Assimilation
DAS	–	Data Assimilation System
EC	–	Environment Canada
DFS	–	Degrees of Freedom for Signal
DMSP	–	Defense Meteorological Satellite Program
MeteoSat	–	Meteorological Satellite
ECCC	–	Environment and Climate Change Canada
ECMWF	–	European Centre for Medium-Range Weather Forecasts
EFSOI	–	Ensemble Forecast Sensitivity Observation Impact
EMC	–	Environmental Modeling Center
EnDA	–	Ensemble Data Assimilation
EnSRF	–	Ensemble Square-Root Filter
EOS	–	Earth Observing System
ERA5	–	ECMWF Reanalysis 5
ERA-40	–	ECMWF Reanalysis-40
ERA-Interim	–	ECMWF Reanalysis-Interim
ERS	–	European Remote Sensing
ERS-2	–	European Remote Sensing-2
ESMF	–	Earth System Modeling Framework
ESS	–	Earth and Space Science

FP	– Forward Processing
FSOI	– Forecast Sensitivity Observation Impact
GCM	– General Circulation Model
Geo	– Geostationary
GEOS	– Goddard Earth Observing System
GFS	– Global Forecasting System
GMAO	– Global Modeling and Assimilation Office
GOCART	– Goddard Chemistry, Aerosol, Radiation, and Transport
GOES	– Geostationary Operational Environmental Satellite
GOS	– Global Observing System
GPS	– Global Positioning System
GPSRO	– Global Positioning System Radio Occultation
GRACE-A	– Gravity Recovery and Climate Experiment–A
GSI	– Gridpoint Statistical Interpolation
HIRS	– High-resolution Infrared Radiation Sounder
HIRS-2	– High-resolution Infrared Radiation Sounder-2
HIRS-3	– High-resolution Infrared Radiation Sounder-3
HIRS-4	– High-resolution Infrared Radiation Sounder-4
IASI	– Infrared Atmospheric Sounding Interferometer
IAU	– Incremental Analysis Update
IFS	– Integrated Forecasting System
IR	– Infrared
JCSDA	– Joint Center for Satellite Data Assimilation
JPSS	– Joint Polar Satellite System
MERRA	– Modern-Era Retrospective Analysis for Research and Applications
MERRA-2	– MERRA, version 2
MERRAero	– MERRA Aerosol Reanalysis
MERRA-Land	– MERRA Land Reanalysis
MHS	– Microwave Humidity Sounder
MLS	– Microwave Limb Sounder
MSU	– Microwave Sounding Unit
MetOp-A	– Meteorological Operational A series
MetOp-B	– Meteorological Operational B series
MW	– Microwave
NASA	– National Aeronautics and Space Administration
NCEP	– National Centers for Environmental Prediction
NHX	– Northern Hemisphere Extratropics
NOAA	– National Oceanic and Atmospheric Administration
NRL	– Naval Research Laboratory
NWP	– Numerical Weather Prediction
OmA	– Observation-minus-Analysis

OmB	– Observation-minus-Background
OSE	– Observing System Experiment
OSSE	– Observing System Simulation Experiment
OSTIA	– Operational Sea Surface Temperature and Sea Ice Analysis
PM	– Past Midday, from Latin <i>Post Meridiem</i>
QJRMS	– Quarterly Journal of the Royal Meteorological Society
QuikSCAT	– Quick Scatterometer
SAC-C	– Scientific Application Satellite-C
SEVIRI	– Spinning Enhanced Visible Infra-Red Imager
SSM/I	– Special Sensor Microwave Imager
SSMIS	– SSM/I and Sounder
SHX	– Southern Hemisphere Extratropics
SSU	– Stratospheric Sounding Unit
TerraSAR-X	– Terra Synthetic Aperture Radar operating in X band
TIROS-N	– Television Infrared Observation Satellite-N
TOVS	– TIROS-N Operational Vertical Sounder
TRP	– Tropics
UTC	– Universal Time Coordinate
WAM	– Whole Atmosphere Model
WIGOS	– WMO Integrated Global Observing System
WindSat	– WindSat Polarimetric Radiometer
WMO	– World Meteorological Organization

CONTENTS

	<u>Page</u>
1 INTRODUCTION	1
1.1 Objectives	6
2 THEORETICAL BACKGROUND	9
2.1 Observation impact on the forecast	9
3 METHODS AND DATA	21
3.1 Methods	21
3.1.1 Modeling framework	21
3.1.1.1 Brief summary of MERRA-2	22
3.1.1.2 Forecast errors and sensitivities in MERRA-2	24
3.1.2 Observation impact in MERRA-2	26
3.1.3 Region definitions	27
3.2 Data	28
3.2.1 Observations	28
4 FSOI APPLICATION TO REANALYSIS	37
4.1 Introduction	37
4.2 Forecast errors and sensitivities	41
4.3 Global perspective	45
4.4 Conventional, Aircraft, AMV and Surface Wind	54
4.5 Radiosonde	57
4.6 Radiance	61
4.7 GPS radio occultation	66
4.8 An interplay of fractional contributions	69
5 FSOI APPLICATION TO REANALYSIS OVER THE AMAZON 71	
5.1 Introduction	71
5.2 Observing system	75
5.3 Forecast sensitivities	78
5.4 FSOI results	80
5.5 Seasonal effect on FSOI	85
6 SUMMARY AND CONCLUSIONS	91

REFERENCES 97

1 INTRODUCTION

The word *assimilation* has a variety of meanings in a variety of sciences (e.g., physics, biological, social), but in every science, assimilation presents the concept of incorporation (LEWIS et al., 2009). In the context of numerical weather prediction (NWP), this concept of incorporation is in the sense of combining data and laws. The way to combine data and laws has been in constant evolution, also the way to obtain the proper data and the way to represent the proper laws. Currently, this incorporation process represents strategies to blend observations with model, commonly known as *data assimilation*, and, as in many branches of science, the increase of computational capacity helped to advance the techniques involved in this process. Recently, these advancements in NWP were classified as a “quiet revolution” in the review article of Bauer et al. (2015), mostly because it happened due to an accumulation of scientific knowledge and technological advances. Such advances turned possible that NWP centers use more and more observations from a variety of observing systems¹. Roughly speaking, the numerical models used to predict the weather have historically evolved from simplified, but consistent, representations of the atmosphere to comprehensive representations, currently known as Earth system models, including interactions between its various components. It started from coupling atmosphere and surface models, both land and marine, to coupling really complex interactions between atmosphere and chemistry models. In parallel, data assimilation has played and still has room to play, an essential role in this evolution transforming what has been used as boundary conditions by simplified models in the historical past of developments to what is currently being used as initial conditions by new components of Earth system models.

Undoubtedly, observations had a good portion of the contribution to our understanding of the structure and dynamics of the Earth system, and consequently providing bases to the development of these modeling systems. Although contributions brought by observations to the developments involved in this evolution are incommensurable, their contributions to generating the initial conditions and subsequent forecasts are not. The traditional longest established way to measure it is through forecast verification of a given metric. An example along the lines of the evolution in NWP over the years can be objectively and quantitatively assessed using forecast skill scores. A typical metric adopted over several years by NWP centers to assess the performance of their systems is the correlation between the forecasts and the

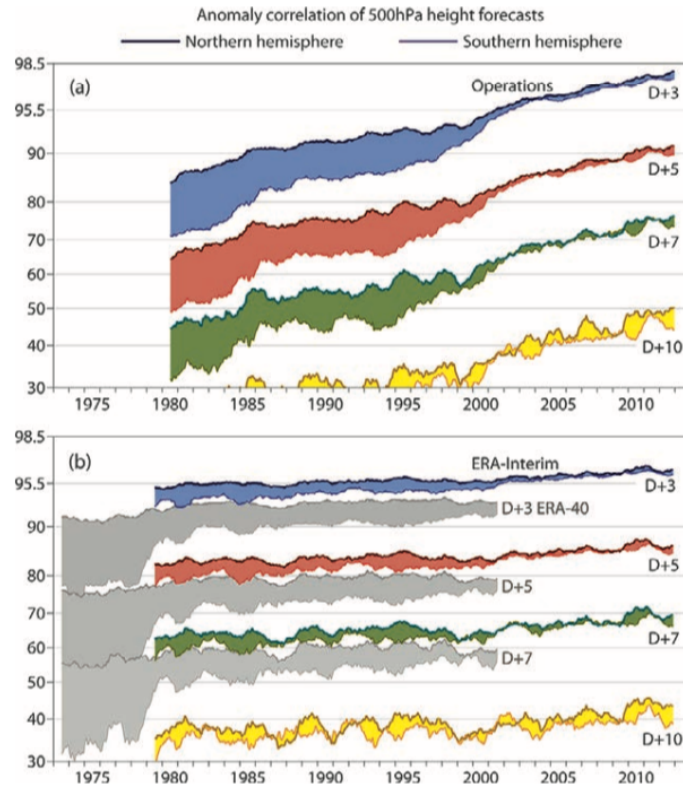
¹We use the definition of *observing system* in this study as an instrument or group of instruments that can be used to generate a set of observational data.

verifying analysis of the geopotential height at the 500 hPa level, expressed as the anomaly with respect to the climatological height. An example of it is presented in the panels of Figure 1.1. This figure is extracted from the work of Dee et al. (2013, Figure 1), but a number of variations of this quantity can be found elsewhere. This figure illustrates the aforementioned measure for various forecast lead times (3-, 5-, 7-, 10-days), from January 1973 to May 2013, averaged for different lead times over the extratropical hemispheres, obtained for the operational system at the European Centre for Medium-Range Weather Forecasts (ECMWF) in panel (a) of Figure 1.1, that is the Integrated Forecasting System (IFS). Over the long-time history presented here, model performance has significantly improved for IFS², reaching unprecedented levels of accuracy. This improvement in forecast skill has been brought by the cumulative improvement of the various components of the IFS, for example: model physics, model dynamics, and data assimilation (e.g., Rabier, 2005). From a data assimilation perspective, the IFS assimilation scheme changed from the optimal interpolation (OI) to the three-dimensional variational (3D-Var) scheme in January 1996 (COURTIER et al., 1998; RABIER et al., 1998; ANDERSSON et al., 1998), and later on from the 3D-Var to the four-dimensional variational (4D-Var) scheme in November 1997 (RABIER et al., 2000; MAHFOUF; RABIER, 2000; KLINKER et al., 2000).

Certainly, changes to the IFS helped the system to better use the available observations, but in addition to it, the observing system has also changed quite a lot throughout the whole time series. ECMWF is one of the few NWP centers that periodically reprocess a long-time history of analyses using a frozen configuration of its operational system — the so-called reanalysis processing. Forecasts for lead times longer than the necessary for the reanalysis production are not a common product in these datasets. However, at ECMWF they are produced in an attempt to obtain a measurement of how newer versions of their systems perform over a long-time history. An example of it is presented in panel (b) of Figure 1.1 for forecasts derived from two versions of ECMWF reanalysis (ERA) datasets: ERA-40 (UPPALA et al., 2005) and ERA-Interim (DEE et al., 2011). It is important to note that the frozen configurations of IFS used to generate each of these reanalyses are closely related to one of the multiple configurations used to create the time series in panel (a) of Figure 1.1. For example, ERA-40 and -Interim were produced using 3D-Var and 4D-Var analysis schemes, respectively. Although not as pronounced as

²The forecast skill score presented on this figure is bounded by -100 to 100%, with a perfect score equal to 100%. There is a consensus in the scientific community that values greater than 60% indicate useful forecasts.

Figure 1.1 - Twelve-month running mean anomaly correlations of 3- (blue), 5- (red), 7- (green) and 10-day (yellow) 1200 UTC forecasts of 500 hPa geopotential height for the extratropical Northern (thick line) and Southern Hemispheres (thin line) from (a) ECMWF operational system from January 1980 to May 2013 and (b) two ECMWF reanalysis (ERA) datasets, the ERA-Interim (colored) from January 1979 to April 2013 and the ERA-40 (grey) from January 1973 to December 2001. The shading shows the difference in scores between the two hemispheres at the forecast ranges indicated. The units are %.



SOURCE: Dee et al. (2013).

in the IFS curves, the forecast skill of reanalyses also improved throughout its time series. Common in both panels of Figure 1.1 is the convergence of the curves for the extratropical hemispheres about late 1990's and early 2000's. The convergence of the curves is even better noticed for shorter leading times, indicating the benefit brought by observations for short-range forecasts. The forecast skill presented in panel (b) of Figure 1.1 clears out changes due to the system, being affected only by changes in the observing system, allowing one to associate changes in forecast skill with, for example, the introduction of new observing systems (e.g., advanced satellite instruments). It is also important to note that these changes in skill are

related to the set of observations being used all at once when producing the initial conditions from where forecasts were issued. This holds even when new observing systems take place. In other words, improvements (or degradation) in forecast skill are due to the new observing systems in the presence of all other observations. Although the major changes in the observing system are well known, it is difficult to attribute improvements (or degradation) in forecast skill to a specific observing system mostly due to two main reasons: (i) the need to find a relationship between changes in the forecast with changes in the initial conditions; and later on how these changes in initial conditions are related to changes in observations. In science generally and NWP specifically, it is extremely valuable to know the sensitivity of a model's output to changes in model's inputs. These reasons are typically studied in terms of sensitivity analysis experiments, having its origins in trial experiments. This kind of experiment is a central problem in predictability studies that involve forecast impact. A lot of effort has been done on this research area focusing on how initial condition perturbations evolve in time, mostly motivated by the systematic theoretical study of forecast error growth performed by [Lorenz \(1965\)](#).

One possible approach to obtain forecast sensitivity is to measure changes in a forecast aspect that result from systematically perturbing any degree of freedom in the initial condition. This leads to an infinity of solutions, being impossible to obtain. In practice, what is commonly performed is to define a finite set of perturbations in the initial conditions and evaluate how the forecast aspect of each perturbed forecast performs with respect to a non-perturbed forecast. These perturbations can be inserted explicitly in the initial conditions. Nonetheless, data assimilation systems provide an environment to perturb the initial conditions through the usage of observations. This can be done in a variety of ways, but the simplest, in agreement with the aforementioned possibility of perturbing any degree of freedom in the initial condition, is perturbing each observation. Leading again to an infinity of solutions and impossible to obtain. The forecast sensitivity obtained using these procedures is related to the introduced perturbations and provides an understanding about the “consequences” of the introduced perturbations. However, what one could be interested in extract from forecast sensitivity is to obtain an understanding of the “causes” that led to a forecast aspect. During many years, sensitivity methods have been exploited in the NWP context with the goal of identifying dynamic links in evolving weather patterns. This kind of estimate has been extensively investigated during the 1990's and 2000's in a variety of field campaigns aiming to find regions where would be beneficial to add extra observations (e.g., deployment of dropsondes) — the so-called targeted observations. The article of [Majumdar \(2016\)](#) provides an

overview about the variety of available strategies adopted over the years. Among those, an efficient method of obtaining this kind of estimate is through the usage of the so-called adjoint models, which are built on adjoint operators that determine sensitivities at the initial time related to all possible perturbations in the initial condition.

If the forecast models are used to step perturbations forward in time, one can say that the adjoint models are used to step sensitivities backward in time. A number of studies have demonstrated how the adjoint models can be used to provide a gradient of some aspect of the forecast to a change in the initial conditions (e.g., Errico and Vukicevic, 1992; Rabier et al., 1996). This procedure helps to solve the problem stated in reason (i) above, but still remains to find a relationship between the changes (perturbations) initial conditions are related to changes in observations. A similar solution can be used for reason (ii). Although not backward in time as the aforementioned adjoint associated with the forecast model, the adjoint of the analysis scheme can also be explained as backward procedures. If the data assimilation scheme is able to map the contribution of the observations to the initial conditions of the forecast model, one can say that its adjoint is able to map perturbations in the initial conditions back to the observations. The desire in obtain a measure diagnosing impacts from observations is closely linked to forecast verification. The combinations of the adjoints of the forecast model and analysis scheme may be used together to objectively determine the contribution brought by observations to numerical weather forecasts — the so-called observation impact. The term *observation impact* can be used in many different contexts. In this study, we use this term referring to how much a NWP forecast is changed due to the observations assimilated. The observation impact is a very specific measure of forecast impact, as it depends upon the choice of forecast metrics, the suite of observations assimilated, the data assimilation system, and the NWP forecast model. The work of Langland and Baker (2004) can be considered the seminal study efficiently attributing to each assimilated observation its contribution in reducing a forecast-error aspect, using the adjoints of the forecast model and data assimilation scheme. This has been introduced under the nomenclature of adjoint-based procedure to observation impact, and later has been termed in different ways³. Currently, this procedure is commonly known as Forecast Sensitivity Observation Impact (FSOI) and this nomenclature will be

³This procedure can be found over the literature under different acronyms, for example: Forecast Sensitivity to Observations (FSO: Cardinali (2009a), Cardinali (2009b)); Forecast Error Contribution (FEC: Cardinali and Prates (2011)); Forecast Error Reduction (FER: Cardinali and Healy (2014)); Forecast Sensitivity approach to Observation Impact (FSOI: Lupu et al. (2015)).

adopted throughout this document. In this study, these adjoints are used to efficiently estimate the reductions of a forecast-error measure due to arbitrary sets of observations used by the data assimilation system.

1.1 Objectives

The present thesis aims to understand the impact of observations on short-range forecasts in the broader context of yearly to decadal time scales of reanalysis, being explored through a state-of-the-art modeling framework using a robust method capable of obtaining a quantitative measurement of the contribution of the observations to reduce forecasts errors. Specifically, this thesis is conducted for the following purposes:

- a) Analyse the observation impact technique applied to a multi-year reanalysis;
- b) Investigate the forecast skill in the light of the observation impact metrics, as a corroboration to forecasts results from other reanalysis using different metrics;
- c) Investigate the contributions from various observing system components in reducing forecast errors along the reanalysis period;
- d) Obtain a quantitative estimate of the contribution of new observing systems to reanalysis forecasts;
- e) Evaluate the contribution of the so-called conventional observations;
- f) Evaluate the contribution of radiance instruments and how they evolve in a long-time history;
- g) In the light of the global evaluation, assess the impact of observations in short-range forecasts over the Amazon basin in South America;
- h) Identify an overview of the evolution of the global observing system.

In order to achieve the objectives proposed here, this document is organised as follows: Chapter 2 provides the theoretical background information necessary to understand the issues addressed in this thesis; Chapter 3 describes the methods and data used; Chapters 4 and 5 refer to results and discussions; and finally, we summarise the work conducted in this thesis and draw conclusions in Chapter 6,

including suggestions for further work that could be carried out following on from work conducted to date.

This thesis is a contribution to observation impact studies, being a unique study in the sense that this is the first study assessing observation impacts in a multi-year reanalysis framework, using the [Langland and Baker \(2004\)](#) approach. The results are segregated into two chapters. Preliminary results of Chapter 4 are already published in the Joint Center for Satellite Data Assimilation (JCSDA) Newsletter, [Diniz and Todling \(2019b\)](#), and an article is under minor revision by the Quarterly Journal of the Royal Meteorological Society (QJRMS), [Diniz and Todling \(2019a\)](#). Another article, presenting results of Chapter 5, has been submitted for the Earth and Space Science (ESS), [Diniz et al. \(2019\)](#).

2 THEORETICAL BACKGROUND

This chapter aims to provide the theoretical background of particular importance to this thesis. It gives a brief general overview of the fundamental processes involved in the estimation of observation impact on short-range forecasts, in the context of NWP, focusing on the FSOI technique. It presents the connection to the primary studies found over the literature. Additional specific background information is presented in the following chapters of this document. For simplicity and ease of understanding, the modeling framework adopted in this chapter uses a general nonlinear forecast model with a linear analysis scheme providing the initial conditions for this model. This choice does not deter the extendability of the introduced fundamentals to specific frameworks.

2.1 Observation impact on the forecast

It is the desire to forecast with accuracy, which demands a better usage of the available resources. The contribution that observing systems have in NWP systems is a so important theme that the World Meteorological Organization (WMO) frequently promotes a workshop designed to draw conclusions concerning the contributions of the various components of the observing system to forecast skill at short and medium range (e.g., the reports of Pailleux, 1997; Pailleux and Böttger, 2000; Böttger et al., 2004; Pailleux et al., 2008; Andersson and Sato, 2012; and Sato and Riishojgaard, 2016). The workshop is designed to discuss the major topics on this theme, for global and regional applications, encouraging the scientific community to present the latest results assessing observation impacts and also to monitor the WMO Global Observing System (GOS). This series of workshops helps data providers and users to measure the current value to NWP of different observing systems, according to the ability of each application in effectively extracting useful information from observations, providing some guidance for future developments. According to the last report of this series, there is a clear trend throughout the NWP centers toward monitoring the GOS with advanced tools.

The assessment of contributions from observations to analysis and forecasts is a challenging diagnostic in NWP. As briefly introduced in Chapter 1, a possible approach to estimate impact of observations on forecasts, is to systematically run a NWP system for a prolonged period perturbing the set of observations, then verify forecast against a reference the skill of the forecast. Historically, the traditional techniques used in this assessing was (and still is) the so-called Observing System Experiment (OSE) and Observing System Simulation Experiment (OSSE). [Atlas](#)

(1997) provides an overview about this kind of experiment. In OSEs and OSSEs, a data assimilation system and model forecast run is conducted using a baseline set of observations, commonly defined as a *control*, and further runs are done but denying or adding observations — the so-called *data denial* and *data add-on* experiments, respectively — to measure forecast impact through a standard set of verification scores. However, the main difference between them is that OSSE is performed in an idealized environment to simulate different observing systems (e.g., a proposal for a new satellite instrument), while the OSE technique uses the already in place observing systems (e.g., a new instrument which is already on board a satellite). The assessment of the value of a given observing system can become quite expensive if a full investigation of the different components of the GOS is performed. This kind of experiment provides a measure representing what would happen if the NWP system did not have (or did have for the add-on case) the observations selected to be denied (or added). In general it is assumed that a positive impact happens when forecast skill increases, while negative impact when it is reduced, regardless of whether the metric is positive or negative defined. For example, an increase in skill for anomaly correlation is obtained with an increase in its value, while an increase in skill for root-mean-squared error is obtained with a decrease in its value. As this study is focused on deriving observation impacts using the FSOI technique, readers are referred to the study of Daescu (2009) for a comprehensive comparison of OSE and FSOI through a mathematical framework. In addition to it, the study of Gelaro and Zhu (2009) presents a systematical comparison between OSE and FSOI using a robust NWP system. Although both measures obtain an estimate of impact of observations on forecast, these techniques are found to complement the results from each other.

As briefly introduced in Chapter 1, the FSOI represents a technique that uses both adjoints (forecast model and analysis scheme) to obtain a measure of how much each assimilated observation helped change a given forecast aspect. The adjoint-based method was introduced by Langland and Baker (2004) in a observation space variational data assimilation system. Interpretations of some basic properties of the method are described in Errico (2007), Gelaro et al. (2007), Trémolet (2007), and Daescu and Todling (2009). Adaptation of the method to model space variational data assimilation systems is described in Trémolet (2008). Zhu and Gelaro (2008) and Cardinali (2009b) present results applying this technique for 3D-Var and 4D-Var systems, respectively. Errico (2007), Gelaro et al. (2007), and Trémolet (2008) treated cross terms among observations as second-order effects. It is possible that bad observations could alter the estimated impacts of nearby good observations,

or vice versa, mostly due to the nonlinearity involved on the process. [Ishibashi \(2011\)](#) studied the cross terms between observation impacts of different datasets, showing that these cross terms between neighboring channels of satellite radiance observations are not negligible.

[Baker and Daley \(2000\)](#) derived the equations of the forecast sensitivity to observations and the background state in terms of the adjoint of the data assimilation system. Subsequently, these techniques have been extended to incorporate the forecast error sensitivity to observation and background error covariances. [Daescu \(2008\)](#) extended the adjoint-based method to assess forecast sensitivity with respect not only to observations, but to observation-error and background-error covariance matrices. The study provides a theoretical framework to diagnose the impact of for further diagnostic tool development not only to evaluate the observation impact on the forecast but also the impact of the other analysis parameters. This method was latter applied by [Daescu and Todling \(2010\)](#), [Daescu and Langland \(2013\)](#), [Cardinali and Healy \(2014\)](#), and [Lupu et al. \(2015\)](#) to optimize the usage of error covariance matrices. The FSOI technique was also applied to an ensemble Kalman filter framework, where adjoint operators are approximated by ensemble forecasts. This was first proposed by [Liu and Kalnay \(2008, see also Li et al., 2010\)](#) in a local ensemble transform Kalman filter environment, presenting promising results when comparing with the traditional adjoint method. Later, the ensemble-based method has been simplified by [Kalnay et al. \(2012\)](#) to any approximation of ensemble Kalman filter. The FSOI variations using ensemble were introduced under the nomenclature of ensemble-based procedure to observation impact, but currently they are known as Ensemble FSOI (EFSOI). [Buehner et al. \(2018\)](#) introduced a variation of the FSOI for hybrid ensemble-variational analysis schemes. The study of [Todling \(2013\)](#) rigorously examined the caveats involved in the FSOI technique introduced by [Langland and Baker \(2004\)](#). In addition to it, the study introduced an alternative to the FSOI estimates using observation-minus-forecasts residuals.

As mentioned in Chapter 1, the present work follows the approach of [Langland and Baker \(2004\)](#) to derive observation impacts. Briefly, the approach requires defining an error measure, e , and obtains observation impacts as the outcome of evaluating how (infinitesimal) changes to the observations change the error measure. The error measure is typically chosen to be a weighted, quadratic, sum of forecast errors calculated with respect to a given verification, that is,

$$e \equiv (\mathbf{x}^f - \mathbf{x}^v)^T \mathbf{P}^T \mathbf{C} \mathbf{P} (\mathbf{x}^f - \mathbf{x}^v), \quad (2.1)$$

where \mathbf{x}^f and \mathbf{x}^v are n -dimensional vectors representing the forecast and verification fields, respectively, \mathbf{C} is a positive definite weighting matrix, \mathbf{P} is a projection operator allowing for confinement of the measure within a desired region, defined 1 in the region of interest and zero elsewhere, and T stands for the transpose operation.

Infinitesimal changes to e can be traced back to changes in the forecast initial condition \mathbf{x}_0 and subsequently to the observations \mathbf{y}^o that lead to a particular initial condition. Specifically, variational calculus allow us to write, the so-called observation impact δe , as in

$$\delta e = \mathbf{d}^T \frac{\partial e}{\partial \mathbf{y}^o} = \mathbf{d}^T \left(\frac{\partial \mathbf{x}_0}{\partial \mathbf{y}^o} \right)^T \left(\frac{\partial \mathbf{x}^f}{\partial \mathbf{x}_0} \right)^T \frac{\partial e}{\partial \mathbf{x}^f} = \mathbf{d}^T \mathbf{K}^T \mathbf{g}, \quad (2.2)$$

with \mathbf{d} being the observation-minus-background (OmB) residual p -dimensional vector, the underlying analysis operator being represented by the matrix \mathbf{K} , and $\mathbf{g} \equiv \left(\frac{\partial \mathbf{x}^f}{\partial \mathbf{x}_0} \right)^T \frac{\partial e}{\partial \mathbf{x}^f}$ amounting to a forecast sensitivity vector whose approximation leads to all kinds of formulae. For example, [Errico \(2007\)](#) shows how the [Langland and Baker \(2004\)](#) formulation can be derived from a Taylor expansion of the differentiation involved in the forecast sensitivity calculation, thus leading to various approximations associated with different levels of truncation in the expansion. While [Daescu and Todling \(2009\)](#) introduce a parametric approach that uses either Taylor series or numerical quadrature methods to obtain various orders of approximations for the observation impacts.

As discussed in [Daescu and Todling \(2009\)](#), the [Langland and Baker \(2004\)](#) formulation corresponds to a second-order approximation of the forecast sensitivity component. This can be written as

$$\mathbf{g} \equiv \frac{1}{2} \left(\mathbf{M}_a^T \mathbf{P}^T \mathbf{C} \mathbf{P} \epsilon_a + \mathbf{M}_b^T \mathbf{P}^T \mathbf{C} \mathbf{P} \epsilon_b \right), \quad (2.3)$$

where the matrix \mathbf{M}^T represents the adjoint of a tangent linear model of the nonlinear model associated with the forecasting model used to obtain \mathbf{x}^f , $\epsilon_f \equiv \mathbf{x}^f - \mathbf{x}^v$ is the forecast error, and the subscripts $f = a$ and $f = b$ correspond to linearization, and error evaluation, of model predictions issued from analysis and corresponding

background states, respectively, as follows:

$$\mathbf{M}_a^T = \left(\frac{\partial \mathbf{x}_a^f}{\partial \mathbf{x}_a} \right)^T, \quad (2.4)$$

and

$$\mathbf{M}_b^T = \left(\frac{\partial \mathbf{x}_b^f}{\partial \mathbf{x}_b} \right)^T. \quad (2.5)$$

As suggested by Trémolet (2008), the impact of observations in a model space variational data assimilation system implemented with several outer loops can be obtained through:

$$\delta e = \sum_{j=1}^J \mathbf{d}_j^T \mathbf{K}_j^T \mathbf{H}_{j+1}^T \mathbf{K}_{j+1}^T \mathbf{z}_{j+1}, \quad (2.6)$$

where J represents the number of outer loops, and $\mathbf{z}_J = \mathbf{g}$. The infinitesimal perturbation representation of observation impact in (2.2) has typically been given the interpretation of being a proxy for a finite perturbation definition of impact described as that improvement (or deterioration) obtained when predicting the state at certain time from two consecutive analyses of a cycling assimilation system. This is illustrated in Figure 2.1. In other words, the infinitesimal perturbation impact δe is equated with the finite perturbation impact Δe as in

$$\delta e \sim \Delta e \equiv e_a - e_b. \quad (2.7)$$

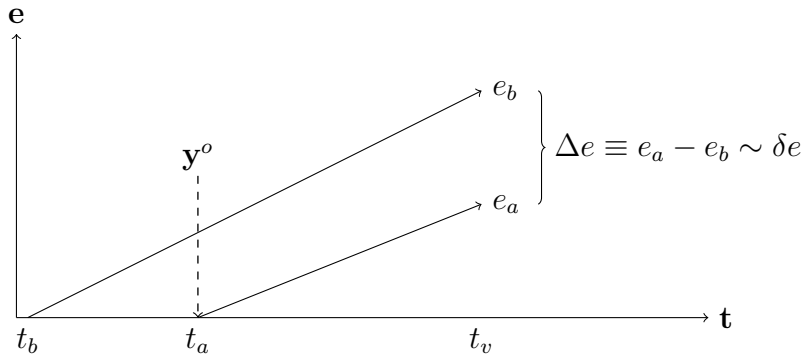
Though Δe can be easily and explicitly calculated, it is not possible to use it to assess the individual contribution from sub-components of the observing system; this is where the infinitesimal representation of impact, δe , becomes handy: expressions following the right-hand side of (2.2) can easily be split into the various components of the observing system. It is pertinent to mention that the ensemble-based observation impact approach of Liu and Kalnay (2008, see also Li et al., 2010) and Kalnay et al. (2012), typically referred to as EFSOI, obtains a direct approximation to the finite perturbation impact Δe , that can just as well be split into the sub-components of the observing system. In other words, FSOI $\sim \Delta e \approx$ EFSOI. This is a subtle point

that has no immediate consequence to comparing FSOI and EFSOI results unless high order terms are sought out in these approximations. The advantage of δe is that it can be split into the sub-components of the observing system by simply noticing that (2.2) can be written as $\delta e = \sum_I \delta e_I$, and that δe_I is given by

$$\delta e_I = \sum_{i=1}^I d_i \tilde{g}_i \quad (2.8)$$

where d_i is the i -th element of the residual vector, $\tilde{g}_i \equiv (\mathbf{K}^T \mathbf{g})_i$ is the i -th element of the analysis sensitivity vector, and I represents any possible partitioning of the background residual vector \mathbf{d} .

Figure 2.1 - Schematic of the observation impact procedure. Relevant times in procedure are: analysis time (t_a), background time (t_b), and forecast verification time (t_v).



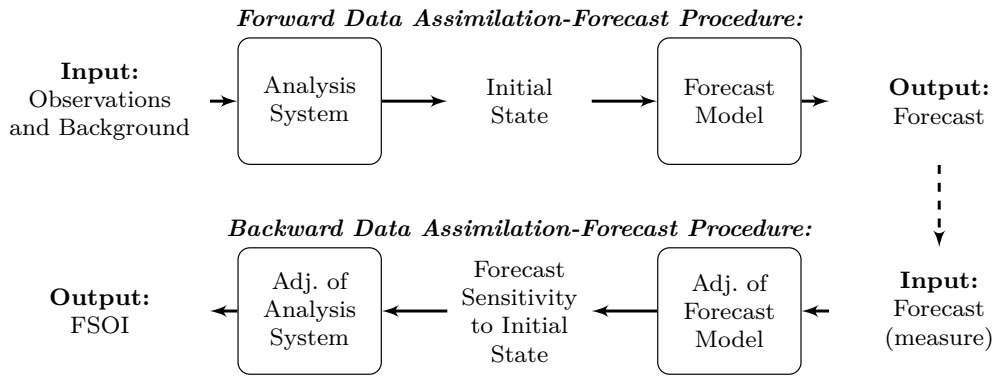
SOURCE: Author's production.

The metric e can be evaluated for any length of forecast, including for a very short-range 6-hour background. In practice, since FSOI typically employs self verification, where \mathbf{x}^v is an analysis obtained with the underlying cycling data assimilation system, the forecast length must be long enough to reduce the effect of spurious correlations affecting the results — see [Todling \(2013\)](#) for an explicit expression for the correlated terms and a discussion of its consequences. At the same time, forecasts cannot be too long in extent since FSOI relies on an infinitesimal perturbation approach and depends on the validity of the tangent linear approximation. As such, it has become typical to evaluate FSOI for 24-hour forecasts. This is the

situation depicted in the finite perturbation illustration of Figure 2.1, when the impact of observations is seen as the difference between the errors on 24- and 30-hour forecasts.

The procedures involved in the FSOI technique are summarized in Figure 2.2. In this figure we show the schematic of the necessary data assimilation procedures involved in FSOI studies. The figure is divided in two main regions. The top row represents the steps involved in a typical data assimilation system when producing analysis — the so-called *forward procedures*. The bottom row represents the steps involved also in a data assimilation system, but when producing sensitivities — the so-called *backward procedures*.

Figure 2.2 - Schematic representation of a data assimilation scheme and its and its Forecast Sensitivity Observation Impact (FSOI) tool.



SOURCE: Author's production.

Also associated with the metric e is the weighting matrix \mathbf{C} . In global applications such as the present one, this is typically chosen to represent a linearized total energy quantity meant to unify the varied units of temperature (T), zonal and meridional horizontal wind components (u and v , respectively), surface pressure (p_s) and specific humidity (q) forming the components of the forecasting and verification vectors, into a single consistent unit, for instance, J kg^{-1} . The typical norm definition adopted in these studies is the total energy norm of Talagrand (1981, see also Lorenz, 1960), being easily calculated and dynamically relevant, as well as comprehensive in that it measures contributions from u , v , T and p_s , augmented by a term accounting for q contribution as in Ehrendorfer et al. (1999), with its continuous formulation being expressed as a symmetric inner-product matrix \mathbf{C} , implemented as an integral of

the total energy over the model horizontal (Σ) and vertical (σ) domains as follows:

$$e = \frac{1}{2} \mathbf{x}^T \mathbf{C} \mathbf{x} = \frac{1}{2} \int_{\Sigma} \int_0^1 \left[u'^2 + v'^2 + \frac{c_{pd}}{T_r} T'^2 + \epsilon_q \frac{L_c^2}{c_{pd} T_r} q'^2 \right] d\sigma d\Sigma + \frac{1}{2} \int_{\Sigma} R_d T_r \left(\frac{p'_s}{p_r} \right)^2 d\Sigma, \quad (2.9)$$

where the prime superscript (\square') represents perturbations, and $c_{pd} = 1004.64 \text{ J K}^{-1} \text{ kg}^{-1}$, $R_d = 287.05 \text{ J K}^{-1} \text{ kg}^{-1}$, $L_c = 2.499 \times 10^6 \text{ J kg}^{-1}$, $T_r = 280 \text{ K}$, and $p_{sr} = 1000 \text{ hPa}$, are the specific heat of dry air at constant pressure, the gas constant for dry air¹, the latent heat of condensation at 273.15 K, and the reference temperature and surface pressure², respectively. The q contribution term involves the ϵ_q parameter³, which defines a relative weight given to the water contribution. When $\epsilon_q \neq 0$ we obtain the moist total energy norm, and when $\epsilon_q = 0$ we obtain the dry total energy norm.

The caveats associated with the choice of the total energy norm for FSOI purposes have been discussed in [Todling \(2013\)](#). One of these relates to the choice of vertical weights used to form the total energy operator: one choice is mass weighting; another, is based on height. The former provides negligibly small weights in the stratosphere (basically above 10 hPa); the latter, provides weights that increase with height about a certain level, thus putting a lot of emphasis on the stratosphere and not much in the troposphere. Neither of these options is quite ideal, though most FSOI works use the mass-weighted option, and as such focus on tropospheric results. An illustration of these choices is shown in [Figure 2.3](#). Alternative weights formed on the basis of the inverse of the observation error covariance matrix used in the analysis procedure have been proposed and examined in [Todling \(2013\)](#); such weights produce impacts treated in a form consistent with how the analysis procedure utilizes the observations; this relates to the approach of degrees of freedom for signal of [Lupu et al. \(2011\)](#). The present work, however, follows the traditional choice of mass-weighted total energy weights, focusing thus on tropospheric contributions from the observing system.

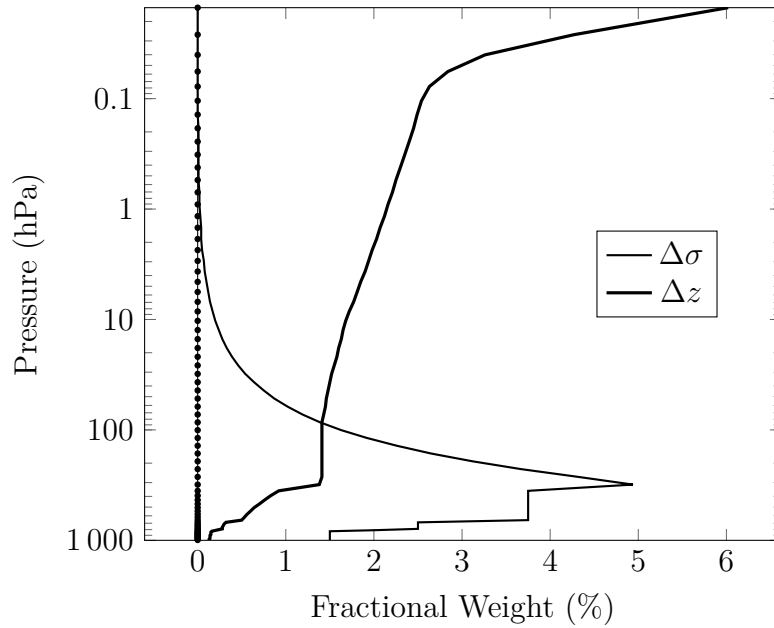
¹Here calculated assuming the universal gas constant $R^* = 8.31447 \times 10^3 \text{ J K}^{-1} \text{ kmol}^{-1}$ and the effective molecular weight of dry air $m_d = 28.965 \text{ kg kmol}^{-1}$.

²According to [Errico et al. \(2007\)](#), these reference values of temperature and surface pressure can be prescribed, location-independent (e.g., mean).

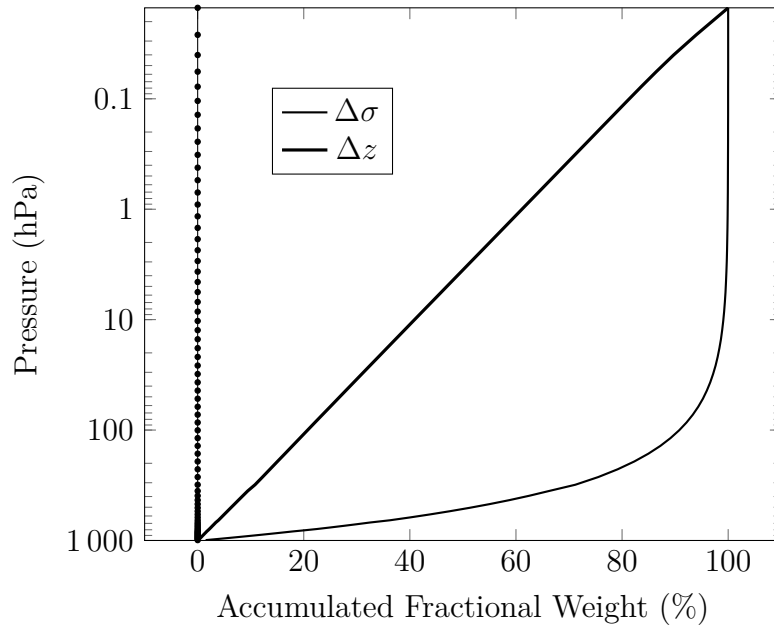
³Also denoted as ω_q over the literature.

Figure 2.3 - The (a) fractional and its (b) accumulated vertical mid-layer weights based on mass ($\Delta\sigma$, thin continuous curve) and on height (Δz , thick continuous curve). The dotted vertical line indicates the 72 model levels. All calculated at a point where $p_s = 1000$ hPa and model-top pressure is 0.01 hPa. Values of $\Delta\sigma$ and Δz are similar to those presented in Figure 1 of Errico (2007) and Figure 2 of Todling (2013). The units of fractional weight are %.

(a)



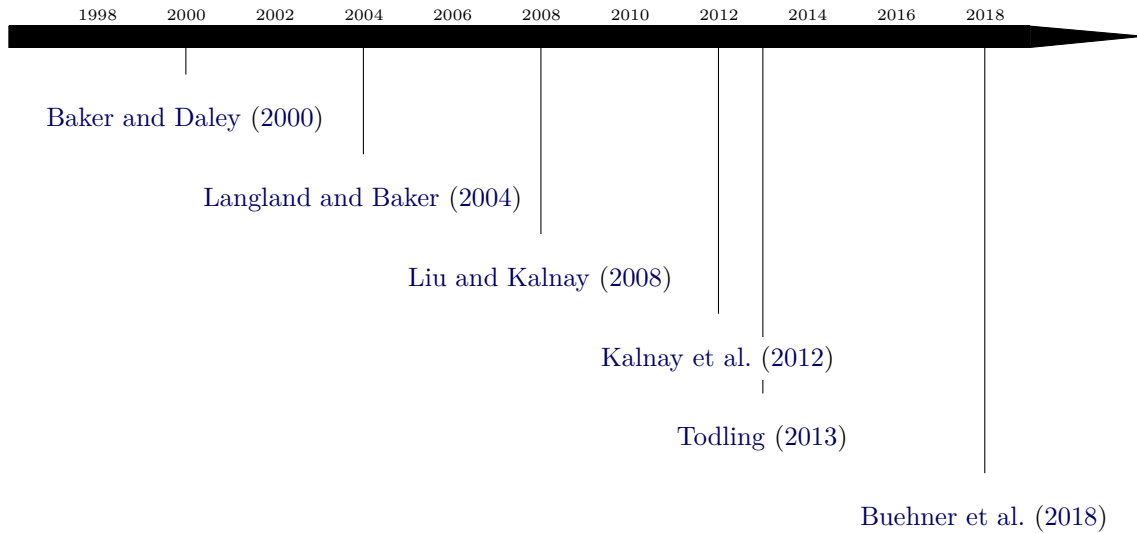
(b)



SOURCE: Author's production.

The abundance of recent studies regarding FSOI applications is too numerous to cover here. Readers are advised to peruse the proceedings of the WMO Workshop on the Impact of Various Observing Systems for a more complete sample in meteorology and related Earth sciences (e.g., the references in the introduction of this chapter). However, a few notable studies should be highlighted to illustrate the main variations of approaches of FSOI. Figure 2.4 presents a timeline of the FSOI studies introducing variations of this technique. We define dates as the year that the research was published. Indeed, developments and discussions started earlier. The omission of studies may reflect the imperfection of this timeline, rather than the intrinsic merit of that study.

Figure 2.4 - Timeline of the studies introducing the main variations of approaches for FSOI.



SOURCE: Author's production.

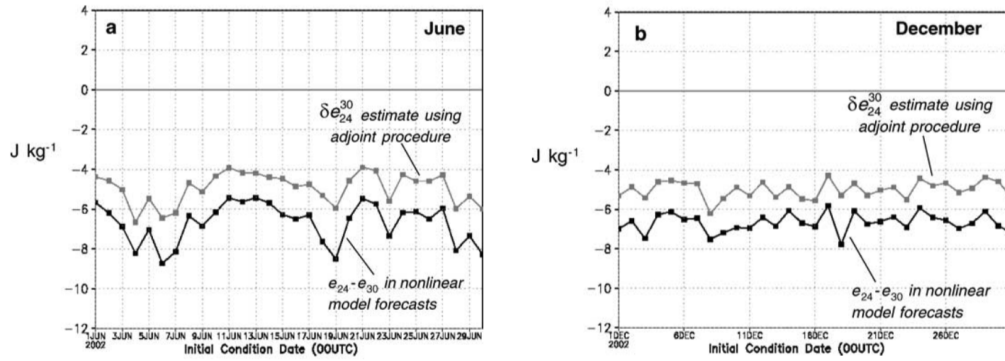
As briefly introduced in Chapter 1, the work of Langland and Baker (2004) can be considered the seminal study related to the FSOI technique. An example of the results obtained by Langland and Baker (2004) is presented here in Figures 2.5 and 2.6. These results are for two single-month periods, namely June and December of 2002. In Figure 2.5, the dark solid line represents the forecast error reduction calculated using Δe , while the grey solid line represents the corresponding adjoint-based observation impact estimate δe ; see (2.7), page 13. It is important notice that the forecast error reduction presents negative values due to e_a being smaller than e_b . This is a clear effect of the benefit that observations brought to the analysis

at time t_a , and as a consequence to the forecasts at time t_v . It is also important notice how the estimate δe follows the variability of Δe . An example of the possible splitting of δe according to the observation categories used to generate the analysis is presented in Figure 2.6. In this figure, grey and dark bars represents results for June and December of 2002, respectively. Positive values represent the observation counts for each category and negative values represent the total impact. The sum of the bars for each period in Figure 2.6 equates with the total impact grey solid line presented in Figure 2.5.

The results of Langland and Baker (2004) encouraged a number of meteorological centers to implement the FSOI technique in its operational systems to routinely diagnose the usage of the observations. As a consequence, this led to the first FSOI intercomparison study, presented in Gelaro et al. (2010), in which were compared FSOI results obtained from three global NWP systems. The three systems were set to use a common set of observations during the month of January 2007. Participated in this intercomparison the systems from: the Naval Research Laboratory (NRL); the National Aeronautics and Space Administration (NASA) Global Modeling Assimilation Office (GMAO); and the Environment Canada (EC). Despite the differences explained in details in Gelaro et al. (2010), it is important to notice the similarity among the three centers. Currently, an extended and update intercomparison of Gelaro et al. (2010) including contributions from additional NWP centers is being spearheaded by the Joint Center for Satellite Data Assimilation (JCSDA)⁴, from December 2014 to February 2015, and the participating NWP centers are (LANGLAND et al., 2016; AULIGNE et al., 2017; MAHAJAN et al., 2018): the NRL (LANGLAND; BAKER, 2004); the GMAO (GELARO et al., 2010); the United Kingdom Met Office (LORENC; MARRIOTT, 2014); the Météo-France (BOULLOT et al., 2016); the Japan Meteorological Agency (JMA) (ISHIBASHI, 2018); and, the Environmental Modeling Center (EMC) of the United States National Center for Environmental Prediction (NCEP) (OTA et al., 2013).

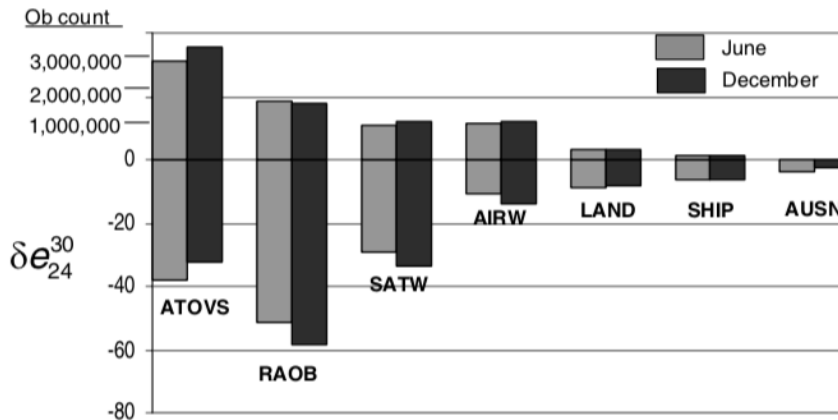
⁴Results for this intercomparison are available online at: <http://ios.jcsda.org>.

Figure 2.5 - Time series of $e_a - e_b$ (Δe , dark solid line) and corresponding adjoint-based observation impact estimate (δe , grey solid line) calculated for the global domain in (a, left) for June and (b, right) for December of 2002. The units are J kg^{-1} .



SOURCE: Langland and Baker (2004).

Figure 2.6 - Summed global observation impact (δe , negative values) and observation counts (positive values) for June and December 2002, partitioned by instrument type. Includes all observations assimilated at 0000 UTC. The key is as follows: ATOVS temperature retrievals; RAOB, rawinsondes; SATW, cloud and feature-track winds; AIRW, commercial aircraft observations; LAND, land surface observations; SHIP, ship surface observations; AUSN, synthetic sea level pressure data (Southern Hemisphere only).



SOURCE: Langland and Baker (2004).

3 METHODS AND DATA

This chapter presents two main sections dedicated to describing the methods (Section 3.1) and data (Section 3.2) used in this thesis.

3.1 Methods

This section describes the modeling framework adopted to obtain the results of this thesis, as well as the specific nomenclature and definition of observation impact measures involved in the present study. Additional information about the particular configuration of the modeling framework used to obtain the results of this thesis is presented in each of the following chapters within the results.

3.1.1 Modeling framework

This study benefited from the NASA Goddard Space Flight Center’s GMAO group and partners’ efforts in developing and maintaining state-of-the-art tools in Earth system modeling and data assimilation. The GMAO uses the Goddard Earth Observing System (GEOS) modeling and data assimilation system to produce estimates of the Earth system state to support NASA’s Earth observation missions and various field campaigns, and as a consequence, the scientific community benefits from it. The GEOS system development is built around the modular concept of the Earth System Modeling Framework (ESMF; Theurich et al., 2016), which allows the system to be easily adapted for various purposes. This enables us to say that GEOS can be considered a *system of subsystems*. As an Earth system model, GEOS presents components for atmospheric and ocean circulation, land surface processes, atmospheric composition, and biogeochemistry. Each of its components can be switched on and off according to its application. This system can be adaptable for a range of applications, from cloud-resolving applications through a global mesoscale model, to a seasonal-to-decadal climate model to perform simulations at coarser resolutions. A broad overview of this system can be found in Rienecker et al. (2008), which provides details and points to references for various components of this system.

The most recent validated version of GEOS runs routinely near-real time at GMAO producing analyses and forecasts, under the name of GEOS Forward Processing (FP). While GEOS FP is under continuous development, with regular updates and upgrades, reflecting the major developments in Earth system modeling, sometimes a clone copy of this system is generated and kept unchanged to reprocess analysis over a historical period. Along the years, this system has been used to generate three

reanalysis datasets: the first, presented in Schubert et al. (1993); second, Modern-Era Retrospective Analysis for Research and Applications (MERRA; Rienecker et al., 2011); and third, the most recent, still running, the MERRA-2 presented in details by Gelaro et al. (2017).

The results of this thesis are based on the MERRA-2 modeling framework. The study of Gelaro et al. (2017) presents an overview of MERRA-2, including a system description and various measures of performance, providing an introduction for a series of studies that evaluate MERRA-2 products and their uses in particular applications. A number of assessments for specific components of the system can be found over the literature, for example: Randles et al. (2017) and Buchard et al. (2017) the aerosol analysis component; Reichle et al. (2017a), Reichle et al. (2017b) and Draper et al. (2018) the process in the land surface component (e.g., precipitation, hydrology, and energy budget); Bosilovich et al. (2017) the global water balance and water cycle variability.

3.1.1.1 Brief summary of MERRA-2

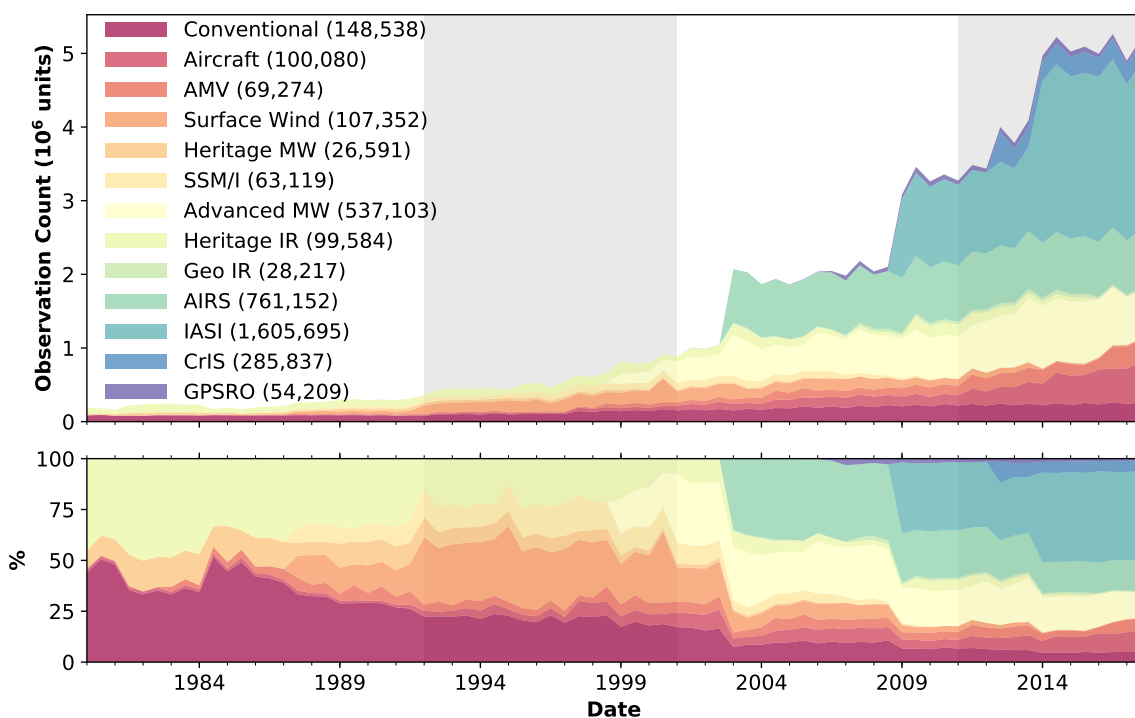
The MERRA-2 is a follow up to MERRA that is primarily aimed at providing an improved water cycle as compared not only to MERRA but also to other available reanalyses. MERRA-2 most distinguishing feature is the use of the dry mass conservation constraint approach of Takacs et al. (2016). MERRA-2 replaces the MERRA 0.5° regular grid finite-volume hydrodynamics of Lin (2004) with a cubed-sphere finite-volume hydrodynamics (PUTMAN; LIN, 2007) at comparable resolution; both operating on 72 hybrid vertical coordinate levels. Additionally, MERRA-2 incorporates a radiatively active Goddard Chemistry, Aerosol, Radiation, and Transport (GOCART; Chin et al., 2002; Colarco et al., 2010) aerosol component that benefits from the assimilation of aerosol optical depth (AOD), and thus represents a step forward into coupling aerosols to the meteorology of reanalysis by integrating the offline MERRAero analysis (BUCHARD et al., 2015) into a full online procedure (RANDES et al., 2017, and references therein), which employs a local displacement ensemble approach to update its corresponding aerosol fields concentration by assimilating AOD through the Physical-space Statistical Analysis System of Randles et al. (2016). Another feature of MERRA-2 is its implementation of a land precipitation correction procedure applied from low- to mid-latitudes that rely on the offline MERRA-Land of Reichle et al. (2017b) and its assimilated precipitation product. The procedure is an attempt to reduce model biases in land precipitation and to ground MERRA-2 to realistic levels of precipitation, especially when affecting aerosol deposition. This

precipitation correction procedure ensures, in particular, that anomalous precipitation events are reasonably well represented in MERRA-2. Other major upgrades in MERRA-2 include: a revised and retuned version of its general circulation model (see Molod et al., 2015, and Cullather et al., 2014); and a revised version of its sea ice concentration and sea surface temperature boundary conditions, this latter relying on a merge of the daily $\frac{1}{4}^\circ$ resolution Reynolds et al. (2007) product from 1982 to March 2006 with the Donlon et al. (2012) $\frac{1}{20}^\circ$ resolution Operational Sea Surface Temperature and Sea Ice Analysis (OSTIA) data set covering the modern period.

Just as in MERRA, the atmospheric analysis uses the Grid-point Statistical Interpolation (GSI), but MERRA-2 incorporates considerable upgrades in its science and software (see Kleist et al., 2009b). Specifically, the MERRA-2 atmospheric analysis relies on an improved version of the Community Radiative Transfer Model (CRTM, release 2.1.3; Han et al., 2006; Chen et al., 2008). Furthermore, the MERRA-2 GSI replaces the weak-constraint balance operator of the MERRA GSI with the strong-constraint tangent linear normal mode formulation of Kleist et al. (2009a) for incremental balance adjustment. The MERRA-2 GSI also invokes the bi-conjugate gradient procedure of El Akkraoui et al. (2013); a three-dimensional variational data assimilation (3D-Var) algorithm incorporates a middle-loop strategy — linearization of the observation operator — with two outer-loops, each with 100 inner iterations. The variational procedure operates at a resolution of 0.5° on 72 vertical hybrid eta levels and uses a first-guess at the appropriate time strategy and a climatological background error covariance derived on the basis of the National Meteorological Center (NMC; now named the NCEP) method (PARRISH; DERBER, 1992), which is unchanged throughout the reanalysis period. The Derber and Wu (1998) variational bias correction procedure is applied to satellite radiance observations, to estimate air-mass and viewing-angle-dependent biases, whereas biases in the scan-angle are estimated offline using an exponential moving average filter applied to the observation-minus-background residuals (R. Treadon, pers. comm.). A cycling offline bias correction procedure is implemented to correct temperature biases in aircraft observations (see Sec. 3.2 of McCarty et al., 2016, for details).

For simplification, the present work calculates observation impacts only for the 0000 UTC analysis cycles, and only for the months of January and July. Consequently, Figure 3.1 counts only observations used at these times over the period from 1980 to 2017 (thus, this is only a *similar* figure to Figure 1 of McCarty et al., 2016, but not identical). Gelaro et al. (2010) provides an understanding for how observation impacts change at different synoptic times in 6-hourly-cycled systems

Figure 3.1 - Time series of monthly mean stacked observation count (top) and its fractional (bottom) for 0000 UTC analyses during months of January and July. The scale factor for observation count is 10^6 and the units for fractional observation count are %. Numerical values in the legends represent the mean value of a given observation category over the course of its availability. The vertical shaded and non-shaded areas represent the four streams of MERRA-2. Numerical values in the legend represent mean. Observation count is similar, but not identical to Figure 1 of [McCarty et al. \(2016\)](#).



SOURCE: Author's production.

such as MERRA-2; typically, the impact of satellite observations is significantly increased at times when the impact-dominating radiosonde network is considerably reduced (i.e., at 0600 and 1800 UTC). As briefly introduced in Section 1.1 (page 6), the objective of the present study is to provide a comprehensive view of the impact of observations in the broader context of yearly to decadal time scales of reanalysis.

3.1.1.2 Forecast errors and sensitivities in MERRA-2

To derive observation impacts following the approach described in the previous chapter requires evaluation of the gradient (2.3), page 12, and thus the availability of 30- and 24-hour forecasts from two consecutive analyses. Forecasts, however, are

not readily available products of MERRA-2, and certainly neither are the forecast sensitivity vectors resulting from the corresponding adjoint operations in (2.3). It is worthwhile noticing that, in situations when forecasts and sensitivities are only derived for the purpose of calculating observation impacts, and forecast are not readily available, the midpoint approximation of [Daescu and Todling \(2009\)](#) provides the same order of accuracy on the impacts at half the cost by referring only to forecasts and model adjoint integrations issued from midpoint initial conditions, defined as half of the sum of the analysis and background fields. The midpoint formulation would have saved us computational resources, however, the desire to examine the long term behavior of the nonlinear impact, derived from the finite perturbation approach (2.7), page 13, motivated us to stick with the traditional [Langland and Baker \(2004\)](#) formulation. The strategy adopted here to reduce cost is to evaluate FSOI for the 0000 UTC analyses. Additionally, FSOI is produced for the months of January and July. Ultimately, 24-hour forecasts were obtained for analyses over each of these times, and 30-hour forecasts were obtained for each of the corresponding preceding 1800 UTC analyses.

All nonlinear forecasts were generated at the full MERRA-2 cubed-sphere horizontal grid resolution of 0.5° , roughly corresponding to 50 km, and with 72 vertical levels with a top pressure at 0.01 hPa. The adjoint model of the forecasting model includes the adjoint of the cubed-sphere hydrodynamical finite-volume core ([Jong Kim, pers. comm.](#)), simple vertical diffusion and boundary layer, and the simplified large-scale moist processes of [Holdaway et al. \(2014\)](#). All versions of the FSOI applications in GEOS ignore the effect of the Incremental Analysis Update (IAU; [Bloom et al., 1996](#)) in the adjoint model integration. Forecast sensitivities are generated on a 1° horizontal grid resolution and the 72 vertical levels of the MERRA-2 nonlinear model. The matrix \mathbf{C} corresponding to a linearized total energy norm accounts for moist perturbations as in Equation (10) of [Holdaway et al. \(2014\)](#), with the latent heat term weighted by a factor of 0.3, as in this study; see (2.9), page 16. [Holdaway et al. \(2014\)](#) argues that this value produces approximately equal weighting between the temperature and specific humidity components of the norm. The matrix \mathbf{P} incorporates a projection operator that simply amounts to a diagonal matrix with ones along most of its diagonal except for some zeroes to exclude perturbation contributions roughly above the 60-th level of the model (roughly 0.6168 hPa) to steering results away from sponge layer effects. Recall that the version of total energy weights used in the present work emphasizes the troposphere and as a consequence the inclusion of such projection operator makes no significant difference to the results.

The MERRA-2 reanalysis production was split into four parallel streams running simultaneously in order to have a timely production. Each stream was spun up for a year previously to its distribution. With streams 1-3 completed, the fourth stream is still being produced near-real-time until the present. A summary of the dates is presented in Table 3.1. Although MERRA-2 is still running, we made a choice to evaluate the impacts from the beginning of the reanalysis until 2017.

Table 3.1 - Production dates of the four streams of MERRA-2.

Stream	Beginning	Distribution	Final
1	1 Jan 1979	1 Jan 1980	31 Dec 1991
2	1 Jan 1991	1 Jan 1992	31 Dec 2000
3	1 Jan 2000	1 Jan 2001	31 Dec 2010
4	1 Jan 2010	1 Jan 2011	Present

3.1.2 Observation impact in MERRA-2

As mentioned above, all results that follow have been obtained for the 0000 UTC analysis of the January and July months of MERRA-2 from 1980 to 2017. It should be noted that the results that follow do not provide an assessment of the impact of precipitation and ozone observations used in MERRA-2. To be able to reliably provide such assessment the adjoint of the model and that of the analysis must account for these quantities properly, as well as the norm defined by the weighting matrix \mathbf{C} in (2.1). Although the adjoint of the GSI carries ozone perturbations in a manner consistent with the forward analysis, the moist total energy norm does not weight perturbations in ozone, and more importantly, the linear model only transports ozone, but does not account for any other process represented in the nonlinear model¹. When it comes to precipitation, the simplified physics in the linear model does not allow for its adequate representation, and the use of retrieved rain rates (such as those from SSM/I and TMI) are known not to influence the GSI analysis, nor subsequent backgrounds, in any significant manner. These factors dismiss any possible assessment of precipitation-related observation in MERRA-2.

A remaining issue in the FSOI approach in general, and in the implementation for this work in particular, is associated with how well nonlinearities are approximated by the tangent linear and its corresponding adjoint components. When it comes to the adjoint of the nonlinear general circulation model, the study of [Holdaway et](#)

¹Note that modifying \mathbf{C} to account for ozone is simple, but not much worth given the model adjoint lack of related processes representation.

al. (2014), and the upgrades then implemented in the simplified physics, indicates that the linear impact is capable of recovering roughly 80% of the nonlinear error reduction. This is essentially an upper limit for how much of the nonlinear impact can be recovered by its linear counterpart, for global applications using GEOS. Their work validated the implementation of a 1° adjoint, using a 1° nonlinear (trajectory) model, and a fully consistent adjoint analysis setting. When it comes to the analysis adjoint, consistency refers to use of similar minimization options in the backward and forward modes of doing the analysis. The GSI software supports a number of minimization strategies. Some are based on preconditioning with the full background error covariance (\mathbf{B}), such as the double conjugate gradient (CG) of Derber and Rosati (1989) and the bi-CG algorithm of El Akkraoui et al. (2013); others are based on preconditioning with the square-root of \mathbf{B} . The analysis adjoint machinery of Trémolet (2008), represented in (3.1), was originally implemented for the latter preconditioning strategy, and it is capable of handling multiple middle (outer) loops. No adjoint option is available for the double CG algorithm and the adjoint of the bi-CG, originally coded after Trémolet (2008) for a single middle loop (as currently used in GEOS FP), was extended in this work to accommodate multiple middle loops. The present work is thus consistent in that its adjoint 3D-Var analysis employs as many middle loops as those employed in the forward analysis. The adjoint is also consistent in the sense that it deals with a similar cost function as that of the forward problem, thus, as for example, employing an FGAT strategy.

The work of Holdaway et al. (2014) is consistent in the sense that it employs a square-root preconditioning minimization option, with two outer loops, in both the forward and backward analyses. As briefly introduced in Chapter 2, the observation impact in an incremental variational data assimilation scheme implementing multiple outer-loops can be obtained through (2.6), page 13. MERRA-2 implements a two outer-loop procedure in its forward analysis, this results in (2.6) using $J = 2$, being expressed as below:

$$\delta e = \mathbf{d}_1^T \mathbf{K}_1^T \mathbf{H}_2^T \mathbf{K}_2^T \mathbf{g} + \mathbf{d}_2^T \mathbf{K}_2^T \mathbf{g}. \quad (3.1)$$

3.1.3 Region definitions

As briefly introduced in Chapter 1, this study presents global results in Chapter 4 and a closer look into these results over the Amazon basin in Chapter 5. We conveniently split our global results into four subregions, namely, the Northern Hemisphere

Extratropics (NHX, north of 20°N), Southern Hemisphere Extratropics (SHX, south of 20°S), Tropics (TRP, between 20°S and 20°N), and the Amazon basin in South America. In this study, we define Amazon basin as a region between the segments 20°S and 4°N in latitude and between 78°W and 45°W in longitude. The actual resulting basin is thus defined as the union of six boxes corners, which are presented in Table 3.2. When these six boxes are combined, the external boundary results in the polygon defined by the black contour in Figure 5.5 (page 79). This is an attempt to cover the major part of a more formally defined basin while excluding adjacent oceans and high altitudes areas of the Andean Cordillera.

Table 3.2 - Boxes corners of the defined regions and the main chapters in which they are used.

Main Usage	Region	Latitude		Longitude	
		Min.	Max.	Min.	Max.
Chapter 4	Global	90.0°S	90.0°N	180.0°W	180.0°E
	NH Extratropics	20.0°N	90.0°N	180.0°W	180.0°E
	SH Extratropics	90.0°S	20.0°S	180.0°W	180.0°E
	Tropics	20.0°S	20.0°N	180.0°W	180.0°E
Chapter 5	Amazon basin	14.5°S	2.0°S	53.0°W	45.0°W
		20.0°S	4.0°N	63.0°W	53.0°W
		15.0°S	3.0°N	70.0°W	63.0°W
		13.0°S	2.0°N	72.0°W	67.0°W
		11.0°S	2.0°N	76.0°W	72.0°W
		8.0°S	1.0°N	78.0°W	76.0°W

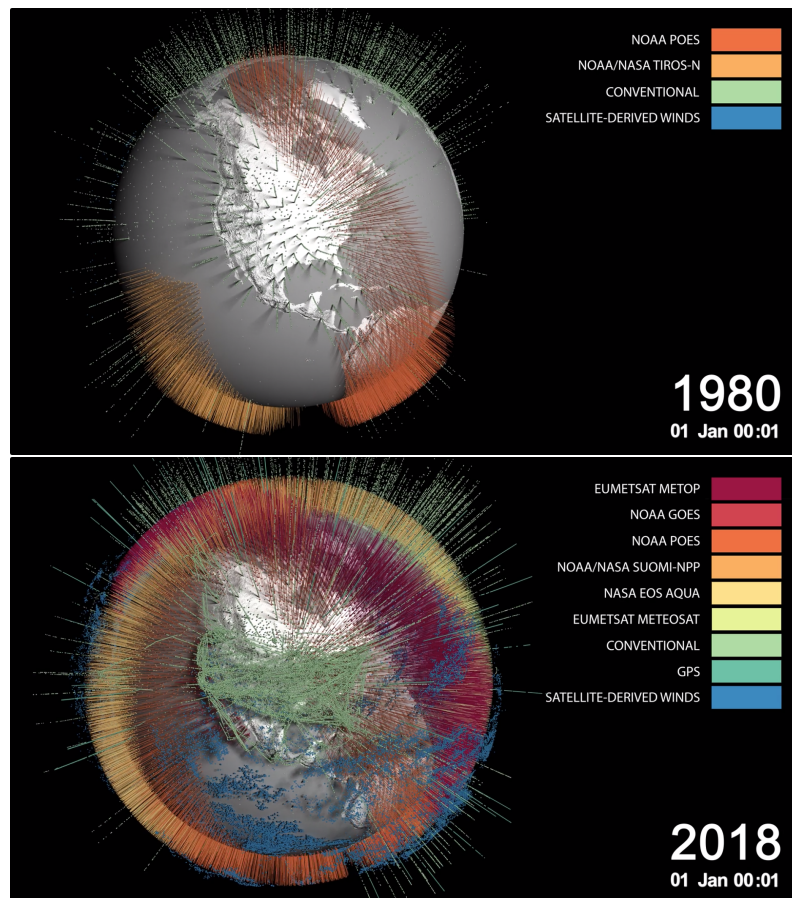
3.2 Data

As briefly explained in the previous section, this thesis derives observation impact in the context of a state-of-the-art data assimilation system over a long-time history. This system has the ability of handling a variety of observing systems. An example to illustrate it is presented in Figure 3.2. This figure shows spatial distributions of observations over the western hemisphere during two distinct periods, January of 1980 and January of 2018. These periods represents the early single platform days (top panel) and the current multi-platform scenario (bottom panel).

3.2.1 Observations

The data considered in this study is the input meteorological observations to the GSI, which is at the heart of the MERRA-2 reanalysis. As MERRA-2 is a successor

Figure 3.2 - Spatial distribution of observations at 0001 UTC of 1 January 1980 (top) and 1 January 2018 (bottom).



SOURCE: NASA's Scientific Visualization Studio (2018).

to MERRA, it incorporates a considerable revision of the observing system used in MERRA; a detailed description is provided in [McCarty et al. \(2016\)](#). The MERRA-2 observing system includes the so-called conventional observations; remotely-sensed ground based observations; satellite-derived wind observations; satellite retrieved observations; radio occultation observations; and satellite radiance observations.

Remotely-sensed ground based observations includes observations from profilers and radar. Satellite-derived wind observations include winds obtained from a variety of satellites through the Atmospheric Motion Vector (AMV) technique and scatterometer. Satellite retrieved observations include the ozone, rain rate and temperature from a variety of satellites. Radio occultation includes the bending angle observa-

tions derived from various satellites. Radiance observations are also obtained from a variety of satellites. The complete set of input observations assimilated in MERRA-2 is presented in Table 3.3 in addition to the beginning and ending dates of each category.

Table 3.3 - Dates of observation data types assimilated in MERRA-2. Underlined rows refer to instruments not considered in this study.

Data type	Begin date	End date
Radiosonde, Pilot Balloon and Dropsonde	1 Jan 1980	Present
AIREP, PIREP, ASDAR, and MDCRS aircraft	1 Jan 1980	Present
PAOB	1 Jan 1980	17 Aug 2010
Surface Land	1 Jan 1980	Present
Surface Ship and Buoy	1 Jan 1980	Present
Wind Profiler	14 May 1992	Present
NEXRAD VAD wind	16 Jun 1997	Present
GMS, MTSAT, and Himawari AMV	1 Jan 1980	Present
MeteoSat AMV	1 Jan 1980	Present
GOES AMV	1 Jan 1980	Present
AVHRR AMV	1 Oct 1982	Present
MODIS AMV	2 Jul 2002	Present
SSM/I and SSMI/S surface wind speed	9 Jul 1987	29 Oct 2013
ERS-1 surface wind vector	5 Aug 1991	21 May 1996
ERS-2 surface wind vector	19 Mar 1996	29 Mar 2011
QuikSCAT surface wind vector	19 Jul 1999	22 Nov 2009
WindSat surface wind vector	13 Aug 2007	4 Aug 2012
ASCAT surface wind vector	15 Sep 2008	Present
<u>SBUV and SBUV/2 ozone</u>	1 Jan 1980	31 Sep 2004
<u>SSM/I rain rate</u>	9 Jul 1987	16 Sep 2009
<u>TMI rain rate</u>	1 Jan 1998	8 Apr 2015
MLS temperature	13 Aug 2004	Present
<u>MLS ozone</u>	1 Oct 2004	Present
<u>OMI total column ozone</u>	1 Oct 2004	Present
GPSRO bending angle	14 Jul 2004	Present
TOVS	1 Jan 1980	10 Oct 2006
SSM/I	9 Jul 1987	4 Nov 2009
ATOVS	21 Jul 1998	Present
Sounder	24 Apr 2001	Present
AMSU-A (Aqua)	1 Sep 2002	Present
AIRS	1 Sep 2002	Present
IASI	17 Sep 2008	Present
ATMS	16 Nov 2011	Present
SEVIRI	15 Feb 2012	Present
CrIS	7 Apr 2012	Present

The observations presented in Table 3.3 will be further partitioned for convenience in different categories when presenting the results in Chapters 4 and 5. The partitioning of the observations follows mostly those in McCarty et al. (2016). However, a few categories comes from the observing system classification of the predecessor of MERRA-2, the MERRA categories introduced in Rienecker et al. (2008) (e.g., for aircrafts). A rough, high-level look at the MERRA-2 observing system is presented in Figure 3.1. The abbreviations on the figure stand for: observations of temperature, specific humidity, surface pressure and horizontal wind components (zonal and meridional) from surface and upper-air *in situ* instruments (Conventional); observations of temperature and horizontal wind components from aircraft *in situ* instruments (Aircraft); radiance observations from advanced microwave (MW) instruments [Advanced MW, e.g., AMSU-A, AMSU-B, Microwave Humidity Sounder (MHS), Advanced Technology Microwave Sounder (ATMS)]; radiance observations from the Atmospheric Infrared Sounder (AIRS); satellite-derived horizontal wind components from atmospheric motion vectors technique (AMV); radiance observations from the Cross-track Infrared Sounder (CrIS); infrared radiance observations from geostationary satellites (Geo IR); bending angle observations obtained using the global positioning system radio occultation technique (GPSRO); radiance observations obtained from early infrared (IR) instruments [Heritage IR, e.g., Stratospheric Sounding Unit (SSU), High-resolution Infrared Radiation Sounder-2 (HIRS-2), HIRS-3, HIRS-4] and early microwave instruments [Heritage MW, e.g., Microwave Sounding Unit (MSU)]; radiance observations from the Infrared Atmospheric Sounding Interferometer (IASI); surface horizontal wind speed and components from scatterometers (Surface Wind); and radiance observations from SSM/I. Notice that precipitation and ozone observations are not included in the figure since this work does not provide an estimate of impacts from these types of data (more on this below). For ease of reference, Table 3.4 provides a summary of the start and end dates for the observation data types used in MERRA-2.

The changes in observing systems taking place over the near 40 years of reanalysis are quite dramatic. For a good part of the 1980's, conventional observations make up nearly half of all available instruments used in the assimilation. In this initial decade, the other sources of dominant observations are the early microwave and infrared instruments on board of TIROS-N and the NOAA satellites 06 through 14. In the late 1980's we see the introduction of remote-sensed surface winds observations, with a noticeable increase in the fractional count of spaceborne measurements. A substantial change in satellite-based instrumentation comes when AMSU is introduced in 1998. Its main contribution coming from the refinement in vertical resolution as

Table 3.4 - Descriptions of the main abbreviated observation categories.

Category	Variable	Source
Conventional	u, v, T, q, p_s	Surface and upper-air <i>in situ</i> instruments
Aircraft	u, v, T	Aircraft <i>in situ</i> instruments
AMV	u, v	Atmospheric Motion Vectors (AMV) technique
Surface Wind	u, v, V	Surface wind from scatterometers
Heritage MW	T_b	MSU
SSM/I	T_b	SSM/I
Advanced MW	T_b	AMSU-A, AMSU-B, MHS, ATMS
Heritage IR	T_b	SSU, HIRS-2, HIRS-3, HIRS-4
Geo IR	T_b	GOES, SEVIRI
AIRS	T_b	AIRS
IASI	T_b	IASI
CrIS	T_b	CrIS
GPSRO	α	GPS radio occultation

The variables are defined as: u , zonal wind component; v , meridional wind component; V , horizontal wind speed; T , temperature; q , specific humidity; p_s , surface pressure; T_b , brightness temperature; and α , bending angle.

compared to MSU. As the reanalysis enters the EOS era and moves toward current times, the introduction of various hyperspectral IR instruments amounts to a dramatic increase in the volume of observations, even though only a few more than 100 channels are typically assimilated out of the couple of thousand channels available from these instruments (and are not counted in Figure 3.1). These instruments are associated with aiding temperature and humidity fields, but the EOS era also sees a considerable increase in satellite-derived wind observations, aircraft observations of temperature and winds, and the introduction of GPS radio occultation. Though not visible in Figure 3.1, the reanalysis period sees a steady drop in the global count of its most conventional component, namely, radiosonde observations.

Radiance observations are from a variety of platforms and instruments. These observations can be categorized according to its platforms following the categories presented in Table 3.5. In addition to it, the same observations can be also categorized according to its instruments. The instruments classification is presented in Table 3.6.

A summary of the quantity of channels assimilated for each of the instruments presented in Table 3.6 is as follows: 3 channels of MSU; 11 of AMSU-A; 5 of AMSU-B; 5 of MHS; 17 of ATMS; 7 of SSM/I; 3 of SSU; 10 of HIRS; 117 of AIRS; 136 of IASI; 120 of CrIS; 11 of Sounder; and 2 of SEVIRI. The specific nominal channel selections

Table 3.5 - As in Table 3.4 (page 32), but for brightness temperature (T_b) variable obtained through radiance satellites.

Platform	Sensors
TIROS-N	SSU; HIRS-2
NOAA-6	MSU; SSU; HIRS-2
NOAA-7	MSU; SSU; HIRS-2
NOAA-8	MSU; SSU; HIRS-2
NOAA-9	MSU; SSU; HIRS-2
NOAA-10	MSU; HIRS-2
NOAA-11	MSU; SSU; HIRS-2
NOAA-12	MSU; HIRS-2
NOAA-14	MSU; SSU; HIRS-2
NOAA-15	AMSU-A, -B; HIRS-3
NOAA-16	AMSU-A, -B; HIRS-3
NOAA-17	AMSU-A, -B; HIRS-3
NOAA-18	AMSU-A; MHS
NOAA-19	AMSU-A; HIRS-4
MetOp-A	AMSU-A; MHS; HIRS-4; IASI
MetOp-B	AMSU-A; MHS; IASI
Aqua	AMSU-A; AIRS
GOES-8	Sounder
GOES-10	Sounder
GOES-11	Sounder
GOES-12	Sounder
GOES-13	Sounder
GOES-15	Sounder
DMSP-F08	SSM/I
DMSP-F10	SSM/I
DMSP-F11	SSM/I
DMSP-F13	SSM/I
DMSP-F14	SSM/I
DMSP-F15	SSM/I
SNPP	ATMS; CrIS
MeteoSat-9	SEVIRI
MeteoSat-10	SEVIRI

is presented in Table 3.7. Its usage can vary for individual satellite platforms as a result of sensor failure or quality control decisions (GELARO et al., 2017).

Table 3.6 - As in Table 3.4 (page 32), but for brightness temperature (T_b) variable obtained through radiance sensors.

Sensor	Platforms
MSU	NOAA-6, -7, -8, -9, -10, -11, -12, -14
AMSU-A	NOAA-15, -16, -17, -18, -19; MetOp-A, -B; Aqua
AMSU-B	NOAA-15, -16, -17
MHS	NOAA-18; MetOp-A, -B
ATMS	SNPP
SSM/I	DMSP-F08, -F10, -F11, -F13, -F14, -F15
SSU	TIROS-N; NOAA-6, -7, -8, -9, -11, -14
HIRS-2	TIROS-N; NOAA-6, -7, -8, -9, -10, -11, -12, -14
HIRS-3	NOAA-15, -16, -17
HIRS-4	NOAA-19; MetOp-A
AIRS	Aqua
IASI	MetOp-A, -B
CrIS	SNPP
Sounder	GOES-8, -10, -11, -12, -13, -15
SEVIRI	MeteoSat-9, -10

Table 3.7 - Nominal channel selections for satellite radiances according to each sensor presented in Table 3.6 (page 35). Channels in bold denote those that are assimilated without any bias correction (only AMSU-A, ATMS, and SSU) and underlined channels were used through 31 July 2012 (only CrIS).

Sensor	Assimilated Channels
MSU	2, 3, 4
AMSU-A	4, 5, 6, 7, 8, 9, 10, 11, 12, 13, 14
AMSU-B	1, 2, 3, 4, 5
MHS	1, 2, 3, 4, 5
ATMS	5, 6, 7, 8, 9, 10, 11, 12, 13, 14, 15 , 17, 18, 19, 20, 21, 22
SSM/I	1, 2, 3, 4, 5, 6, 7
SSU	1, 2, 3
HIRS	2, 3, 4, 5, 6, 7, 8, 10, 11, 12
AIRS	3, 6, 9, 10, 11, 13, 14, 18, 21, 29, 31, 44, 45, 46, 47, 49, 50, 52, 53, 55, 56, 57, 59, 60, 61, 62, 63, 64, 65, 66, 67, 68, 70, 72, 73, 75, 76, 77, 78, 80, 81, 83, 84, 85, 86, 87, 88, 89, 90, 91, 92, 93, 94, 95, 96, 97, 98, 99, 100, 101, 102, 103, 104, 105, 106, 107, 109, 110, 113, 114, 115, 116, 117, 119, 121, 122, 123, 124, 125, 126, 128, 129, 130, 166, 167, 168, 169, 170, 171, 172, 173, 174, 176, 177, 178, 181, 182, 186, 190, 193, 202, 208, 212, 215, 216, 217, 218, 219, 220, 221, 222, 223, 225, 226, 227, 228, 229
IASI	1, 5, 9, 11, 13, 15, 16, 17, 19, 20, 22, 23, 24, 27, 28, 30, 32, 34, 43, 44, 45, 47, 48, 49, 50, 51, 52, 53, 54, 55, 56, 57, 58, 59, 60, 61, 63, 64, 65, 66, 68, 69, 70, 71, 72, 73, 75, 76, 77, 79, 81, 85, 86, 87, 88, 90, 91, 93, 94, 95, 97, 99, 101, 102, 104, 105, 106, 107, 108, 109, 111, 112, 113, 114, 115, 116, 118, 120, 121, 122, 124, 125, 129, 131, 132, 134, 135, 136, 137, 138, 139, 140, 142, 143, 145, 146, 147, 148, 149, 150, 151, 152, 153, 154, 155, 157, 159, 161, 162, 165, 166, 167, 169, 170, 172, 174, 180, 181, 182, 183, 184, 185, 186, 191, 192, 193, 196, 198, 199, 200, 201, 202, 205, 206, 208, 209, 211
CrIS	1, 23, <u>26</u> , 27, 29, <u>30</u> , 31, 32, <u>33</u> , 34, <u>35</u> , 36, 39, 40, 41, <u>42</u> , <u>43</u> , 44, 45, <u>46</u> , 47, 48, <u>49</u> , 50, 51, <u>52</u> , <u>53</u> , 54, 57, <u>58</u> , 59, <u>60</u> , <u>61</u> , 62, <u>63</u> , <u>64</u> , 65, <u>66</u> , <u>67</u> , 68, <u>69</u> , <u>70</u> , 71, <u>72</u> , 73, <u>74</u> , 75, <u>76</u> , 79, 80, 81, 82, 83, 84, 85, <u>86</u> , 87, 88, 89, <u>90</u> , 91, 92, 93, 101, 113, 120, 121, 122, 123, 124, <u>125</u> , 126, 128, 185, 226, 228, <u>229</u> , 230, 237, 239, 261, 274, <u>275</u> , 276, <u>277</u> , 278, <u>279</u> , <u>280</u> , 281, <u>282</u> , 283, <u>284</u> , 285, <u>286</u> , 287, <u>288</u> , <u>289</u> , 290, <u>291</u> , 292, <u>293</u> , <u>294</u> , 295, 296, 297, 298, 299, 300, 301, 302, 303, 304, 305, 306, 307, 308, 309, <u>310</u> , 311, 312
Sounder	1, 2, 3, 4, 5, 6, 7, 8, 10, 11, 12
SEVIRI	2, 3

4 FSOI APPLICATION TO REANALYSIS

This chapter presents the results obtaining observation impacts in a multi-year reanalysis dataset, using the FSOI technique.

4.1 Introduction

The MERRA-2 is the latest global atmospheric reanalysis produced by the NASA GMAO. At the time of this writing, MERRA-2 is an ongoing reanalysis covering nearly 40 years of assimilation, from 1980 to the present. As other reanalyses, its main purpose is to provide a data set for climate studies devoid of the discontinuities encountered in operational NWP records, where frequent system upgrades introduce nonphysical signatures in the time series. Although minimized to good extent, irregularities in the boundary conditions (sea surface temperature and sea ice) and intrinsic change in the observing system over the course of such multi-year integration, can introduce undesirable features in the record still.

An example along the lines of illegitimate changes in the reanalysis record introduced by the observing system and its treatment is the unrealistic trend in precipitation noticed in MERRA (e.g., Section 7a of [Rienecker et al., 2011](#)). Close investigation reveals it to be associated with the use of window channels (1-3 and 15) from the Advanced Microwave Sounding Unit-A (AMSU-A) instruments, which as a consequence, are chosen not to participate in MERRA-2; and by analogy channels 1-4 and 15 of the Advanced Technology Microwave Sounder (ATMS) and channel 1 of the Microwave Sounding Unit (MSU) are also not assimilated. Similar sensitivities are also found with respect to the assimilation of AMSU-B, and even more so with the introduction of the Special Sensor Microwave Imager (SSM/I). Arguably, under the dry mass conservation constraint feature added to MERRA-2 (below) these choices could have well been revisited.

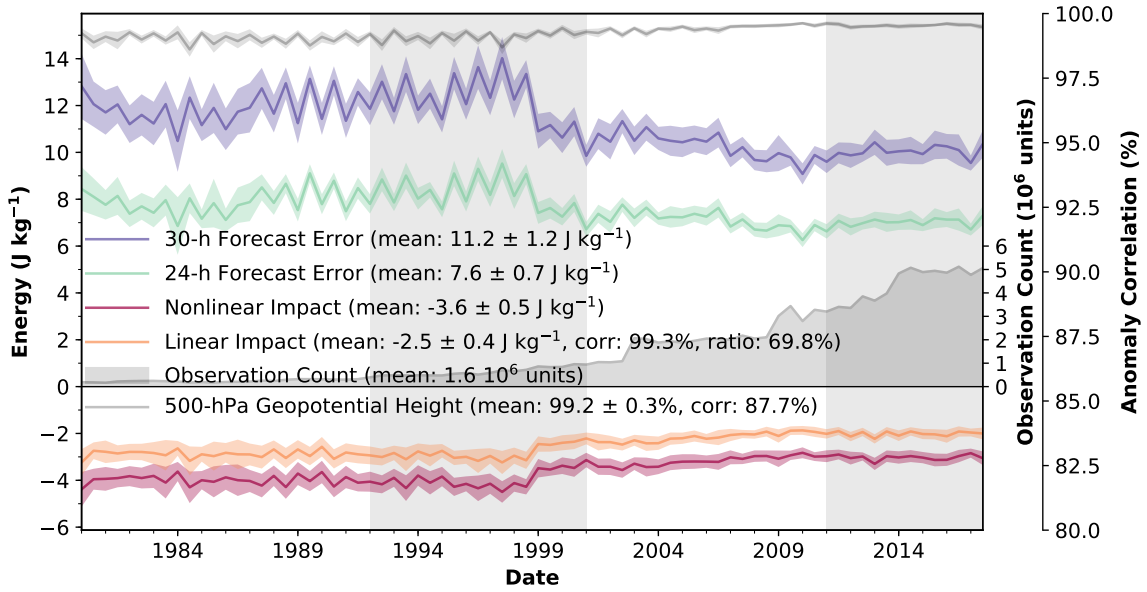
Careful treatment of boundary conditions and observation datasets to be used in reanalysis, as well as variational bias correction ([DERBER; WU, 1998](#)), incremental analysis update ([BLOOM et al., 1996](#)), and imposition of physical constraints to the assimilation system (e.g., [Takacs et al., 2016](#)) are a few of the mechanisms used to ameliorate the situation and try to reduce the introduction of spurious signals in data assimilation and reanalyses in particular.

However careful reanalysis efforts might be, changes in the observing system can substantially change the quality (and likely the character) of the underlying analyses.

An illustration of the improved quality of analyses along the course of MERRA-2 can be seen from short-range forecasts produced for its analyses, as a parallel exercise to the MERRA-2 production. Figure 4.1 shows 30- (purple curve) and 24-hour (green curve), total energy normalized, forecast errors calculated with respect to self-analyses for all January and July from 1980 to 2017. The 30-hour forecasts are issued from 1800 UTC analyses and the 24-hour forecasts are issued from the subsequent 0000 UTC analyses. The most striking feature in both forecast error time series is their abrupt change in behavior around the late 1990's and beginning of 2000's — referred to here as the Earth Observing System (EOS) era, or sometimes simply modern era in the context of the present study. Not only do the errors seem to level along a smaller value in the EOS era as compared to the pre-EOS era, but also noticeable are the reduction in the amplitude of the zig-zagging of the errors between consecutive January and July months, and the reduced amplitude of the spread of the errors between these two periods (indicated by the one standard deviation from the mean shaded areas). The EOS era saw a dramatic change in the observing system, especially by the introduction of instruments placed on satellite platforms, such as: AMSU-A and -B in 1998; longwave, window, and water vapor channels from Geostationary Operational Environmental Satellites (GOES) Sounder in 2001 and water vapor channels from Spinning Enhanced Visible Infra-Red Imager (SEVIRI) in 2012; hyper-spectral infrared Atmospheric Infrared Sounder (AIRS) in 2002; and the Global Positioning System radio occultations (GPSRO) in 2004. These help explain the improved quality in forecasts during this era with subtle but noticeable error reductions seen in the errors time series. Also noticeable in the forecast error curves in the figure is the slight increase in error from the mid-1980's until about the end of the pre-EOS era. We will see later that these are largely due to error growth in the Tropics and Southern Hemisphere. The reasons for such error growth in the short-range forecasts of MERRA-2 remains to be fully understood.

As briefly introduced in Chapter 2, a measure of the contribution brought about by assimilating observations in each cycle can be obtained by subtracting the 30-hour forecast error from the 24-hour error since these are verified at the same time. The error reduction brought about by assimilating six more hours of observations is shown by the red curve in Figure 4.1; the variability of the reduction is shown by the one standard deviation red-shaded area around the same curve. The improvement in the background from assimilating the increased set of observations in the EOS era as compared to the pre-EOS era is reflected in the reduction (in absolute value) of the error reduction in the EOS period. It is a matter of interest to try to understand which of the different instruments contribute to bringing about these improvements

Figure 4.1 - Time series of 30- (violet) and 24-h (green) forecast errors, nonlinear (red) and linear (orange) impact estimates and the count of used observations (yellow, right axis). Lines represent monthly mean values with ± 1 standard deviation from the mean in shading for 0000 UTC analyses during months of January and July. The vertical shaded and non-shaded areas represent the four streams of MERRA-2. Numerical values in the legend represent mean ± 1 standard deviation in addition to the Pearson's correlation between linear and nonlinear impacts and its ratio. For reference, the time series of monthly averaged 500 hPa geopotential height anomaly correlations is also shown (grey curve) with scales on the far right vertical axis (%). The units of energy are J kg^{-1} and the scale factor for observation count is 10^6 .



SOURCE: Author's production.

along the course of the reanalysis. A lot of insight is already given in this regard in works such as that of [Dee and Uppala \(2009\)](#). Other reanalysis articles have further contributed to this understanding (e.g., [Rienecker et al., 2011](#); [Dee et al., 2011](#); [Gelaro et al., 2017](#); and references therein).

The present work is yet another contribution along the lines of highlighting the significance of different components of the observing system. The approach taken here differs from that of previous works in that it applies the [Trémolet \(2008\)](#) extension of [Langland and Baker \(2004\)](#), adjoint-based approach to assess the impact of observations used in reanalysis. Unlike traditional examination of root-mean-square error of observation residuals, which carries with it the units of the observables, the adjoint-

based methodology unifies the units and facilitates cross-comparing the contribution of different types of observations. Specifically, this approach is natural to the version of the GMAO Global Earth Observing System (GEOS) assimilation system used to produce MERRA-2, since its software has at its disposal the whole machinery required by adjoint-based methods. Indeed, the MERRA-2 version of GEOS is very closely related to what GMAO had at some point in time for its so-called forward processing, near real-time system for which FSOI is routinely derived and monitored. It is worth mentioning that the impact of observations can also be obtained by using the adjoint-free degrees of freedom for signal (DFS) approach of [Lupu et al. \(2011\)](#). [Horányi \(2017\)](#) applies DFS to the latest ECMWF reanalysis, the ERA5, though the work evaluates the impact of observations only over a few months of a set of key selected years. In many ways, as discussed in [Todling \(2013\)](#), DFS and FSOI provide complementary information about the contribution of the observing system: the first to the cycling variational system; the second to short-range forecasts. The present work chooses to examine only FSOI for MERRA-2.

The [Trémolet \(2008\)](#) extension of the [Langland and Baker \(2004\)](#) approach provides an alternative way to estimate the error reduction displayed by the red curve in [Figure 4.1](#). Unlike the calculation related to producing this curve, which is performed in physical-space, the [Langland and Baker \(2004\)](#) estimate is derived in observation-space, and has thus the advantage of allowing for the approximate error reduction to be partitioned into the various sub-components of the observing system. The approximate estimates are reliable to the extent they are a fair representation of the actual error reductions. The orange curve in [Figure 4.1](#) displays the adjoint-based FSOI (total impact) estimate of the error reductions (referred to as total impacts). As indicated in the figure, the total impact correlates at over 99% with the actual error reduction, though it represents only about 70% of the magnitude of the total error reduction. This low percentage, when well understood and explained, does not deter from the results being used to obtain insightful conclusions about the observing system. Indeed, [Lorenz and Marriott \(2014\)](#) point out that it is more relevant to have the linear estimates well correlated with the nonlinear value and, as the case in [Figure 4.1](#), than to precisely match the level of error reduction. It is the main objective of the present work to provide an understanding for how the different components of the observing system used in MERRA-2 contribute to form the total impact displayed in this figure.

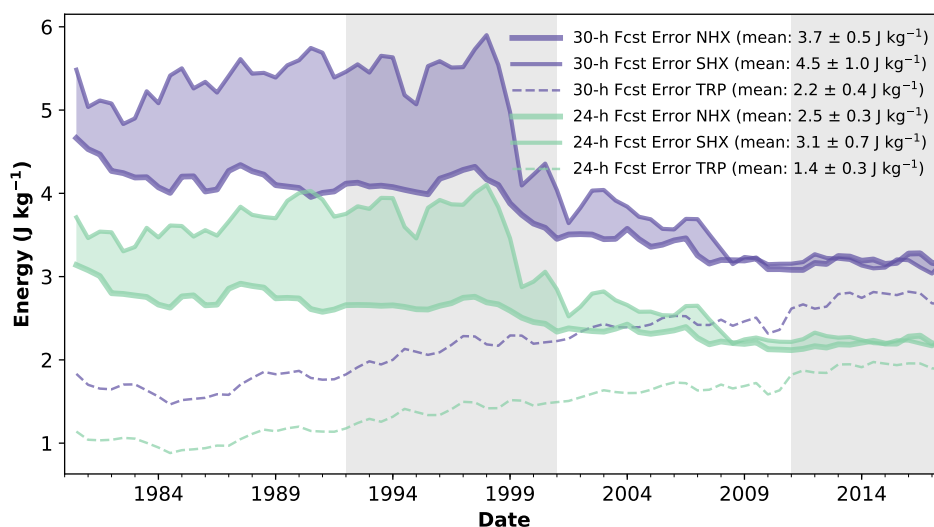
4.2 Forecast errors and sensitivities

An account for how the self-verified 30- and 24-hour errors in MERRA-2 short-range forecasts change over time is given in Figure 4.2. The calculation of the linearized total energy metric (2.1), page 12, is split into three regions, namely, Northern Hemisphere Extratropics (NHX, north of 20°N, thick line), Southern Hemisphere Extratropics (SHX, south of 20°S, thin line), and Tropics (TRP, between 20°S and 20°N, dashed line). The curves correspond to running means calculated to help quantify the inter-annual variability¹. The 30- and 24-h forecast errors correspond to the violet and green curves, respectively, and the shading shows the differences in scores between the two extratropical hemispheres. As seen elsewhere from more typical anomaly correlation results derived for longer forecast lead times (e.g., in particular panel (b) of Figure 1 of Dee et al., 2013, reproduced in this document as panel (b) of Figure 1.1, page 3), there is considerable improvement in forecast skill entering the EOS era (early 2000's onward), when the increase in number of remote sensing instruments brings about an abundance of observations (see Figure 3.1, page 24). The improvement is especially noticeable in the Southern Hemisphere Extratropics where the dominance of satellite over conventional observations is considerable. Interestingly, tropical errors seem to increase slightly, and steadily, from the mid-1980's until the late 2000's. Also surprising is the slight error increase in the Southern Hemisphere from the mid-1980's until about the late 1990's. Given that in the early days of the reanalysis observation coverage in the Tropics is not very vast, the errors at these early times might seem small simply due to their being less difference between the model predictions and the corresponding (verifying) analyses than at more recent times. As observations increase in amount, as well as in diversity of instruments, the errors increase and become more representative of differences between the verifying analyses and model predictions. Although the same argument might be used to explain the error growth in the Southern Hemisphere, it would appear more reasonable to look for an alternative explanation, such as large biases in the model or improper use of observations in the MERRA-2 analyses. This, however, is outside the scope of the present work.

The abrupt change in errors between the pre-EOS and EOS era identified in the figure here, and also noticed in Figure 4.1 (page 39), seems to differ from the results of Dee et al. (2013) where the 500 hPa geopotential height anomaly correlations

¹This is done using monthly-mean skill scores calculated over the years and calculating a running mean with the corresponding value of each month and its predecessor. As our results starts in January 1980, the value of this month is being omitted for consistency with the whole time series.

Figure 4.2 - Time series of (a) 30- (violet) and 24-h (green) forecast errors regionally partitioned into Northern Hemisphere Extratropics (NHX, thick), Southern Hemisphere Extratropics (SHX, thin), and Tropics (TRP, dashed), plotted in the form of annual running means. Values plotted for January (July) are averages over that month and the preceding July (January). The shading shows the differences in scores between the two extratropical hemispheres. The vertical shaded and non-shaded areas represent the four streams of MERRA-2. Numerical values in the legend represent mean ± 1 standard deviation. The units of energy are J kg^{-1} .



SOURCE: Author's production.

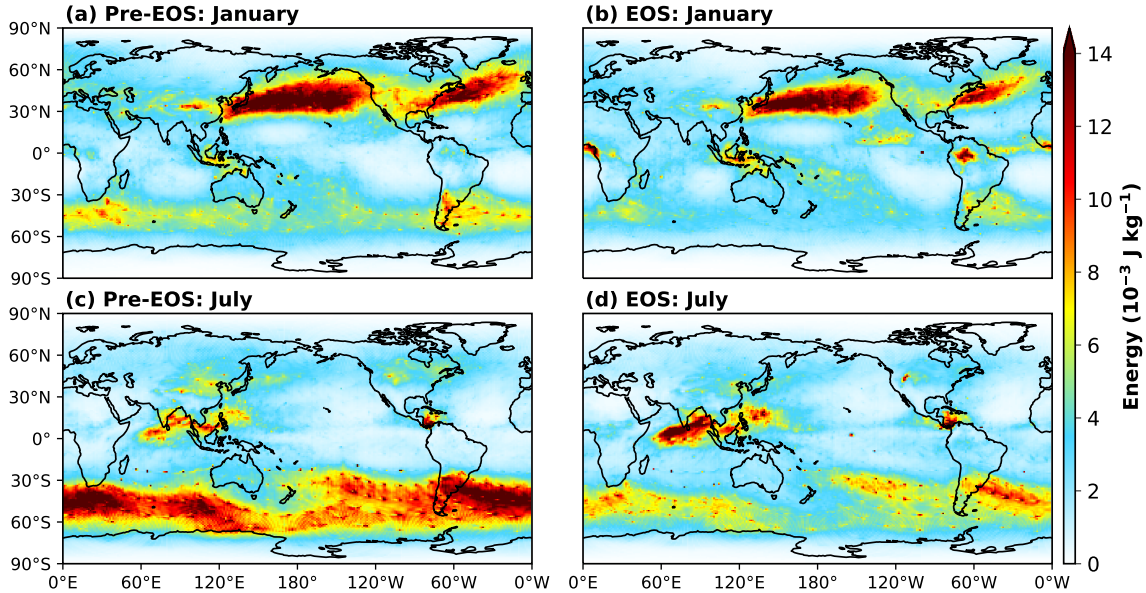
steadily rise from the early reanalysis periods to the present, with no clear jumps detected in the time series (shown for forecast lead times 3-, 5-, 7- and 10-days in their work). It is important to notice that care must be exercised when comparing the forecast errors shown in Figures 4.1 and 4.2 with more traditional error metrics. To emphasize this point, Figure 4.1 shows the time series of monthly averaged 500 hPa geopotential height, self-verified, anomaly correlations (grey curve) for the 24-hour forecasts on the January and July months of MERRA-2. With forecasts of such short lead-time the anomaly correlations are high to begin with even in the early days of the reanalysis when data is less abundant than in the more recent EOS days. Consistent with Dee et al. (2013), the day-1 500 hPa geopotential height anomaly correlations here rises steadily from start to end, showing no dramatic transition from the pre-EOS to the EOS era. As results from Figures 4.1 and 4.2 indicate, this

is an incomplete view of what truly happens to the errors. The total energy-based 24- and 30-hour forecast errors provide a more encompassing view since they account for the contribution of errors in mass, wind and humidity integrated through the whole troposphere and are thus more telling than typical error metrics based on single-level, single-variable quantities. Unlike the gentle rise in skill seen in the 500 hPa geopotential height anomalies, the total (tropospheric) forecast quality abruptly improves in the EOS era.

The reduction in extratropical forecast errors seen in Figure 4.2, and their corresponding increase of errors in the Tropics from the pre-EOS to the EOS era is directly related to the 24-hour vertically integrated energy in forecast sensitivities derived as intermediate inputs to diagnosing observation impacts through (2.2). Figure 4.3 shows 18-year averages for January (top) and July (bottom) of pre-EOS (1982-1999) and EOS (2000-2017) era 24-hour vertically integrated energy in forecast sensitivities given in J kg^{-1} [formed from the first term on the right-hand side of (2.3)]. The averages for January resemble the single January result in Figure 8 of Gelaro et al. (2010), and show the largest sensitivities being concentrated along the North Pacific and North Atlantic storm tracks; in July, the bottom panels in Figure 4.3 here show the largest sensitivities being flipped to the midlatitudes of the Southern Hemisphere; that is, global 24-hour forecast sensitivities are largest in the winter-hemisphere when the variability in the storm tracks are largest. Comparing the pre-EOS with the EOS eras, the sensitivities are in direct contrast to how forecast errors change, with reduced sensitivities in the Extratropics and increased sensitivities in the Tropics. The Extratropical behavior of the errors and their sensitivities reflects the combined improvement in model predictions and the ability of analysis systems, such as the 3D-Var in MERRA-2, to handle observations in those areas. In the Tropics, the increased forecast errors and sensitivities in a period of increased, largely remote sensed, tropical observations suggests the assimilation not to be making ideal use of such observations there. The MERRA-2 3D-Var assimilates a number of highly sensitive water-vapor channels from hyperspectral instruments, perhaps these contribute to the increase in errors. An accurate answer to this puzzle is deferred to future studies.

Having calculated the 30- and 24-hour forecast errors it is simple to calculate the forecast error reduction, Δe , defined in (2.7) — the so-called *nonlinear* observation impact. Figure 4.4 shows time series of this quantity for the January and July months of the reanalysis period, averaged and regionally split in similar ways as done in Figure 4.2. It is important to remember here, the more negative the numbers, the

Figure 4.3 - Eighteen-year averaged 24-hour vertically integrated energy in forecast sensitivities for January [top: (a) and (b)] and July [bottom: (c) and (d)] over the pre-EOS [1982-1999; left: (a) and (c)] and the EOS [2000-2017; right: (b) and (d)] eras. The scale factor is 10^{-3} and the units are J kg^{-1} .

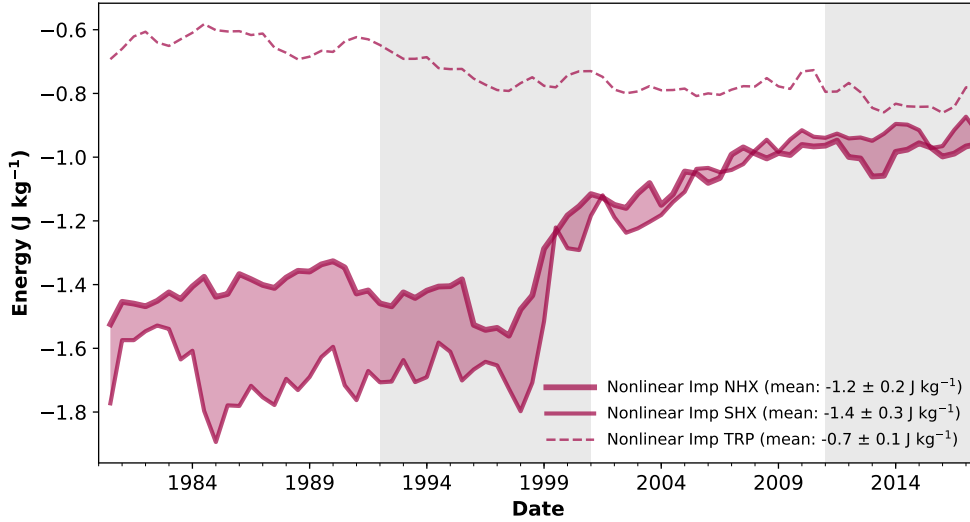


SOURCE: Author's production.

bigger the impact of assimilating observations. Not surprisingly, as model predictions improve dramatically over the Extratropics in the EOS era the impact of assimilating observations becomes less significant when compared to the impact in the pre-EOS era, when the observations had “to do a lot of work” to reduce forecast errors. In the Tropics, the situation is contrary, as the impact of assimilating observations increases when the system advances into the modern era.

Results from the alternative calculation of observation impact following the adjoint approach in (2.2) appear in Figure 4.5 — the so-called *linear* observation impact. Just as its nonlinear counterpart, Δe , shown in Figure 4.4, the observation-space-based total impact δe can also easily be split regionally. Comparison of these quantities shows that the adjoint-based results resemble quite well the error reductions; this being the crux in the reliability of the adjoint-based approach. Both show similar Northern and Southern Hemisphere differences and a sharp reduction of impact as the assimilation of observations improves the quality of backgrounds in the EOS era; both show the low impact observations had in the early days of MERRA-2

Figure 4.4 - As in Figure 4.2 (page 42), but for nonlinear impacts.



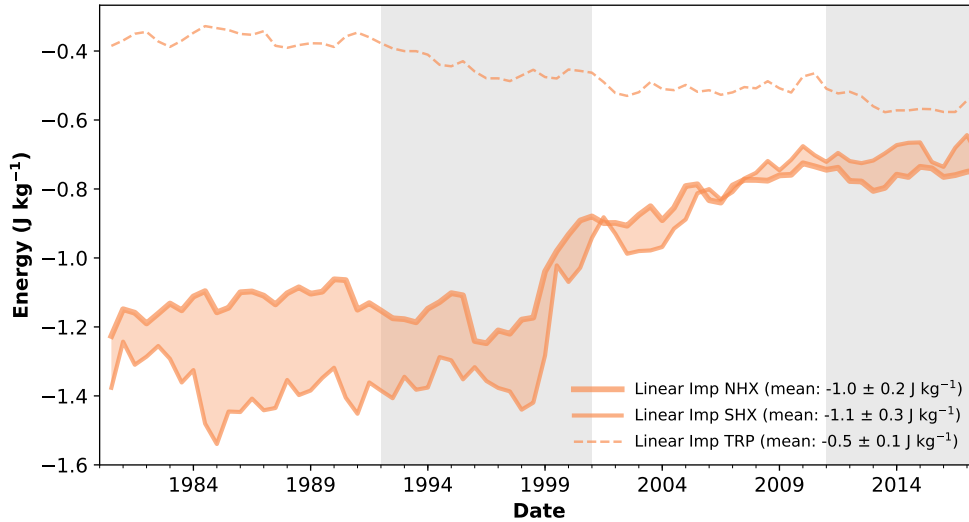
SOURCE: Author's production.

and the increased impact as the system gets into the modern era. The difference in magnitude between the forecast error reductions in Figure 4.4 and the observation impacts in Figure 4.5 is the consequence of the combined assumptions and approximations involved in contrasting Δe and δe : finite perturbation versus infinitesimal perturbation approaches; and the approximations making up both model and analysis adjoints with respect to their nonlinear (forward) counterparts. Although the forecast errors and its reduction over the Tropics increases, they are still smaller (in absolute value) when compared to either of the Extratropics.

4.3 Global perspective

One possible partition of the residual vector and corresponding impacts is to define classes based on the observable quantities handled in the MERRA-2 GSI 3D-Var analysis. The impacts of each of the related variable types and their fractional benefit are shown in Figures 4.6 and 4.7, respectively. These results are displayed as monthly means for each January and July of the period of MERRA-2 studied in this work. Although ozone and precipitation (rain rates) are other two variables handled in the MERRA-2 analysis, they are intentionally not account for here for the reasons explained above. From Figure 4.6 it is seen that the assimilation of horizontal

Figure 4.5 - As in Figure 4.2 (page 42), but for linear impacts.

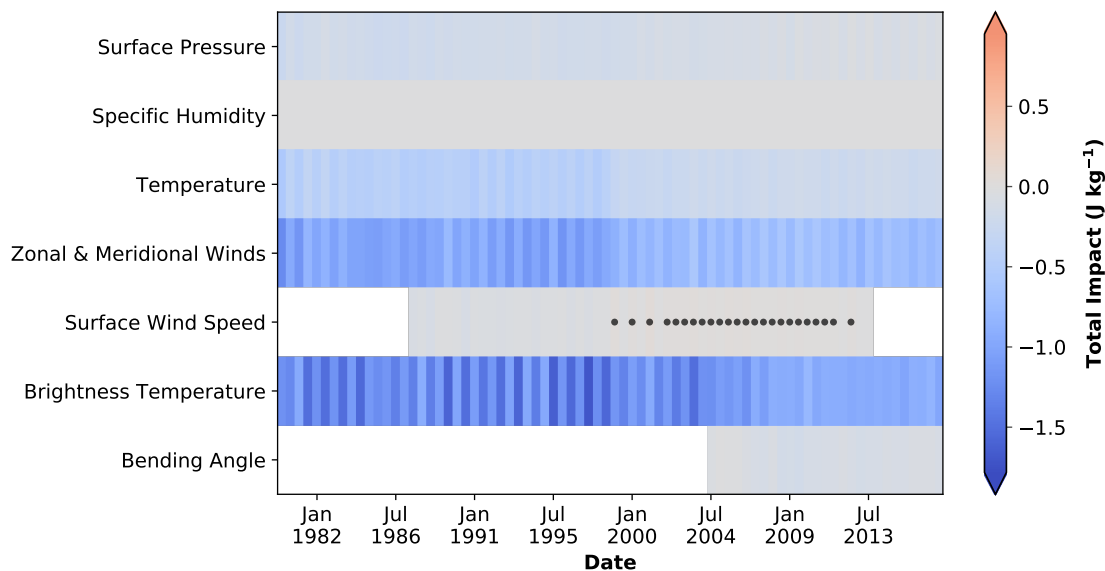


SOURCE: Author's production.

wind components and brightness temperatures dominate the analysis contribution to reducing 24-hour forecast errors. These types are followed by the contributions from assimilating temperature and surface pressure. A reduction on the impact from winds and temperature is noticeable as MERRA-2 enters the modern era. In the generality of this summary, and under the given scales, the contribution from assimilating specific humidity, surface wind speeds, and even bending angle from GPSRO seem minor as compared to the others. One factor that makes such categories seem to contribute little is that the categories of winds and brightness temperature are very broad, including a number of different instruments and platforms, and are thus bound to dominate. The contribution from surface wind speeds becomes disruptive especially as the assimilation of this quantity is taken into the modern era (notice red bars). These cases are not very intense and as such are highlighted with black dots for improved readability.

The fractional beneficial impacts shown in Figure 4.7 help compare the contribution from each of the analysis variable types removing the influence exerted from pure data volume of related observations. Beneficial fractions represent the percentage of observations contributing positively (negative values) to the observation impacts and are constructed by assuming the impact is smaller than -10^{-10} , that is, an

Figure 4.6 - Heatmap of monthly mean total observation impact for each assimilated variable type. Values are for 0000 UTC analyses during months of January and July. Patched boxes represent monthly mean values with ± 3 standard deviations from the total mean impact displayed in the figure and dots represent boxes with negative values. The units are J kg^{-1} .

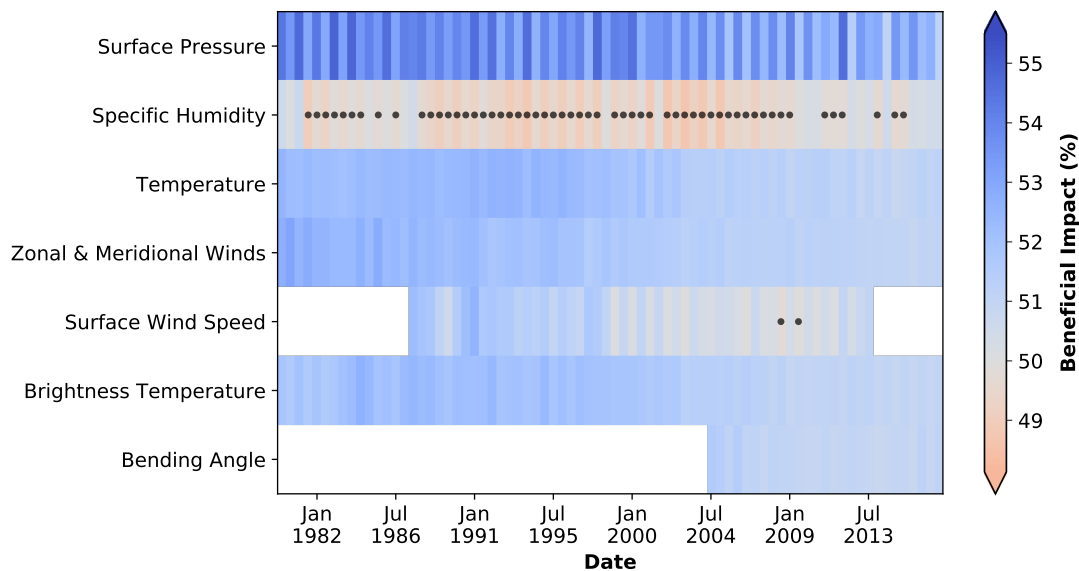


SOURCE: Author's production.

observation with impact $|d_i \tilde{g}_i| \leq 10^{-10}$ is considered neutral, and it is not taken into consideration in the results displayed in this figure². For most variables, and for most of the time, these fractions are slightly larger than 50%. Although results here remove contribution from so-called neutral impacts, they are still consistent with the results reported in the intercomparison work of Gelaro et al. (2010). The breath of the results here are, however, considerably broader since it applies to the context of a multi-year reanalysis. While about 50% of assimilated observations of temperature, wind, brightness temperature and bending angle contribute to reduce errors in the 24-hour forecasts, nearly 60% of all surface pressure observations contribute in the same direction, especially in the months of January. This is a somewhat surprising result. The scalar, univariate, analysis of M. Fisher (2006; pers. comm.) and Ehrendorfer (2007) suggest that between 60% to 65% of observations should contribute to improve the data assimilation cycle; Todling (2013) confirmed their results using

²This threshold is based on a choice made in an yet unpublished intercomparison and ongoing study extending and update the results of Gelaro et al. (2010) to including contributions from multiple global assimilation systems (Rauhl Mahajan, pers. comm.).

Figure 4.7 - As in Figure 4.6 (page 47), but for fractional of beneficial observations. The units are %.

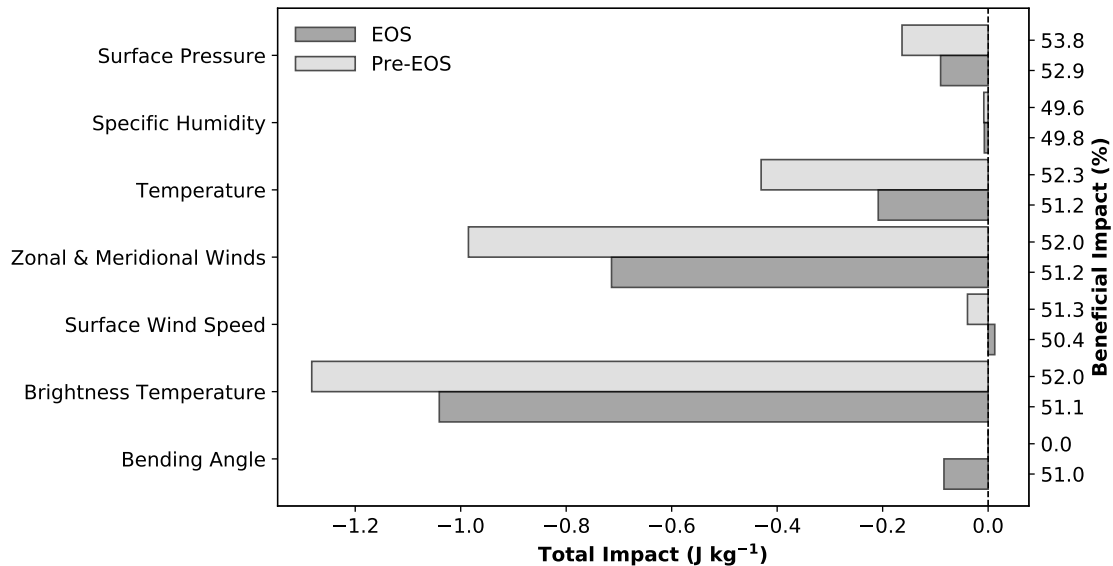


SOURCE: Author's production.

a DFS-like approach applied to the complete GEOS data assimilation system. No actual estimate exists for what exactly to expect in the context of *forecast* error reduction (i.e., FSOI), but since the Fisher-Ehrendorfer estimate for the impact on cycling analyses depends on the prescribed background and observation errors, it is likely that FSOI results also depend on these quantities and on how fast errors in the forecasting model grow. In this sense, it can be speculated that results for surface pressure here are associated with the quality of MERRA-2 forecasts of surface pressure as compared to other quantities. Given that MERRA-2 employs the Takacs et al. (2016) dry mass constraint it is possible this might contribute to the percentage observed here, but this will have to be investigated elsewhere. In Figure 4.7, only specific humidity observations seen to fall consistently under 50%. Though at times less than 50% of the assimilated surface wind speeds benefit the forecast, the number only systematically drops below 50% in the EOS era. In the case of humidity this could be associated with the lack of representation of correlations between this variable and temperature and winds; in the case of speed observations, the low beneficial rates could be associated with the effectiveness of the linearization of its observation operator and quality of the simplified boundary layer physics in the model adjoint.

To compare more directly results from the pre-EOS and EOS eras, Figure 4.8 presents mean impact over the two periods for the MERRA-2 analysis main observables. Relatively speaking, the ranking of dominance has not changed: in both periods brightness temperature dominates the impacts, followed by wind, and temperature. In the pre-EOS era these are followed by surface pressure; in the EOS era surface pressure and bending angle observations show roughly equal impact when reducing forecast errors. Under the measure defined by \mathbf{C} in (2.1), specific humidity and surface winds contribute very little to the error reduction. Overall, the impact of assimilating observation decreases in the EOS era as compared to the pre-EOS era. It is somewhat counter-intuitive, but nonetheless a fact, that observations have smaller impacts the more abundant and better quality they are. This goes right along with the error reduction noticed in Figure 4.1 when going from the pre-EOS to the EOS era. As the observing system improves forecast errors go down and so does the impact of any particular observing system (in absolute value).

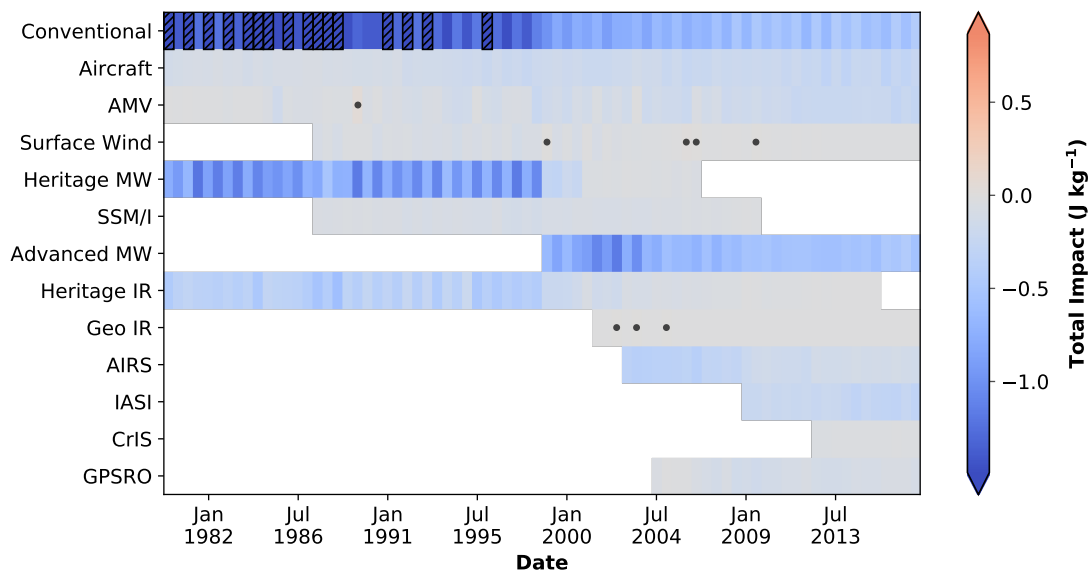
Figure 4.8 - Total impact during the pre-EOS (1982-1999, light grey bars) and EOS (2000-2017, dark grey bars) eras. The numbers on the right vertical axis represent fractional of beneficial observations. Note that there are no bending angle observations in the pre-EOS era. The units of total impact are J kg^{-1} and of beneficial impact are %.



SOURCE: Author's production.

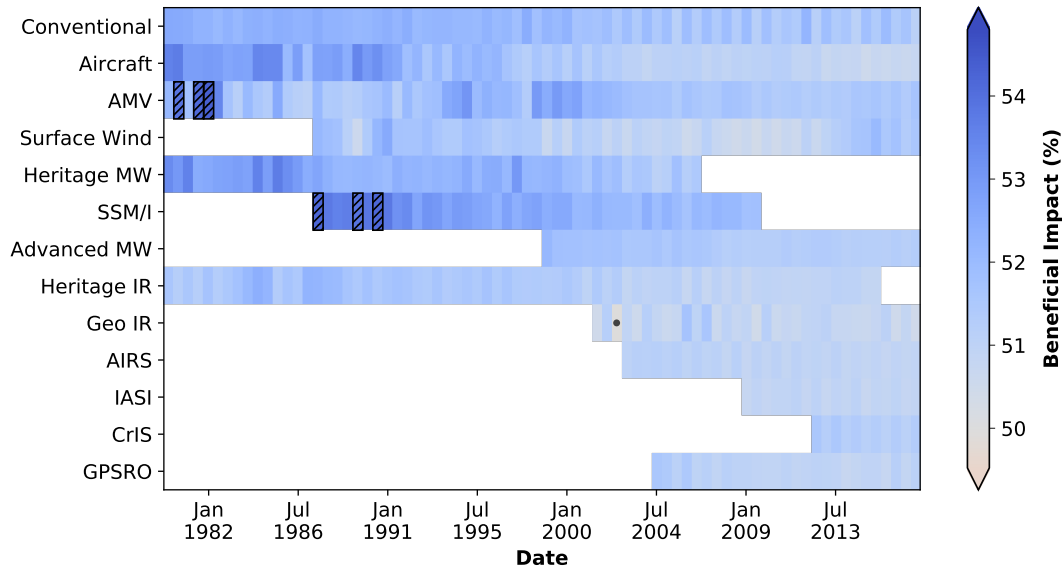
Another possible partition of the residual vectors, and corresponding calculation of the observation impact δe , is to choose I to represent major observing types. Following the partitioning of [McCarty et al. \(2016\)](#) used in [Figure 3.1](#) (page 24), a comparison of the impacts related to the observing classes appears in [Figure 4.9](#) together with corresponding beneficial impacts in [Figure 4.10](#). As before, the figures display time-series covering most of the period of MERRA-2 and the months of January and July. Hatched patches highlight results showing impacts above three standard deviations of the total mean impact displayed in the figure. It is quite evident from this that Conventional observations play the main role in MERRA-2 during the pre-EOS era. The second most important contribution to the impact in the same period comes from the so-called Heritage MW instruments, i.e., MSU on early National Oceanic and Atmospheric Administration (NOAA) satellites [Television Infrared Observation Satellite-N (TIROS-N), NOAA-6-9, 11, 12, 14]. This is followed by the impact from SSU and HIRS-2 (Heritage IR) on board of the same NOAA satellites. In the eyes of the metric defined in (2.1), the remaining part of the observing system contributes only marginally to reducing errors in the 24-hour forecasts.

Figure 4.9 - As in [Figure 4.6](#) (page 47), but for the major observing systems assimilated in MERRA-2. The categories presented here are the same used in [Figure 3.1](#) (page 24).



SOURCE: Author's production.

Figure 4.10 - As in Figure 4.9 (page 50), but for fractional of beneficial observations. The units are %.



SOURCE: Author's production.

As MERRA-2 enters the EOS era, the impact of conventional observations drops considerably as compared to their impact in the pre-EOS era. That, as seen in Figures 4.1 and 4.2 (pages 39 and 42, respectively), total forecast error improves even under the dramatic drop in Conventional observations seen in the bottom panel of Figure 3.1 (page 24) is demonstration of the higher resolution and better quality of new observations in the EOS era, particularly of the AMSU-A and -B instruments as compared to those of the early period. Indeed, that such reduced Conventional network still shows up as a major contributor in the EOS era can only be attributed to the improvement in background fields brought about by the new instruments. The overall impact of observations is a combination of multiple instruments, though clearly some are of fundamental importance. For example, Figure 4.9 suggests that the AIRS instrument on the afternoon (PM) orbit NASA Aqua satellite has had a good share of the impact from the times of its introduction in 2002. When the IASI instrument is introduced on the Meteorological Operational-A (MetOp-A) platform (and eventually, MetOp-B), the influence of AIRS seems to diminish, even though MetOp satellites are placed in different morning (AM) orbits. The contribution from the Joint Polar Satellite System (JPSS) CrIS instrument, which is in an orbit concurrent with AIRS on Aqua, is seen as less significant than that of AIRS. This

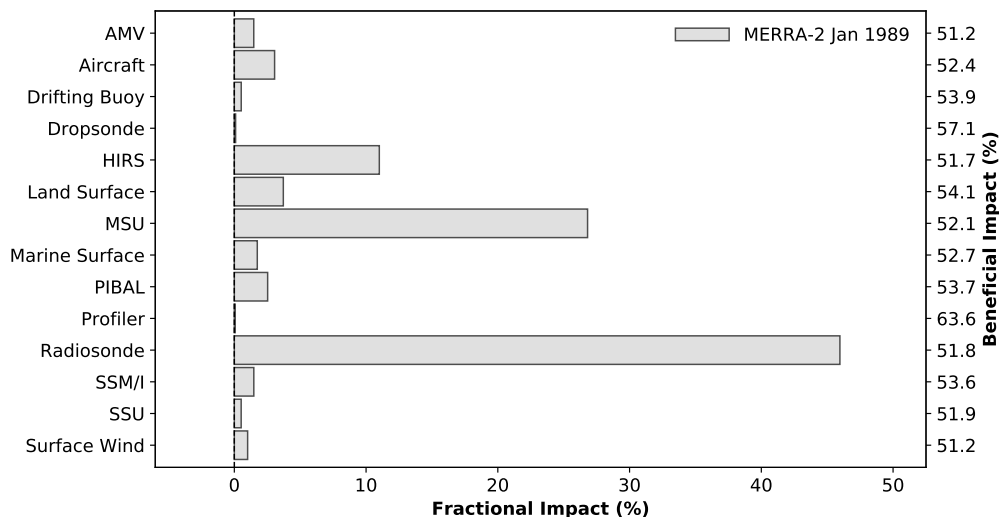
is likely due to the not-so-ideal choice of highly-correlated CrIS channels made in MERRA-2, and its corresponding GEOS FP system (see Section 2.3.1 of [McCarty et al., 2016](#)). That instruments which typically contribute to improve the forecast error metric under consideration can actually, at times, deteriorate results can be seen from the red-shaded bars in Figure 4.9. Typically these are of weak intensity and are highlighted with black dots. This is the case for some of the early GOES IR observations and for some surface wind observations (see what follows).

Before moving on to examine more specific partitions of the observing system it might be instructive to show results for specific months of given years since these more easily compare with results found elsewhere. The January fractional impacts (bars) for 1989 and 2015 are displayed in Figures 4.11 and 4.12, respectively. The figures also show the fraction of beneficial impact indicated for each case along the right vertical axis. The figure breaks down the observing system in a more traditional format, such as found in, for example, the works of [Langland and Baker \(2004\)](#), [Gelaro et al. \(2010\)](#), [Lorenc and Marriott \(2014\)](#), and others. As expected, the break down of the observing classes is not the same in both figures since the observing system changes quite substantially between 1989 and 2015. The two years selected here intentionally coincide with two of the years chosen in [Horányi \(2017, Figures 6 and 9 there\)](#). Though the results here can be compared with those of [Horányi \(2017\)](#), one must be cautious and recall the remark made earlier that DFS and FSOI do not quite give the same information. Indeed, [Horányi \(2017\)](#) finds DFS to indicate the somewhat surprising dominance of HIRS over MSU in 1989 (and earlier), whereas the FSOI results in Figure 4.11 show the expected dominance of MSU over HIRS in MERRA-2. Comparing 1989 with 2015 we find Radiosondes to dominate the fractional impacts, but the magnitude being considerably lower in the latter period. In 2015, [Horányi \(2017\)](#) finds the fractional DFS of IASI to be slightly larger than that of AMSU-A; here, in January 2015, the fractional impact of AMSU-A is larger than that of IASI, which is typical of most other systems. In both [Horányi \(2017\)](#) and here, Aircraft ranks fourth in 2015, but relative to various instruments the fractional contribution from GPSRO seems to be more noticeable in MERRA-2 than in ERA5, for this period.

Figure 4.12 also shows January 2015 results from the GMAO near-real-time system (FP). This allows for comparison of NWP results with those obtained for MERRA-2. In doing so, we should bear in mind the resolution difference between the 50 km MERRA-2 system and the 25.5 km GEOS FP 3D-Var system at that time³. More

³The current GEOS FP exercises a Hybrid 4D-EnVar system at a resolution of 12.5 km.

Figure 4.11 - Fractional impact during January of 1989. The horizontal axis represents fractional impact; the right vertical axis indicates fraction of beneficial observations for each category. The units of fractional and beneficial impacts are %.

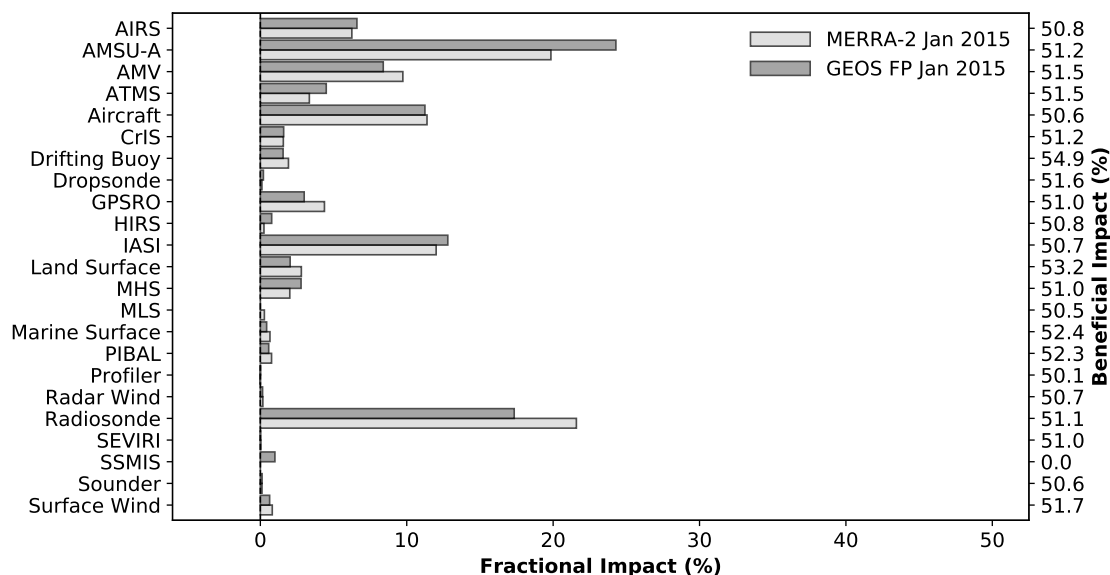


SOURCE: Author's production.

significantly are the differences in the observation blend in these two GMAO systems. For example, MLS temperatures are not (yet) used in FP; aircraft temperature observations are not (yet) bias corrected in FP; GPSRO is used up to 60 km in FP, as opposed to 30 km in MERRA-2; this latter does not make use of GPSRO from the MetOp-B satellite; and unlike MERRA-2, FP makes use of SSMIS (MW) brightness temperatures. Their observing system also differ in sources of ozone observations, but FSOI is not derived for such observations in either case. Other differences are in the details of the tuning of various physical parameterizations between the model versions in these systems, including the fact that no precipitation forcing is applied to FP. The most evident difference in the results displayed here is that AMSU-A dominates the fractional impacts followed closely by Radiosondes in FP, whereas in MERRA-2 the order of these observing types is swapped. The fractional dominance of these two observing types is always very close and it is frequently interchanged when looked at as monthly contributions⁴. The fractional impact ranking of all other observing systems is very comparable between FP and MERRA-2.

⁴The reader is invited to visit the FSOI live GMAO monitoring website at https://gmao.gsfc.nasa.gov/forecasts/systems/fp/obs_impact/, where it is typical to see Radiosonde dominating the fractional impacts, followed closely by AMSU-A and Geostationary winds.

Figure 4.12 - As in Figure 4.11 (page 53), but for January of 2015. For reference, the fractional impact for GEOS FP is also shown (dark grey bars).



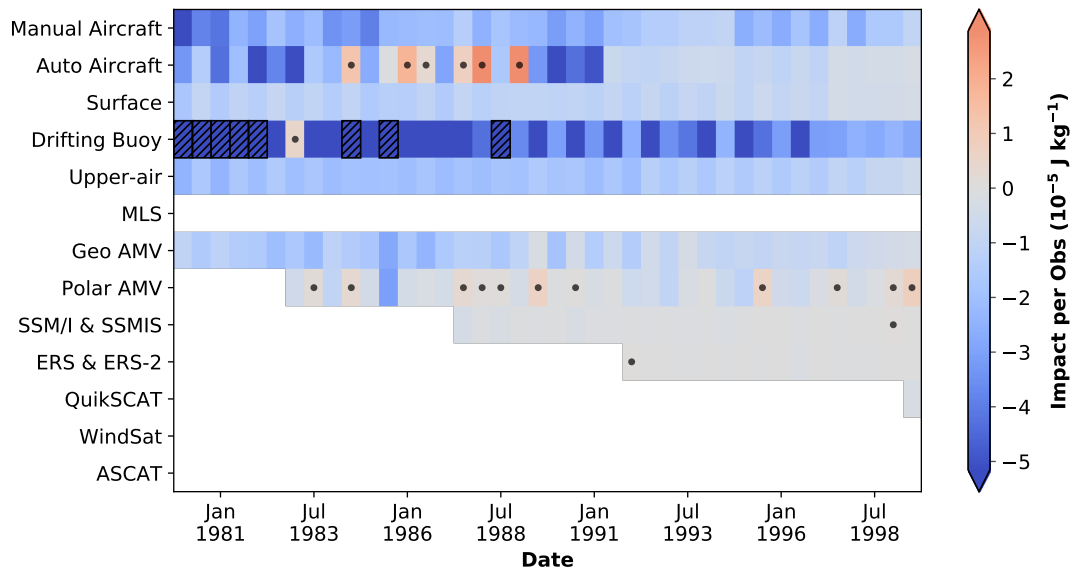
SOURCE: Author's production.

4.4 Conventional, Aircraft, AMV and Surface Wind

Figures 4.13 and 4.14 provide closer examination of the categories named Conventional, Aircraft, AMV, and Surface Wind seen in Figure 4.9 (page 50) but now displaying *impact per observation* instead of total impact. This is analogous, though not identical, to the so-called observation influence, defined as DFS per observation. Following Rienecker et al. (2008, see Table 3.5.4 there), the Aircraft category of Figure 4.9 is now split into two-subcategories, namely: Manual and Automated; these represent two distinct data quality assigned different observation errors. The Conventional category of Figure 4.9 is now split into Surface, Drifting Buoy, Upper-Air (Radiosondes and Profilers), and MLS (Microwave Limb Sounder) retrieved temperature. The AMVs are split into Geostationary and Polar. And finally surface winds are split into SSM/I & SSMIS (SSM/I Sounder), ERS & ERS-2 (European Remote Sensing), QuikSCAT, WindSat, and ASCAT (Advanced Scatterometer). It might be somewhat atypical to include MLS temperature retrievals in the Conventional category, but this is how McCarty et al. (2016) has it. The impact of the observing classes here is considerably affected by the transition of MERRA-2 into the modern period. So much so that to allow for color scales to reveal any significant informa-

tion it is necessary to split the picture into a pre-EOS and EOS period, and use different color scales for each case. Notice that the impact (per observation) reduces by almost an order of magnitude going from the pre-EOS to the EOS period.

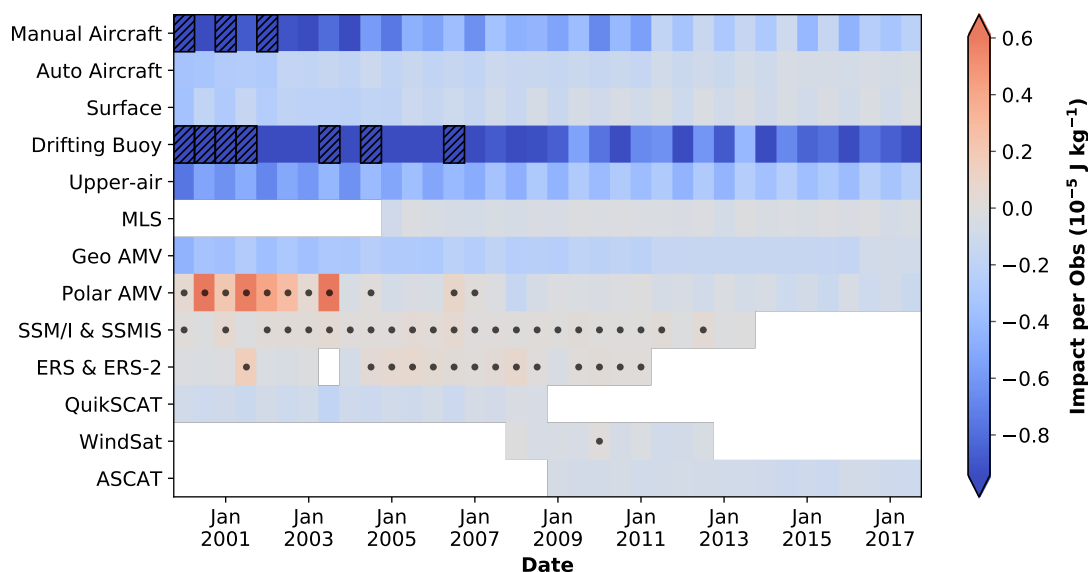
Figure 4.13 - Heatmap of monthly mean impact per observation for Conventional, Aircraft, AMV and Surface Wind observations presented in Figure 3.1 (page 24) during the pre-EOS era (1980-1999). The Conventional category is split into three subcategories: Surface, Drifting Buoy, Upper-Air, and MLS; the Aircraft into two: Manual and Automated; the AMV into two: Geostationary and Polar; and the Surface Wind into five: SSM/I & SSMIS, ERS & ERS-2, QuikSCAT, WindSat and ASCAT. Values are for 0000 UTC analyses during months of January and July. Patched boxes represent monthly mean values with ± 3 standard deviations from the total mean impact displayed in the figure and dots represent boxes with negative values. The scale factor is 10^{-5} and the units are J kg^{-1} .



SOURCE: Author's production.

On a per-observation basis, the contribution from Drifting Buoy observations far exceeds that of any other instrument shown in the figure, throughout the MERRA-2 period; if nothing else, there are very few such observations, strategically positioned, sometimes being the single source of information on passing storms. This results is consistent with results from Horányi (2017) who finds drifting buoys to dominate observation influence in all ERA5 years examined there. In the pre-EOS era, Aircraft

Figure 4.14 - As in Figure 4.13 (page 55), but for the EOS era (2000-2017).



SOURCE: Author's production.

observations come next, followed closely by Upper-air, Surface and Geostationary AMVs. The automated Aircraft reports go through a period of “instability” in the mid-1980’s, when observations were not very dense, and their contribution actually degrades the forecast error reduction measure (2.1). Global maps of the location of these observations reveal them to amount to very sparse flights spread over the globe, depending on month and year (not shown). As MERRA-2 gets into the EOS era, and the automated observations become standard, and substantially increase in volume, their impact per observation stabilizes and their contribution becomes safely in the direction of reducing forecast errors just as much as Surface and Geostationary AMV observations.

In the EOS era, after Drifting Buoy, Manual Aircraft shows significant impact on a per observation basis, especially in the early to mid 2000’s. Through in this period, the impact of Upper-Air observations is substantial and steady. Also in this era, MERRA-2 assimilates MLS observations (ozone and temperature) from 2004 and beyond; the figure accounts only for retrieved temperature profiles, which are assimilated at or above 5 hPa (40 km). Although these data have been shown to be a strong player in determining the dynamics of the stratopause and lower mesosphere (GELARO et al., 2017; LONG et al., 2017), their contribution to reducing the

forecast error metric (2.1) is rather neutral. One must bear in mind that the vertical weights provided by the energy operator defining the matrix \mathbf{C} are rather small above 10 hPa and it would be surprising to see any data above this level to show significant contribution to error reduction.

When it comes to surface wind observations, the heatmap results of Figures 4.13 and 4.14 seem to suggest their contribution to be neutral, such as that from pre-EOS QuikSCAT, to marginally positive, as from QuikSCAT and ASCAT in the EOS era. Here again, one must be careful interpreting the results in light of the relatively low weights imposed by the total energy norm defined by the matrix \mathbf{C} near the surface (see Figure 2.3, page 17). Indeed, different norm weights would lead to different results. Additionally, the representation of near-surface physical processes in the model adjoint is much too simplified as compared to the complex boundary layer representation of the full nonlinear model. Even with such caveats it is noticeable that the contribution from QuikSCAT improves as the system goes from the pre-EOS into the EOS era; this is likely the case where other (new) instruments of the EOS era help the system make overall better use of existing instruments.

Finally, in all of the results seen in Figures 4.13 and 4.14 (as well as those from Figures 4.6, 4.7, 4.9 and 4.10, pages 47, 48, 50 and 51, respectively) a certain seasonality is noticed with January results being slightly larger than in July. This is understandable since the bulk of the observations considered in these figures are in the Northern Hemisphere, and January is when the largest forecast sensitivities are found (see Figure 4.3, page 44), during the winter period of this hemisphere.

4.5 Radiosonde

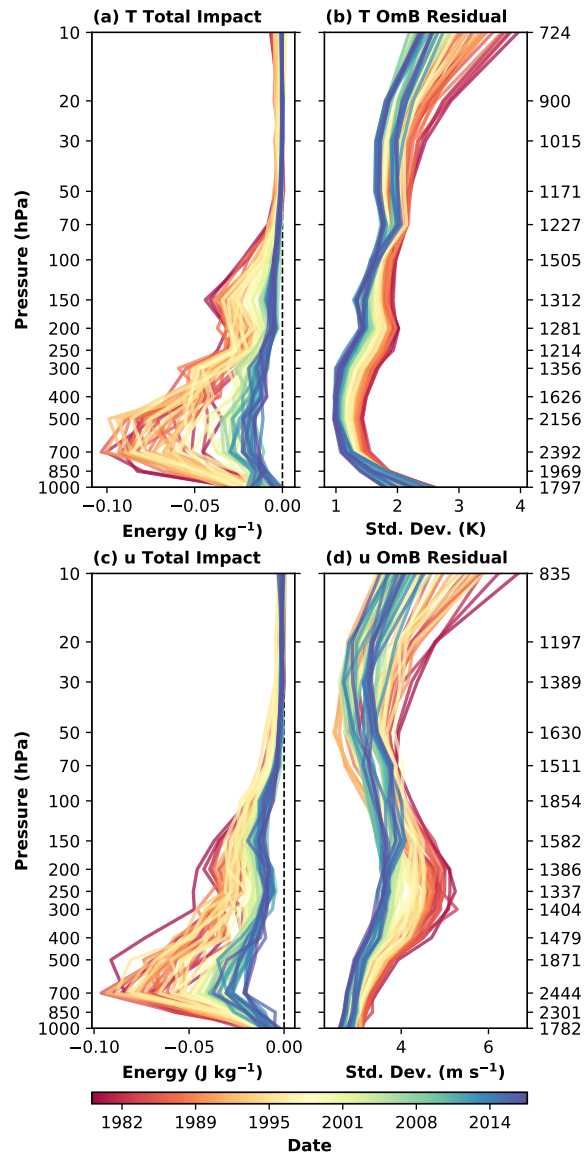
Vertical mean profiles can also be derived from the impacts, just as typically done elsewhere for examining observation-minus-background (OmB) residuals. As an illustration, the left panels of Figure 4.15 show vertical profiles of monthly averaged impacts in the 0000 UTC analyses of all January and July months from 1980 to 2017 for radiosonde observations of temperature and zonal wind. For reference, the right panels of the figure show corresponding monthly OmB standard deviations for the quantities on left. Numbers in the right vertical axis represents the mean observation count for each layer. It is noticeable that the bulk of the impact in both variables is concentrated in the layer between 850 and 100 hPa. It is also noticeable from the coloring of the curves in figures that there is a transition from the initial years of the reanalysis to more recent years when the impacts become smaller in absolute value, and do the residual standard deviations. This transition is seen

even when the observation counts are factored in, by looking at fractional impacts (not shown), and thus rules out the influence of the number of observations in the results. The reduced impact of the radiosonde observations in the modern period is attributed to the improvement in the background over time as induced by the effective contribution from modern observing systems.

An illustration of the betterment of the background fields is provided in Figure 4.16. Using the observation residual diagnostic of Desroziers et al. (2005) the figure displays background and observation error standard deviation for radiosonde (a) temperature and (b) zonal wind. The estimates are shown for January and July, and are derived over two separate periods, namely, the pre-EOS (1982-1999) and EOS (2000-2017) eras. Background errors are smaller in the modern era as compared to their estimates over the 1980's; the reduction in tropospheric error is noticeably dramatic in the zonal component of the wind. The dots along the curves indicate the statistical significance of a t -test for the means of two independent samples, assuming that the samples do not have equal population variance, that is the Welch's version of t -test. The size of these dots is associated with the significance level as indicated in the figure. The numbers in the right vertical axis are the mean observation count for the pre-EOS era and, in parenthesis the difference of the count of the pre-EOS era with the EOS era; a positive value being indicative of the reduction in count over the more recent period. Observation errors show smaller variations in the vertical than the corresponding background errors do. Observation errors for temperature are somewhat reduced, almost consistently throughout the column, in the EOS era as compared to the pre-EOS era, with exception of the layer between 100 to 70 hPa. Observation errors for zonal wind are nearly unchanged below 500 hPa and above 30 hPa, with results about jet level being somewhat reduced in the EOS era, but somewhat increased between 150 and 30 hPa in the same EOS era.

The GSI 3D-Var specifies fixed observations errors throughout the reanalysis period. The varying observation error estimates in the figure suggest that an optimal analysis should benefit from a prescription allowing for time-varying observation errors. As in typical 3D-Var implementations, the prescribed background error is also fixed throughout the reanalysis, but its estimated value clearly changes with time; the change in the zonal component of the wind along the jet level is rather substantial. This reduction (change) in background error along the reanalysis period is unsurprisingly a clear motivation for the implementation of more advanced analyses procedures, capable of automatically adjusting to changes in the background. In other words, four-dimensional variational data assimilation (4D-Var) and hybrid

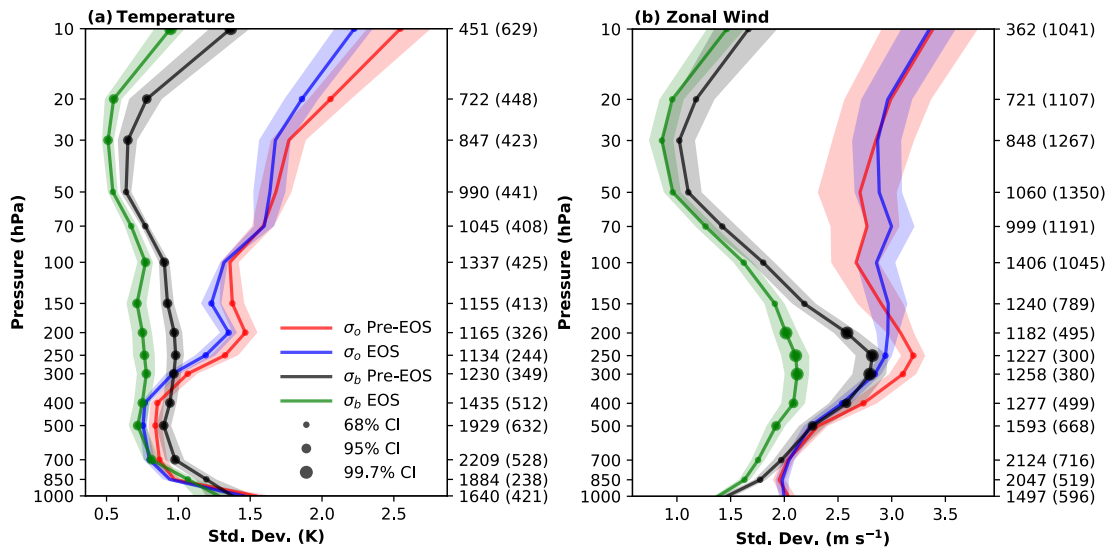
Figure 4.15 - Monthly mean vertical profiles of total impact [left: (a) and (c)] and standard deviation [right: (b) and (d)] of observation-minus-background (OmB) residuals for temperature [top: (a) and (b)] and zonal wind component [bottom: (c) and (d)]. The column on the right represents mean number of observations per analysis in each layer. The units of energy are J kg^{-1} and of standard deviation of temperature and zonal wind component are K and m s^{-1} , respectively.



SOURCE: Author's production.

ensemble-variational methods are bound to be better approaches for reanalysis. The impact of these error reductions in the analyses can be further illustrated by look-

Figure 4.16 - Vertical profiles of estimates of background (green and black) and observation (blue and red) error standard deviations for (a) temperature and (b) zonal wind obtained from the radiosondes during the pre-EOS (1982-1999; red and black) and the EOS (2000-2017; blue and green) eras. Lines represent mean values with ± 1 standard deviation from the mean in shading for 0000 UTC analyses during months of January and July. The column on the right represents mean number of observations per analysis in each layer for the pre-EOS era and in parenthesis the difference subtracting EOS from pre-EOS era. The dots represent the statistical significance between the eras. The units of standard deviation of temperature and zonal wind component are K and m s^{-1} , respectively.



SOURCE: Author's production.

ing at a “pseudo” scalar gain, $\sigma_b^2/(\sigma_b^2 + \sigma_o^2)$, that can be calculated directly from the background (σ_b) and observation (σ_o) errors in Figure 4.16, assuming the corresponding error covariances to be diagonal. This simple calculation reveals clearly the reduced effective weights given to radiosonde observations in the modern era as compared to the early periods (more on this below). This happens simply because of the introduction of other instruments competes with, and in many respects takes it away from, the contribution of radiosondes.

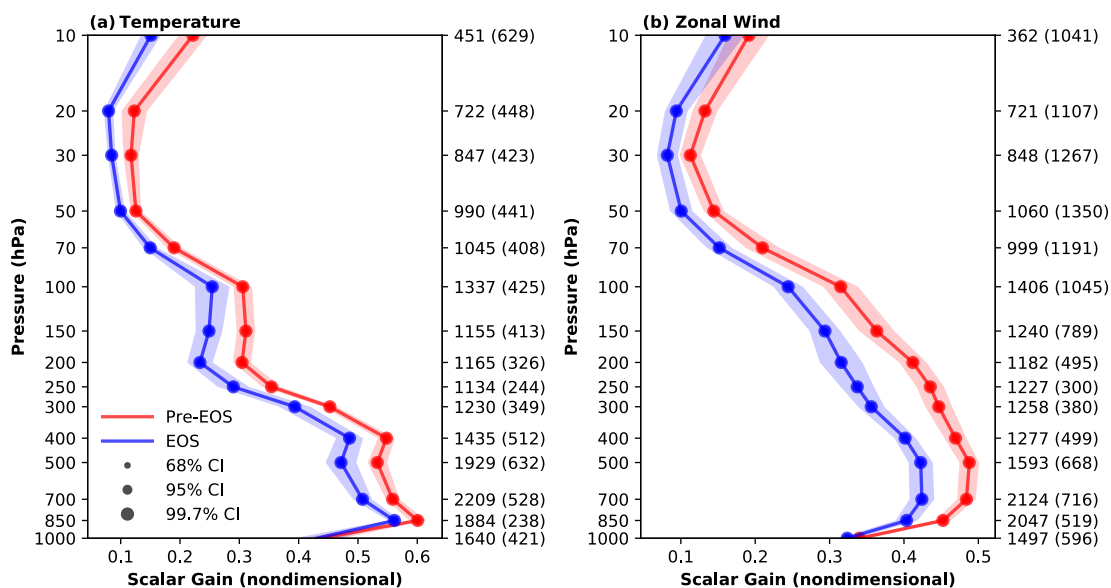
An important fact to remember about MERRA-2 is that it relies on a 3D-Var algorithm with prescribed, fixed, observation and background error covariances for the whole course of its integration. Indeed, MERRA-2 is derived from GMAO FP,

near-real-time, system. The prescribed errors of this system are tuned to provide best results over the current period, and therefore, one might expect the system to perform less optimally over other periods. The only quasi-adaptive feature of the MERRA-2 3D-Var is its online variational bias correction (DERBER; WU, 1998) and an offline aircraft bias correction procedure. These, however, adjust biases in satellite radiances and aircraft temperature observations but not observation and background error covariances. An illustration of the difference in tuning is provided here in Figure 4.17, where scalar analysis gains derived from observation residuals of radiosonde temperature in panel (a) and winds in panel (b) are shown for the pre-EOS and EOS era of MERRA-2. These quantities are constructed from estimates of background and observation error standard deviation over the eighteen years of January and July months preceding the EOS era (1982-1999) and during the EOS era (2000-2017). If it is assumed that the system to be tuned for the current (EOS) era, the results in the figure suggest the errors associated with the pre-EOS era to be in need of tuning, i.e., requiring an adjustment of the prescribed statistics. It is important to note that the x-axis is not kept the same among the panels (a) and (b). This helps identify that temperature observations present slightly larger scalar analysis gains when compared to wind observations.

4.6 Radiance

Two of the most compact ways to subset radiance observations and their impact on forecast error reduction are shown in Figures 4.18 and 4.19: by platform, and by sensor, respectively. The figures actually display *fractional* impact where the fractions are calculated with respect to the whole observing system considered for each particular period. The continuous grey curve — equal in both figures — shows the time series of total radiance fractional impact for each period, and equates with the total impact strip of brightness temperature shown in Figure 4.6 (page 47). It is noted from the curve here that the fraction of satellite radiances contributing to reduce forecast errors ranges from the mid 30% to nearly 60%. The fractions show a steady rise from the mid-1990's to early 2000's, then slightly fall back down to rove around 47% in the modern era. This reduced fractional impact can be traced to an slight increase in the fractional impact of conventional wind observations — likely from aircraft data (not shown). The size of the bubbles in Figure 4.18 corresponds to the average number of observations in that subset class. The largest bubbles are found further to the right in the two figures, after the Aqua, MetOp and JPSS platforms are launched and the high-spectral IR instruments AIRS, IASI and CrIS become available.

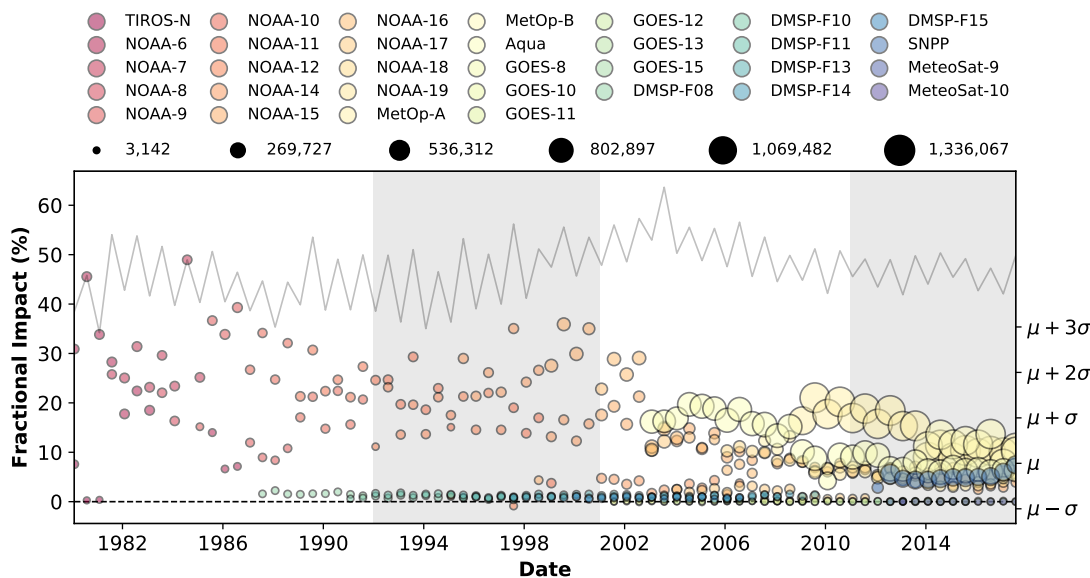
Figure 4.17 - Vertical profiles of estimates of Kalman gain, $\sigma_b^2/(\sigma_b^2 + \sigma_o^2)$, in observation-space for radiosonde residuals of (a) temperature and (b) zonal wind obtained for the 0000 UTC analyses of the January and July months of the pre-EOS (1982-1999; red) and the EOS (2000-2017; blue) eras. Curves represent mean values; shading represents ± 1 standard deviation from the mean. The column on the right represents mean number of observations per cycle in a particular layer for the pre-EOS era and in parenthesis the differences from the pre-EOS era.



SOURCE: Author's production.

Closer examination of Figure 4.18 shows the modern period to have a larger blend of different platforms than the early pre-EOS period, with the consequence that the fractional impact from platforms contributing most is smaller than what is seen from the dominant platforms in the early periods. In other words, the modern platforms share the contribution among themselves without any single one of them dominating above levels achieved by past platforms. Notice that the pre-EOS era typically has 3-to-4 simultaneous platforms, in contrast with the modern period when 9-to-10 platforms are found to operate simultaneously. As mentioned above, the overall contribution from satellite observations in the modern period is still larger, in the mean, than what is seen in the early periods, but not dramatically so. Clearly, this is not a statement about the quality and quantity of the observations brought about by new platforms (and instruments). As a matter of fact, we have seen a quite substantial improvement in forecast error in the modern era over the earlier periods

Figure 4.18 - Monthly mean fractional observation impact for all radiance grouped as satellite platforms. Only results for 0000 UTC analyses during months of January and July are included. The line represents the sum of all bubble values for each month. The size of the bubbles is proportional to the monthly mean observation count for each partition of the observing system. The units of fractional observation impact are %.



SOURCE: Author's production.

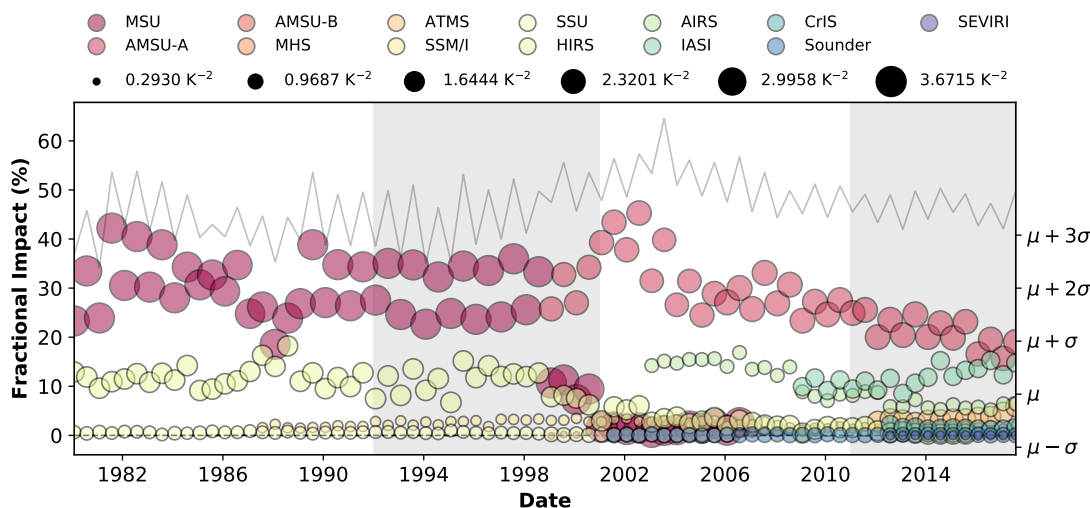
(see Figures 4.1 and 4.2, pages 39 and 42, respectively) and that can only be attributed to changes in the observing system, and specifically changes in both quality and quantity of satellite observations. Also noticed in the figure is the fact that in the pre-EOS era the TIROS-N and the NOAA series of satellites up to NOAA-14 dominate the fractional impact; the fractional contribution from the early GOES satellites is very small. Indeed, even in the modern era, the fractional contribution from these platforms, as well as the Defense Meteorological Satellite Program (DMSP) and Meteorological Satellite (MeteoSat), is minor, but one has to associate their contribution with the difficulties in making proper use of the instruments they carry (see below).

The dominant platforms are the ones carrying the dominant instruments. This is seen from examining Figure 4.19. Directly associated with the comments above, we see from the figure now that in the pre-EOS era the MSU and HIRS instruments on the TIROS-N and pre-NOAA-15 satellites dominate the fractional impact of radiances.

Close examination of the impact of these instruments identifies a period in the mid-1980's when their fractional impact nearly equals. However, in no time throughout the MERRA-2 pre-EOS period the impact of HIRS surpasses that of MSU as seems to be the case in the DFS results of Horányi (2017) for selected months in 1979 and 1989 of ERA5 (Figures 5 and 6 in that work). The fractional impact from SSU (NOAA-6-9,11,14) shows as being minor, though as anticipated previously the weighting matrix \mathbf{C} defining the forecast error measure (2.1), page 12, provides very little weight in the stratosphere where the SSU contribution is mostly influential; the three SSU channels used in MERRA-2 peak on or above 15 hPa (channels 1, 2, and 3 peak at about 15, 5, and 1.5 hPa, respectively). Around 1999 and in the early 2000's the AMSU-A instrument start dominating the fractional impact, swamping the contribution from MSU (still available for a short period of time on NOAA-11, and for several years on NOAA-14). After AMSU-A's peak contribution in its early days its contribution is reduced when the AIRS (Aqua) is introduced; the AMSU-A contribution continues to reduce further as IASI (MetOp-A and -B) and more recently ATMS (JPSS) become available. Similarly, the consistent contribution from the HIRS instrument in various platforms of the pre-EOS era dwindles down as ATOVS replaces TOVS, and more so, when the hyperspectral AIRS instrument is introduced. The fractional impact of AIRS is reduced after IASI becomes available; and then its fractional impact is further reduced when CrIS starts being assimilated. Sounder (GOES), SSM/I (DMSP), and SEVIRI (MeteoSat) all show low fractional contributions, but as mentioned above these are complex observations, typically highly thinned in GSI (due to cloud screening), which the analysis does not make effective use of.

In all of the discussion of Figures 4.18 and 4.19 one must bear in mind that the contribution brought about by various observing systems is indirectly dependent on the weight the (GSI) analysis gives to each particular instrument. A precise measure of the overall weight associated with a given instrument is difficult to obtain since observation errors are assigned to each particular channel provided by any instrument. Nonetheless, it is instructive to try to associate observation impacts to some measure of analysis weights. In Figure 4.19, the size of the bubbles represents an estimate of the analysis weights given to a particular instrument. These weights are estimated by averaging the inverse observation error variance of each used channel, of a given instrument and in a given cycle, over the channels of the corresponding instrument, and then averaging the results for each cycle over the month of relevance. From these we can tell, for example, that the two most heavily weighted instruments throughout the reanalysis are MSU and AMSU-A. At first

Figure 4.19 - As in Figure 4.18 (page 63), but for sensors. The size of the bubbles is proportional to the inverse of the observation error variance assigned before the assimilation for each partition of the observing system. The units of fractional observation impact are % and of the inverse of the observation error variance are K^{-2} .



SOURCE: Author's production.

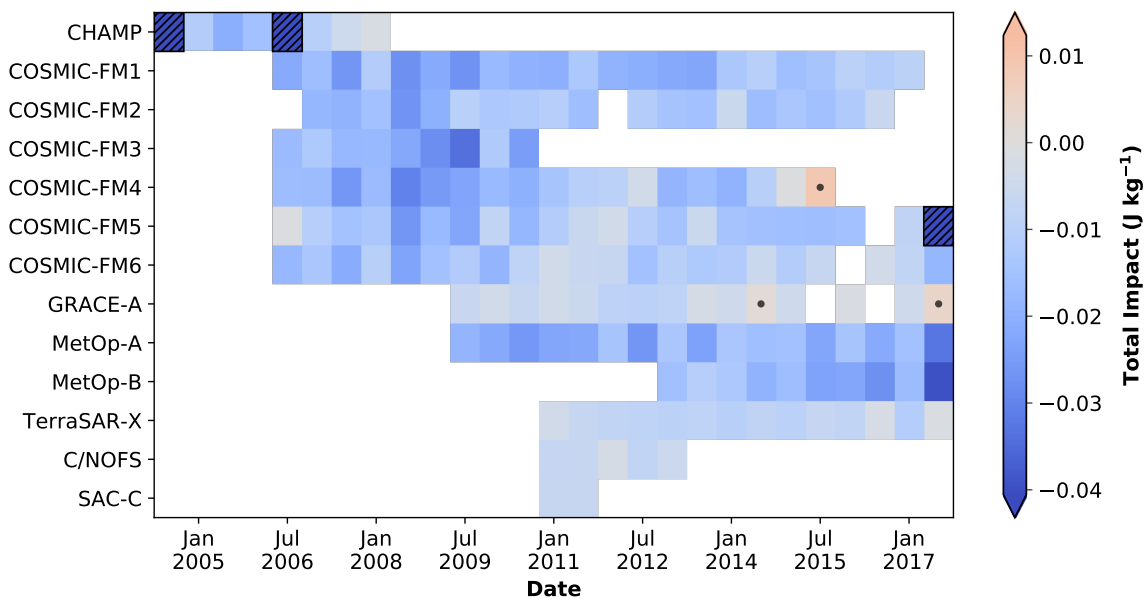
glance these are the instruments with the highest fractional impact. In the pre-EOS era, the HIRS instrument also receive a considerable amount of weight, and it is the second largest fractional impact during that period superseded only by MSU. However, higher weights are not always necessarily directly associated with larger fractional impacts. The overall weight given by the analysis to AMSU-A is noticeably smaller than the weight given to MSU, and still, if we examine the period when these two instruments work concurrently (1998-2006), the fractional impact from AMSU-A dominates that from MSU. This is attributed to AMSU-A providing better estimates of the atmospheric vertical structure than MSU. Similarly, the pre-EOS HIRS instruments are given more weight than any of the hyperspectral IR instruments of the modern era, and yet the fractional impact of the hyperspectral instruments is at comparable levels to the impacts from HIRS. The thinking behind these weighing strategy being that a conservative approach should be taken when handling instruments with considerable inter-channel correlations, such as the hyperspectral sensors, when such correlation are not accounted for in the analysis.

Again, that low-weighted instruments can contribute just as much as high-weighted instruments can only be attributed to the better quality and higher fidelity of the former instrument.

4.7 GPS radio occultation

GPSRO is an observing system that has been shown to have considerable impact in helping improve NWP systems (e.g., Healy and Thépaut, 2006; Cucurull and Derber, 2008). We examine the contribution of this instrument to reanalysis in Figures 4.20 and 4.21. The two figures summarize the impact of GPSRO observations in the results. Similarly to the platform split for brightness temperature observations, Figure 4.20 provides a heatmap of impacts for the various GPSRO platforms; the sum of all these impacts equates with the total impact strip for bending angle shown in Figure 4.6 (page 47).

Figure 4.20 - As in Figure 4.6 (page 47), but for all GPSRO observations grouped as satellite platforms.



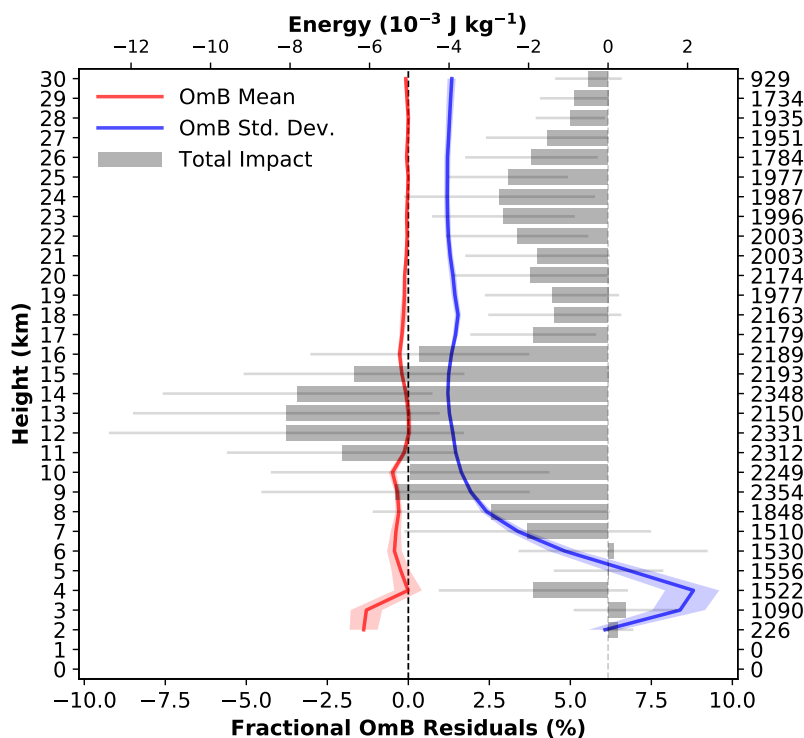
SOURCE: Author's production.

When initially introduced in July 2004, the single platform, Challenging Minisat Payload (CHAMP) shows consistent and strong impact signal with a seasonality

that seems to show larger impacts in the July months. The impact of CHAMP is noticeably reduced when the Constellation Observing System for Meteorology, Ionosphere & Climate (COSMIC) is introduced (July 2006). COSMIC is a cluster of six platforms (FM1-6) spread along different drifting orbits and providing relatively even coverage of the globe. All of the platforms in the constellation seem to contribute fairly evenly to reducing errors in the forecast. When GPSRO observations from MetOp-A and eventually MetOp-B are assimilated their contribution to forecast error reduction seem to be comparable to that of the observations from the COSMIC platforms. The impact from other GPSRO platforms, namely, Gravity Recovery and Climate Experiment–A (GRACE-A), Terra Synthetic Aperture Radar operating in X band (TerraSAR-X), Communications/Navigation Outage Forecasting System (C/NOFS) and Scientific Application Satellite-C (SAC-C) seem smaller than the impact from COSMIC and the MetOp satellites. This being attributed to the sparseness of these “other” platforms.

GPSRO observations have fine vertical resolution and it is worth examining vertical profiles of their impacts. MERRA-2 assimilates GPSRO bending angle observations up to 30 km (approximately 10 hPa) and the vertical profiles of various quantities shown in Figure 4.21 go up to the top of the data utilization level. As these measurements have a height-based vertical coordinate, the vertical coordinate in the y-axis of Figure 4.21 is chosen to be height. The figure shows total mean impact for each 1 km layer in the grey bars with scales indicated on the top x-axis. Also displayed in the figure are the mean and standard deviation of the observation-scaled OmB residuals, that is, of the quantities formed by (d_i/y_i^o) , with scales indicated along the bottom x-axis. Beneficial impacts (grey bars) are seen throughout the column with the exception of levels somewhat near the surface. The bulk of the impact is seen between 7 and 17 km, with smaller but consistent impacts above 17 km and below 6 km. The whiskers placed along the grey bars provide an estimate of the variability of the impacts and only below 6 km these are seen to sometimes contribute in the opposite direction of reducing errors in the forecast. The low and degrading impact at low levels is consistent with the fact that the scaled OmB residuals show considerable dispersion at these levels. Everywhere else along the profile, the standard deviation of the scaled residuals is largely uniform and perhaps less correlated with the impacts themselves. The relatively small impact seen above 17 km might well be a consequence of the mass weighting in the total energy norm used to derive FSOI; weights drop exponentially fast above 300 hPa becoming comparatively small above 70 hPa (~ 17 km), see Figure 2.3 (page 17). Because of this, it is not surprising to see works based on DFS (e.g., Horányi, 2017) to find GPSRO possibly playing

Figure 4.21 - Vertical profile of mean (red, bottom axis) and standard deviation (blue, bottom axis) of fractional observation-minus-background (OmB) residuals, and mean observation impact (bars, top axis). Lines (bars) represent mean values with ± 1 standard deviations from the mean in shading (whiskers) for 0000 UTC analyses during months of January and July. The column on the right represents mean number of observations per analysis in each layer. The units of mean and standard deviation of fractional background residuals are % and of energy are $10^{-3} \text{ J kg}^{-1}$.



SOURCE: Author's production.

a bigger role than that identified in the present evaluation. To a large extent, the findings here are very much consistent with the results in the works of Cardinali and Healy (2014) and Lorenc and Marriott (2014), though month-specific studies such as in these works tend to find deterioration of results above certain levels (e.g., Figure 11 of Lorenc and Marriott, 2014) which is not found in the case of the multi-year averaging results presented here.

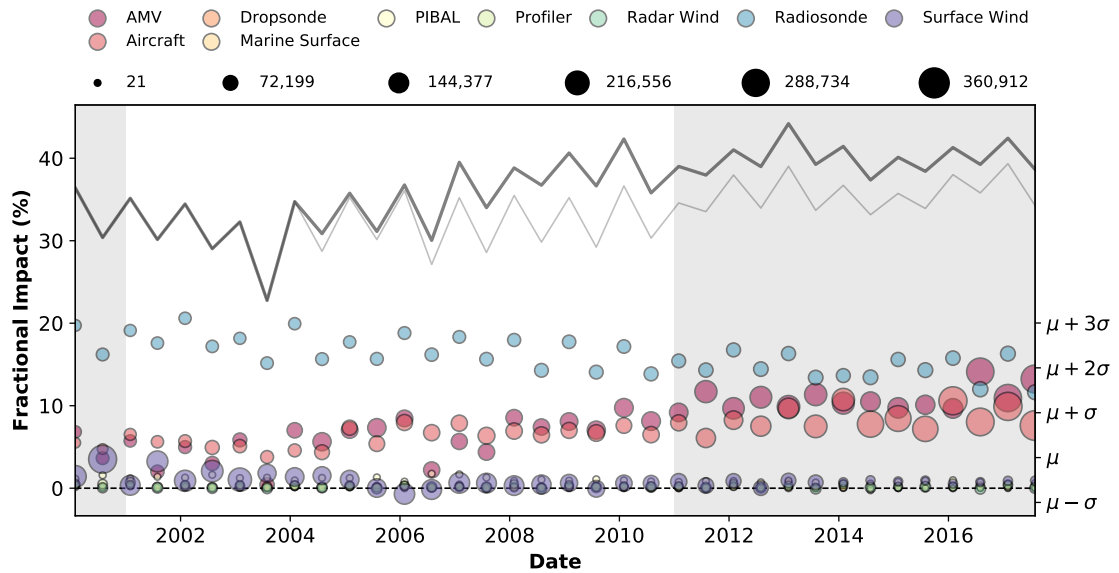
Overall, close examination of results in Figures 4.6 and 4.9 (pages 47 and 50, respectively) show that the GPSRO contributes from as little as 1% to the overall observation impact when first introduced in CHAMP in 2004, to nearly 10% during the main years of COSMIC, to about 5% toward the end of the time series exam-

ined in those figures. To a good extent, these results are in agreement with similar, month-long, estimates found elsewhere, e.g.: 6% in [Cardinali and Prates \(2011\)](#) for June 2009; 2.7% in [Lorenc and Marriott \(2014\)](#) for August-September 2010; and 10% in [Cardinali and Healy \(2014\)](#) for June 2011.

4.8 An interplay of fractional contributions

It has been noticed elsewhere that introduction of a new instrument may, at times, considerably take away the fractional contribution of some other instrument. An example of such interplay occurs in the EOS period, when there is a steady the drop in fractional impact from brightness temperature observations visible in the grey curves of [Figures 4.18 and 4.19](#) (pages 63 and 65, respectively), during the EOS era (same on both figures, see explanation in [Section 4.6](#), page 61). Since fractional impact has to add up to 100%, it should be possible to determine what complementary component of the observing system takes it away from brightness temperature. Close examination of the time series of impacts from other instruments reveals that observations from wind increase their fractional contribution within the same time period as the drop noticed in brightness temperature. A breakdown of the various upper-air wind instruments is shown in [Figure 4.22](#). The thin light grey curve represents the total fractional contribution from wind observations; only data from the EOS era is considered here. Notice that the rise from wind contribution happens just about when the fractional contribution from brightness temperature decreases. The breakdown points to aircraft wind and AMV observations as the main contributing sources. However, wind observations are not the whole story. The drop in fractional impact from brightness temperature is almost 10% of the total impact (from early 2000's to 2017). The increase due to wind is only about 6 to 7%. As illustrated by the thick dark grey curve in [Figure 4.22](#), GPSRO explains where the remaining fraction goes. Indeed, GPSRO contributes from as little as 1% when CHAMP is introduced in 2004, to almost 10% during the main years of COSMIC, to about 5% toward the end of the time series examined in the figure — these percentages are directly extracted from the difference between the two solid curves in [Figure 4.22](#). To a good extent, these results are in agreement with similar, month-long, estimates found elsewhere, e.g.: 6% in [Cardinali and Prates \(2011\)](#) for June 2009; 2.7% in [Lorenc and Marriott \(2014\)](#) for August-September 2010; and 10% in [Cardinali and Healy \(2014\)](#) for June 2011.

Figure 4.22 - As in Figure 4.18, but for various sources of wind observations. The thin light grey curve represents the sum of fractional impact from all wind observation sources. The thick dark grey curve adds the contribution from GPSRO to those of wind observations.



SOURCE: Author's production.

5 FSOI APPLICATION TO REANALYSIS OVER THE AMAZON

This chapter is a follow-up work of the results presented in Chapter 4, focusing on the observation impacts over the Amazon basin in South America. Although the observation impacts presented in this chapter are for a confined region, it is essential to say that these impacts represent the contribution to the reduction of the global forecast error measure presented in Chapter 4. In other words, the results presented in this chapter relates to the usage of the observations over the Amazon basin in the presence of all other observations outside the Amazon basin.

5.1 Introduction

Chapter 4 provides a comprehensive assessment of the impact of the observations on short-range (24-hour) forecasts from a multi-year reanalysis. Unlike typical examination of root-mean-square error of observation residuals that inherit the unit of the variables being examined and are thus not suitable for cross-comparison, the FSOI technique employed in Chapter 4 standardize units and thus allow for cross-comparison. FSOI was introduced by [Langland and Baker \(2004\)](#), and it has since become a standard tool for assessing the plethora of observations assimilated in global operational NWP systems. One disadvantage of relying on, say, time series of FSOI results from NWP applications is that these are affected not only by changes in the observing system but also by changes in the rest of the system, namely, updates to the underlying model and changes in the data assimilation technique being used in operations. Most FSOI studies in the literature have been carried out over short periods, with fixed versions of the corresponding NWP systems (e.g., [Langland and Baker, 2004](#); [Gelaro and Zhu, 2009](#); [Gelaro et al., 2010](#); [Cardinali, 2009a](#); [Ota et al., 2013](#); [Lorenc and Marriott, 2014](#); [Buehner et al., 2018](#)). Jumps in NWP datasets due to system upgrades have long been recognized as undesirable, rendering such datasets unsuitable for climate and long-term studies (e.g., [National Research Council, 1991](#)). Reanalysis provides a relatively better alternative since it is unaffected by system upgrades of any kind; its results are only affected by changes in the observing system. In many ways, reanalysis provides an ideal environment for conducting FSOI studies.

The study in Chapter 4 rely on the MERRA-2, which is an ongoing exercise with now nearly 40 years of assimilated products available for climate studies. Though not used in its ongoing integration, MERRA-2 has all necessary ingredients to perform FSOI, namely, an adjoint model ([HOLDAWAY et al., 2014](#)) of its nonlinear general circulation model, and an adjoint ([TRÉMOLET, 2008](#)) of its three-dimensional variational

analysis. FSOI requires the introduction of a forecast error measure (or metric), and it evaluates the sensitivity of this measure to changes in the observations. Implicit in this evaluation are sensitivities of forecasts to changes in the initial conditions, which are derived from the model adjoint. Since such adjoint models are only valid over relatively short periods, FSOI results are typically derived for the 24-hour forecasts. More specifically, the technique of [Langland and Baker \(2004\)](#) also requires the availability of 30-hour forecasts, valid at the same time as the 24-hour corresponding ones, to allow for a relatively accurate FSOI estimate (see [Errico, 2007](#); [Daescu and Todling, 2009](#)).

Results presented in Chapter 4 shows that, unlike other regions in the tropics, the Amazon basin forecast sensitivities change rather substantially from the first half of MERRA-2 to its latter half, with a consequent increase in forecast error. These changes are associated with changes in the observing system. The potential impact of tropical heat sources in producing teleconnection patterns which can be a source in forecast errors elsewhere over the globe is one the motivations of this chapter. In the Amazon basin context, [Grimm and Dias \(1995\)](#) presents results for the potential impact of the South America heat sources. The objective of the present study is to provide an assessment of the impact of observations in short-range (24-hour) forecasts for the Amazon basin from 1980 to 2017 and to shed some light on the reasons for such increased error growth. This assessment is a focused evaluation extracted from the global evaluation of Chapter 4. Although the work here relies still on the global forecast error metric employed in that work, conclusions are not expected to change in any significant way by the use of a regionally-specific projection metric. Indeed, work has been done showing that global error measures are just as effective in obtaining regional results as regionally projected measures are (see Sec. 3.2 of [Boullot et al., 2016](#)). This holds as long as the essence of the metric remains the same, specifically for the case here, as long as results are still sought out for total energy and not some other error measure based on, say, circulation or vorticity or something else. Directly related to these statements is the fact that any assessment that relies on the specification of a norm depends on that norm; thus, a change in the norm might, in some cases, change the results and corresponding conclusions. Examination of different norms is not part of the present work; readers interested in applications using alternative norms are referred to typical few-month-long evaluations such as those of [Todling \(2013\)](#), [Sommer and Weissmann \(2016\)](#), [Necker et al. \(2018\)](#), [Cardinali \(2018\)](#), [Kotsuki et al. \(2019\)](#).

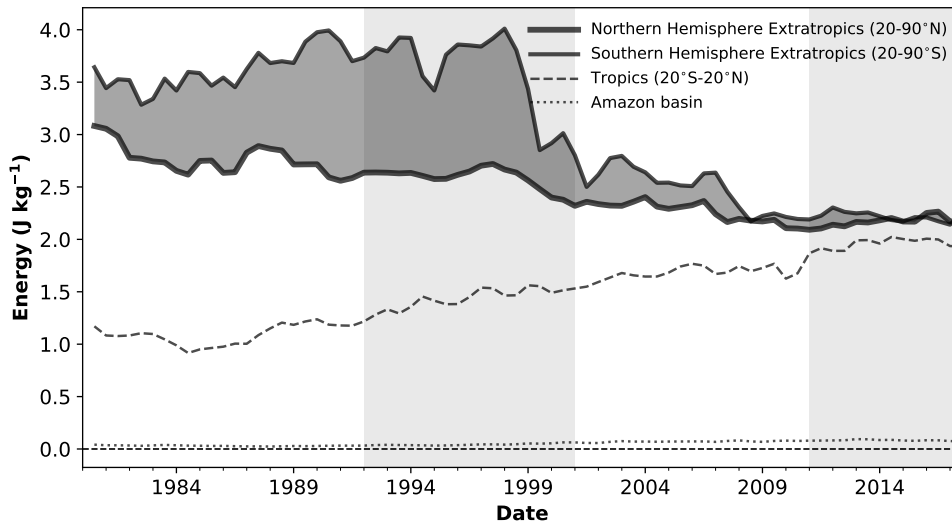
In six-hourly cycling systems, such as those based on 3D-Var, FSOI can be thought

of as a proxy for the error difference between two forecasts valid at the same time but issued six-hours apart¹. These differences are referred to as nonlinear impacts, whereas FSOI is sometimes referred to as a linear impact. In the particular case of calculating FSOI for the 24-hour forecasts, the nonlinear impact is created from differences between the 24- and 30-hour forecast errors; negative numbers meaning that errors in the 24-hour forecast are smaller than those in the 30-hour forecasts, and indicate an improvement in predictions due to the assimilation of new batches of six-hour observations. An illustration of the time evolution of the monthly averaged 24-h forecast errors and linear impacts throughout MERRA-2 are shown in Figures 5.1 and 5.2, respectively. The curves include results for January and July, from 1980 to 2017, and a one-cycle moving average is applied to the monthly means. The total impact is partitioned into four regions (Figure 5.2): Northern Hemisphere Extratropics (NHX), Southern Hemisphere Extratropics (SHX), Tropics, and Amazon basin; the first three appear in Chapter 4 in Figure 4.5 (see page 46). These region definitions are presented in Chapter 3 (see Table 3.2, page 28). Notice the impact of observations in the NHX and SHX reduces quite substantially as MERRA-2 enters the so-called Earth Observing System (EOS), or modern, era (late 1999 onward). The impacts brought about by assimilating observations become much more alike between the two hemispheres in the modern era, as compared to the early pre-EOS period. In the tropics and the Amazon basin, the situation is opposite, with the impact of observations increasing as the reanalysis enters the modern era (a zoom for these two regions appears in Figure 5.3). Results over the Amazon basin are only a small part of those over the whole tropics, but the same trend of increased impact is seen in both regions. In evaluating these results it is essential to realize that, regardless of region, errors constructed from self-verification are bound to underestimate the true errors; self-verified forecast errors are small in the absence of observations. Consequently, under the self-verification there are two reasons for observation impacts to be small (in absolute value): (i) little, and/or poor quality, observations being available; or (ii) many, and/or very high quality, observations being available. There is yet a third possibility related to system errors being so large that no matter what data are assimilated little to no impact is obtained. This is considered a pathetic case of no relevance. In the extra-tropics, the decrease of impact in the modern era is associated with reason (ii): the increase and enhancement in quality of the observations introduced in the late 1990's and beyond, amounts to a consequence improvement in the background fields used in the analyses and

¹Some might prefer to consider the other way around and say that such forecast error differences are a proxy for FSOI. Either way, what follows holds.

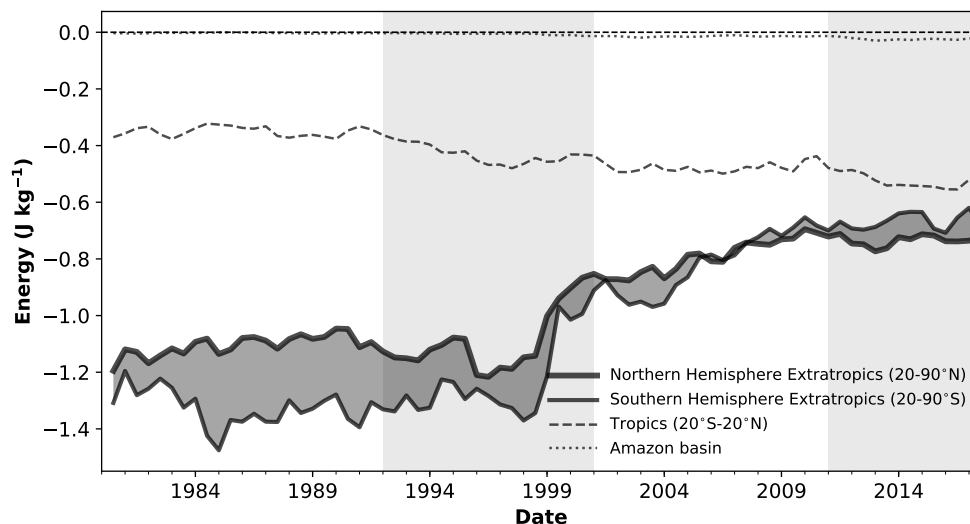
corresponding forecasts. In the tropics, the low impact of observations in the early periods is associated with reason (i). Assuming that as time progresses, MERRA-2 assimilates more and better quality observations in the tropics, the increased forecast errors in this area combined with the steady rise in the observation impacts can be indication of either the observations not being used optimally in this region, or that a certain level of balance between properly observing and predicting the tropics has not yet been achieved in the reanalysis. The precise reasons for the behavior of MERRA-2 observation impacts in the tropics is a topic of investigation beyond the present work.

Figure 5.1 - Time series of 24-h forecast errors in the Northern Hemisphere Extratropics (north of 20°N; thick continuous line), Southern Hemisphere Extratropics (south of 20°S; thin continuous line), Tropics (between 20°S and 20°N; dashed line), and Amazon basin (dotted line). Lines represent monthly mean values during January and July. The shading shows the differences in scores between the two extratropical hemispheres. Values are plotted in the form of annual running means, resulting in that values plotted for January (July) are averages over that month and the preceding July (January), and, as a consequence, we omit values for January 1980 for consistency with the whole time series. The units of energy are J kg^{-1} .



SOURCE: Author's production.

Figure 5.2 - As in Figure 5.1 (page 74), but for linear impacts.



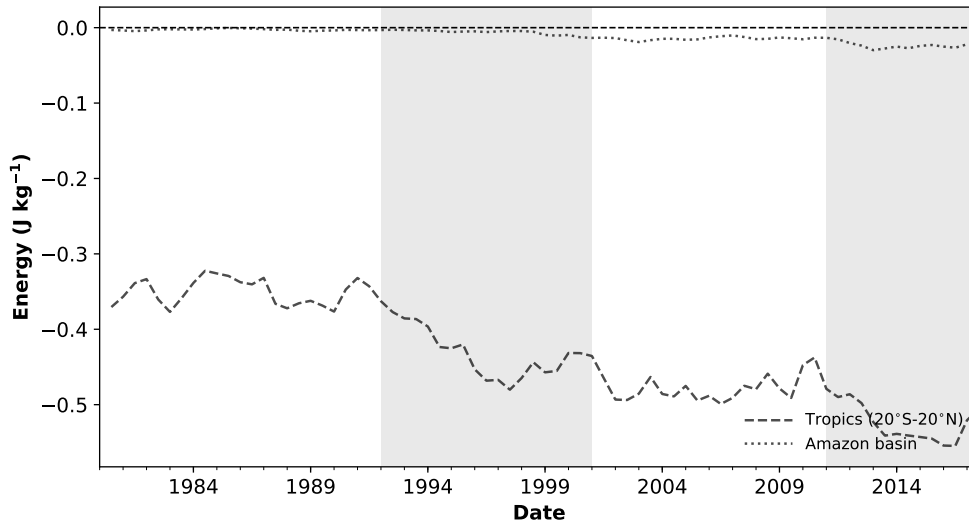
SOURCE: Author's production.

What follows looks more closely at the evolution of impacts seen in Figures 5.2 and 5.3 over the Amazon and determines what changes in the observing system taking place between the pre-EOS and EOS era lead to the noticeable changes of impacts. Specifically, observations will be seen to impact forecasts during wet and dry seasons in different ways, with specific observing systems contributing to the impact in particular ways. Seasonality differences in the impact will be seen to link to corresponding forecast sensitivities. Finally, the observing systems that most contribute to the reduce short-range forecast errors in the region will be identified. The ultimate hope of the present work is to provide an incentive for additional observations to be made available over the Amazon basin as well as to motivate improved treatment of certain observations already assimilated.

5.2 Observing system

The observing system used over nearly 40 years of MERRA-2 analysis is rich and varied and is described in detail in [McCarty et al. \(2016\)](#). It includes conventional observations from a variety of sources, many of which are not available in the Amazon region or are only sparsely available. The bulk of the observations in MERRA-2 is

Figure 5.3 - As in Figure 5.2 (page 75), but only the Tropics (between 20°S and 20°N; dashed line), and the Amazon basin (dotted line).

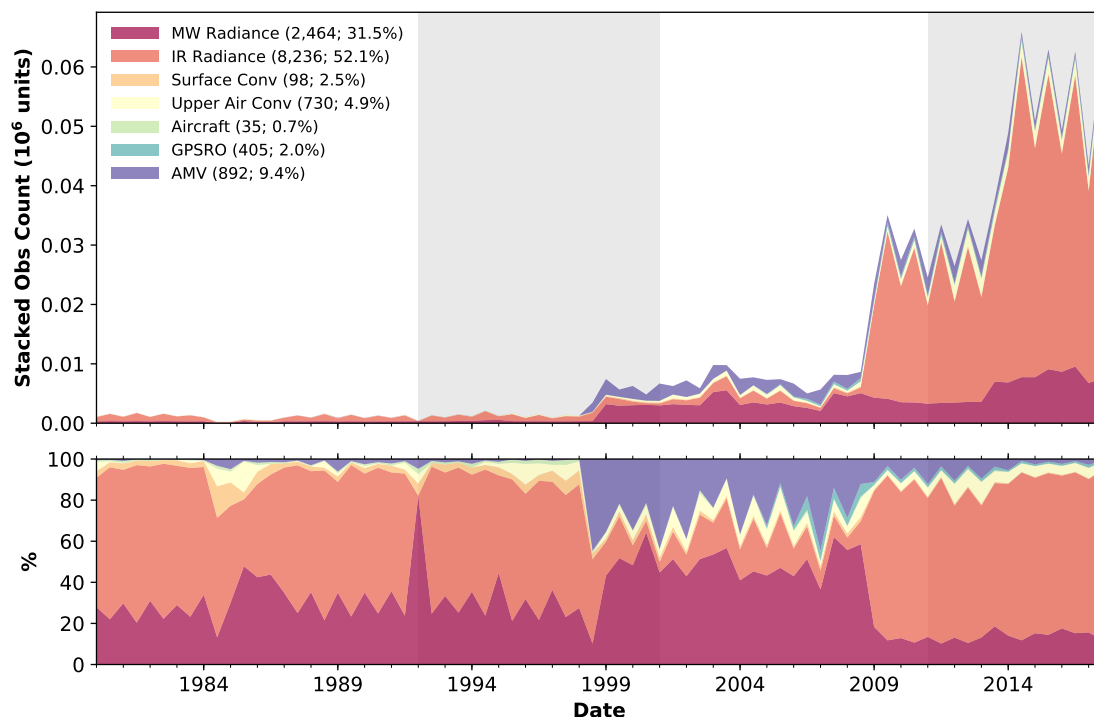


SOURCE: Author's production.

comprised of satellite radiances, especially as the reanalysis enters the EOS era. The modern observing system is dominated by data from hyperspectral instruments such as the Atmospheric Infrared Sounder (AIRS) and Infrared Atmospheric Sounding Interferometer (IASI). Figure 5.4 provides a condensed view of the monthly averaged observation counts (top) and corresponding stacked percentage (bottom) for the various instruments analyzed in MERRA-2, over the Amazon basin. Counts are provided only for the 0000 UTC analyses, and only for January and July since observation impacts are only calculated for these times and months.

From the observation counts in Figure 5.4, we see a dramatic increase in satellite observations in the modern era, as compared to the early pre-EOS era. This increase in observations is a good part of the explanation for the near sudden reduction in observation impact seen in Figures 5.2 and 5.3 in the extratropics (not shown) and the Amazon basin when transitioning from the early to the modern periods. The other reason for the reduced observation impact (not shown here) is the increased quality in certain types of observations [particularly, brightness temperatures derived from microwave (MW) observations; e.g., Microwave Sounding Unit (MSU) versus

Figure 5.4 - Time series of the monthly mean stacked observation count (top) and corresponding fractional count (bottom) for the 0000 UTC MERRA-2 analyses during January and July over the Amazon basin. The scale factor for observation count is 10^6 , and the units for fractional counts are %. Numerical values in the legends are the mean non-scaled number of observations and the mean fractional counts during the availability of each observing system. The vertical shaded and non-shaded areas separate the four streams of MERRA-2.



SOURCE: Author's production.

Advanced Microwave Sounding Unit A (AMSU-A)]. The study in Chapter 4 (and references therein) have shown this to be associated with the considerable reduction in forecast error over the same regions and the same period. Clearly, these are directly related to the reason (ii) listed in the Section 5.1 for how observation impacts can be found to be small.

An illustration of the reason (i) in the Section 5.1 for how small impacts can alternatively be due to near lack of observations is provided by examining the Amazon basin data coverage during the pre-EOS era shown in Figure 5.4. Comparing with Figures 5.2 and 5.3, we see that before the mid-1990's impacts are considerably

low as compared to the impacts in the extratropics. In this early period of the reanalysis, there are not as many observations in the tropics as there are in the extratropics, especially those from conventional observing systems. As observation counts increase into the EOS era, their impact also increases. From the late 1990's to about the end of 2008 there is a considerable increase in coverage from MW instruments (largely AMSU-A) and Atmospheric Motion Vectors (AMVs). During this period, the former makes up about 55% of all data assimilated in the region, while the latter corresponds to about 30% of the data assimilated. From late 2008 and beyond hyperspectral infrared (IR) instruments such as IASI on Meteorological Operational A series (MetOp-A) and eventually on MetOp-B come in the mix and dominate the observation count in the region (see percentage count in the bottom panel of Figure 5.4). All these contribute to an increase in observation impact as compared to the early, sparsely observed, era.

A relevant aspect of the observation count in Figure 5.4 that is especially noticeable during the period between the late 1990's and 2008 is the zig-zagging of the counts of MW, IR, and AMV observations. Close examination reveals it to be a consequence of seasonality, particularly the increase in clouds during the wet (January) months versus the low cloud dry (July) months. The January months tend to have more AMV observations than the July months; it is the presence of clouds, and their movement, that allows for the estimation of AMV observation. Conversely, the GSI 3D-Var analysis of MERRA-2 handles only clear-sky radiances (see Sec. 9 of [Gelaro et al., 2017](#)) consequently resulting in less MW and IR observations in the wet (January) months than in the dry (July) months. Still, the largest variations in count between these instruments come from the presence of multiple water-vapor sensitive channels for IR instruments (especially hyperspectral) — the most water-vapor sensitive channels 1-3 and 15 of AMSU-A (MW) are not assimilated in MERRA-2.

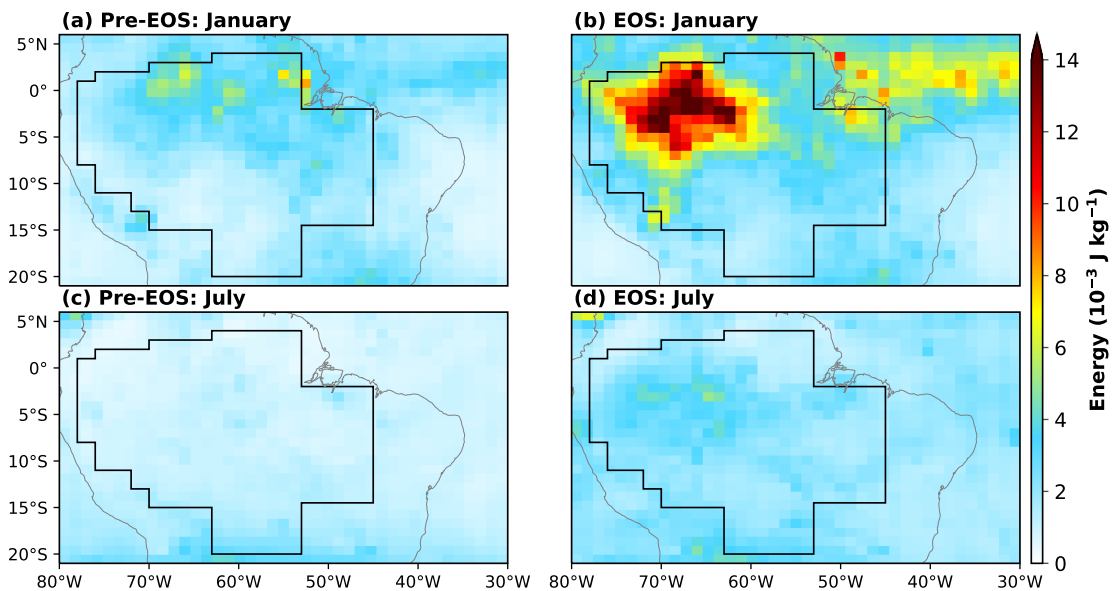
5.3 Forecast sensitivities

A key component associated with the impact of observations on the forecast is the forecast sensitivity derived through (2.3), page 12. A global evaluation of 24-hour vertically integrated energy in forecast sensitivities of MERRA-2 in Chapter 4 has shown the energy fields to be largest along with the storm tracks of each hemisphere and to be more accentuated in the NHX in January with a flipped behavior to the SHX in July. Furthermore, Chapter 4 also find considerable reduction in the 24-hour vertically integrated energy in forecast sensitivities in the EOS era as compared to the pre-EOS era. This reduction is directly associated with the increase in

data volume and the reduced observation impact in the two hemispheres as seen in Figures 5.2 and 5.3.

A similar evaluation comparing 24-hour vertically integrated energy in forecast sensitivities for the pre-EOS and EOS era, but now focused over the Amazon basin is shown here in Figure 5.5. These are 18-year, 1° (roughly 100 km resolution), averaged forecast sensitivities for January and July for each half period of the reanalysis. In opposition to what happens in the extratropics, in the tropics, and in particular over the Amazon basin, the energy in the forecast sensitivities actually increase in magnitude between the two periods. This increase is directly associated with the increased impact of observations in the Tropics and Amazon basin over the same periods and illustrated in Figures 5.2 and 5.3 (pages 75 and 76, respectively). Very noticeable is the contrast between January and July averaged sensitivities, especially during the EOS era.

Figure 5.5 - Eighteen-year averaged 24-hour vertically integrated energy in forecast sensitivities for January [top: (a) and (b)] and July [bottom: (c) and (d)] over the pre-EOS [1982-1999; left: (a) and (c)] and the EOS [2000-2017; right: (b) and (d)] eras. The Amazon basin is represented by polygons in black contour. The scale factor is 10^{-3} and the units of energy are J kg^{-1} .



SOURCE: Author's production.

Partitioning of the averaged energy associated with these sensitivities reveals the dominant parts of the sensitivities to project onto the available potential and latent heat components of the energy (not shown). This is in opposition to what is typically found with the global partitioning of the energy where the largest contribution is determined by the kinetic energy component associated with the winds along the storm tracks. This is not surprising given the relevance of thermodynamical effects in tropical regions.

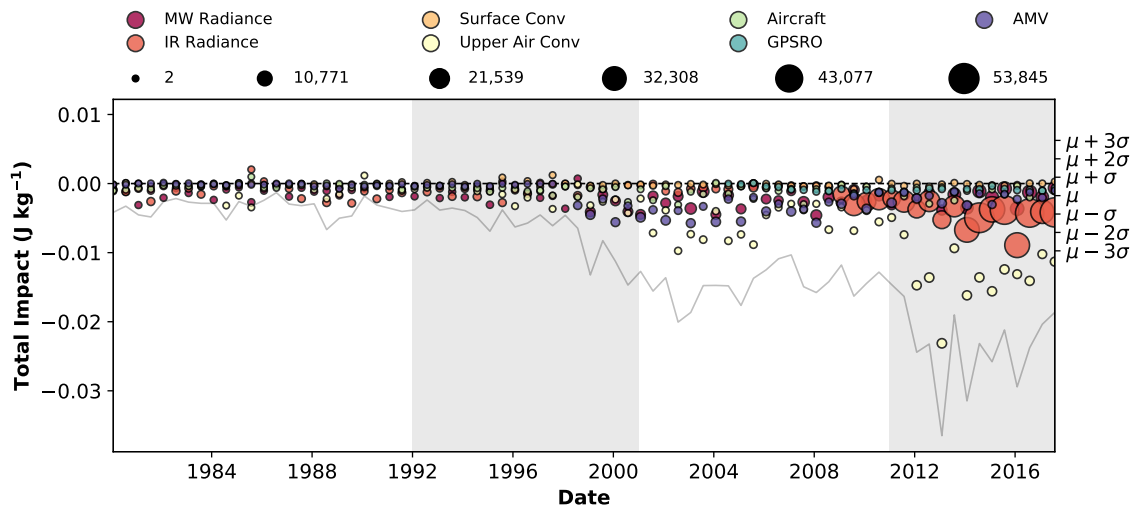
5.4 FSOI results

The impact of each observation on a given forecast can easily be derived from the individual terms of the dot product in the last equality of (2.2), page 12. Clearly, the impact from a single observation makes little sense and what is typically done to obtain meaningful results is to group the individual impacts into various categories and then apply regional and time averages to the grouped impacts. In what follows we largely concentrate on observations (and their corresponding impacts) within the Amazon basin, with considerations of other regions presented only to help reinforce argumentation.

Figures 5.6 and 5.7 provide an overall summary of the observation impact and their fractional impact over the Amazon basin, respectively. As before, results include only January and July, from 1980 to 2017. Each bubble in Figure 5.6 refers to monthly averaged observation impacts, and in Figure 5.7 to fractional impacts for a whole given month. The size of the bubbles in figure reflects the mean observation count over a particular month. The thin solid curve shown in Figure 5.6 is the time series of total observation impact over the Amazon basin and is similar to the dotted curves shown in Figures 5.2 and 5.3, except that a moving average is not applied now. The solid grey curve in Figure 5.7 shows the sum of fractional impact for each month. Except for cases when there are observing systems contributing to deteriorate the forecasts, this grey curve adds up to 100%. The observing system is split into different observation types. With a few exceptions, most of the types contribute to reduce forecast errors, most of the time (negative numbers in Figure 5.6), with some, occasionally contributing in the other direction (positive numbers in Figure 5.6; spikes in the grey curve of Figure 5.7). Note that in relatively confined regions, it is not uncommon, neither a concern to see observations sometimes contributing to deteriorate the forecast; globally, on the other hand, this would require attention.

In the pre-EOS era, the impact of each individual observing type is relatively small, but MW radiance observations (mainly MSU) tend to have a larger impact as com-

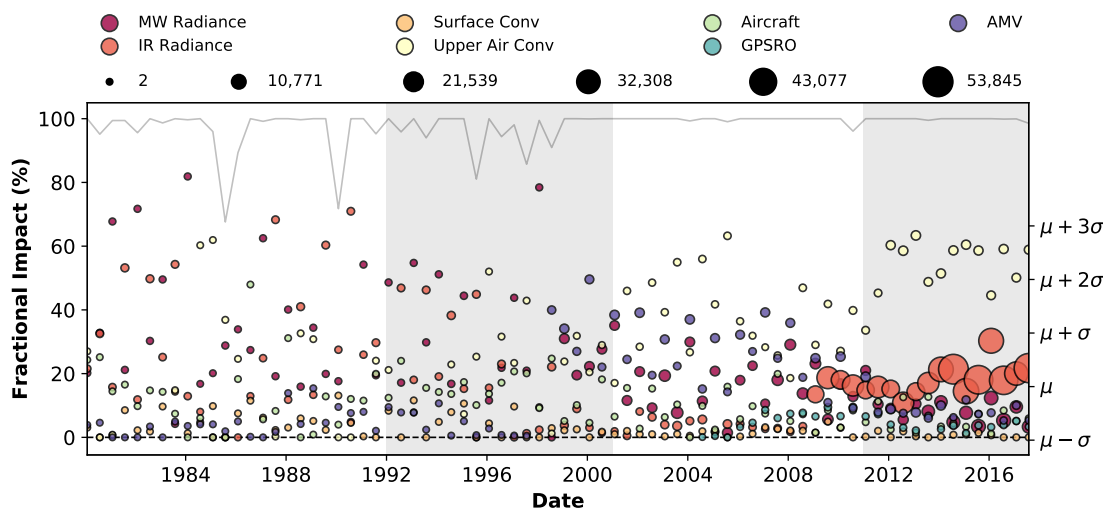
Figure 5.6 - Time series of the monthly mean total impacts for all observations over the Amazon basin, grouped according to classes presented in Figure 5.4 (page 77). The grey line represent the sum of all bubble values for each month and is referred to as the dotted line in Figures 5.2 and 5.3 (pages 75 and 76, respectively), with a single modification related to the moving average that is not being applied here. The size of the bubbles is proportional to the monthly mean observation count for each partition of the observing system. The units of total impact are J kg^{-1} .



SOURCE: Author's production.

pared to other observing types available during that period. As MERRA-2 enters the EOS era considerably more observations become available (as we have seen in Figure 5.4), but now conventional observations seem to dominate the impact. This dominance of conventional observations is especially noticeable in Figure 5.7 when its fractional contribution roves around 55-60%. Observing systems such as AMVs and Aircrafts also provide consistently work to reduce forecast errors, at times contributing to slightly over 20%. Hyperspectral IR observations, once made available, account for as much as 30% of the error reduction. The fractional percentage contribution of GPSRO to error reduction falls a little under 10%. It should be pointed out that the low impact of surface observations, both globally and locally over the Amazon basin, must be taken with some caution. The weights of the total energy norm associated with \mathbf{C} in (2.1) and the modest representation of physical processes in

Figure 5.7 - As in Figure 5.6 (page 81), but for fractional impacts. The grey line represent the sum of all bubble values for each month. The units of fractional impacts are %.



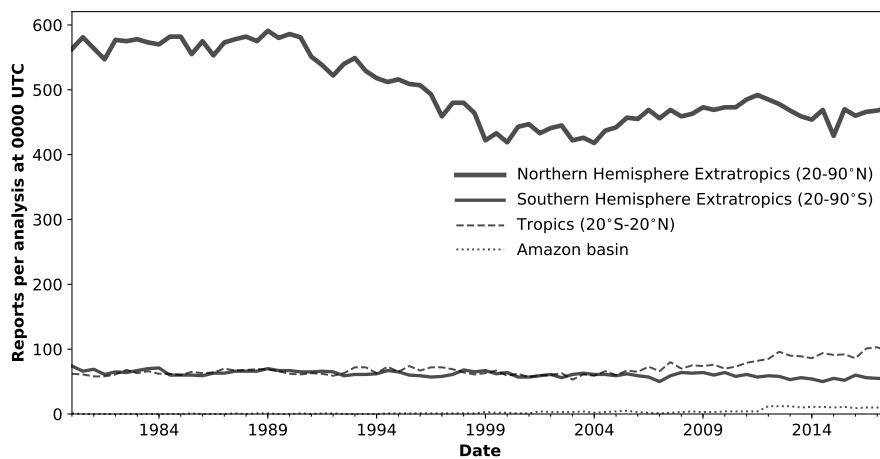
SOURCE: Author's production.

the adjoint model required for the derivation of forecast sensitivities are two factors that can significantly downplay the importance of near-surface observations.

The bulk of what is classified here as conventional observations is dominated by radiosondes. A summary view of the count from radiosonde reports (based on temperature soundings) is shown in Figures 5.8, 5.9 and 5.10. Figure 5.8 gives a broad view of the partitioning of the global network of radiosondes into NHX, SHX, Tropics and over the Amazon basin. Consistent with other works, we find a substantial decrease of this type of observations in the NHX — mainly taking place during the periods between the mid-1990's to the early 2000's — and a mild decrease in the SHX which suffers from considerable lack of radiosondes in comparison to the NHX. A closer view into the Tropics and Amazon basin is provided in Figure 5.9. In the tropics, however, the situation is slightly more positive, with the network experiencing a steady rise in sounding reports from 2004 onward, reaching as much as a 40% rise late in the reanalysis period (e.g., Figure 18 of Dee et al., 2011; and Figure 7 of Gelaro et al., 2017). Over the Amazon basin this is even more favorable (a zoom

for this region appears in Figure 5.10), with a rise in observations also starting in the late 1990's and getting to nearly as many as five times the number of averaged reports. Unfortunately, the total number of averaged reports in the region is so small to begin with that a five-time increase amounts to still a small count overall. But even just a few extra radiosonde reports seem to contribute remarkably, steadily, and consistently to a progressive reduction in forecast errors — see latter part of time series in Figure 5.6.

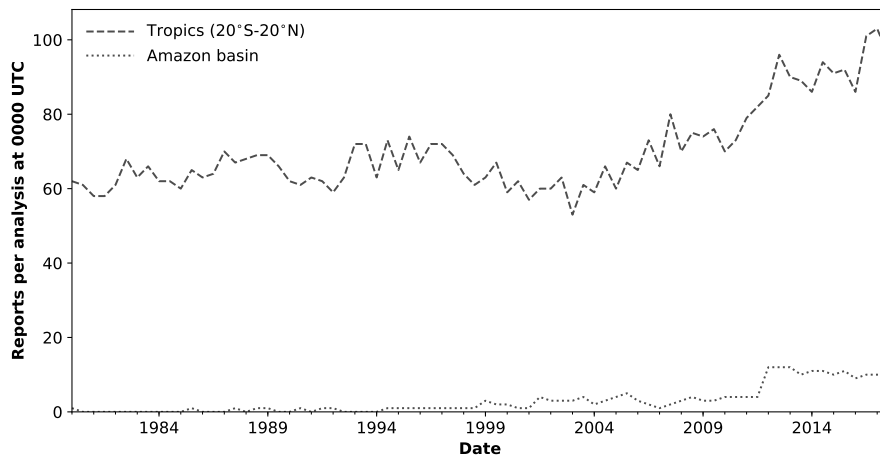
Figure 5.8 - Time series of the monthly mean number of radiosonde reports per analysis at 0000 UTC in the Northern Hemisphere Extratropics (north of 20°N; thick continuous line), Southern Hemisphere Extratropics (south of 20°S; thin continuous line), Tropics (between 20°S and 20°N; dashed line), and Amazon basin (dotted line). Lines represent monthly mean values during January and July. Only reports including temperature are account for.



SOURCE: Author's production.

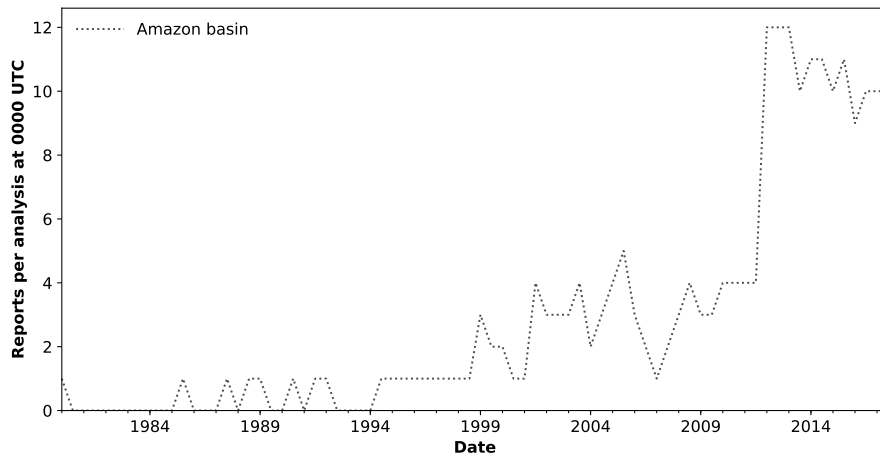
It is rather peculiar that in the midst of the data-rich EOS period, highly dominated by satellite observations, one finds a handful of conventional observations to dominate the fractional impact. It is possible that the somewhat concurrent introduction of hyperspectral instruments helps improve the use of other data types through an improvement in the underlying background fields. It is also conceivable that assimilation of all-sky MW and hyperspectral IR instruments might take over and get these instruments to become the dominant contributors to forecast error reduction in the Amazon basin. All-sky assimilation, however, is not part of MERRA-2. Work is being done in the GSI analysis to treat observations in cloudy and precipitating

Figure 5.9 - As in Figure 5.8 (page 83), but only the Tropics (between 20°S and 20°N; dashed line) and the Amazon basin (dotted line).



SOURCE: Author's production.

Figure 5.10 - As in Figure 5.8 (page 83), but only the Amazon basin.



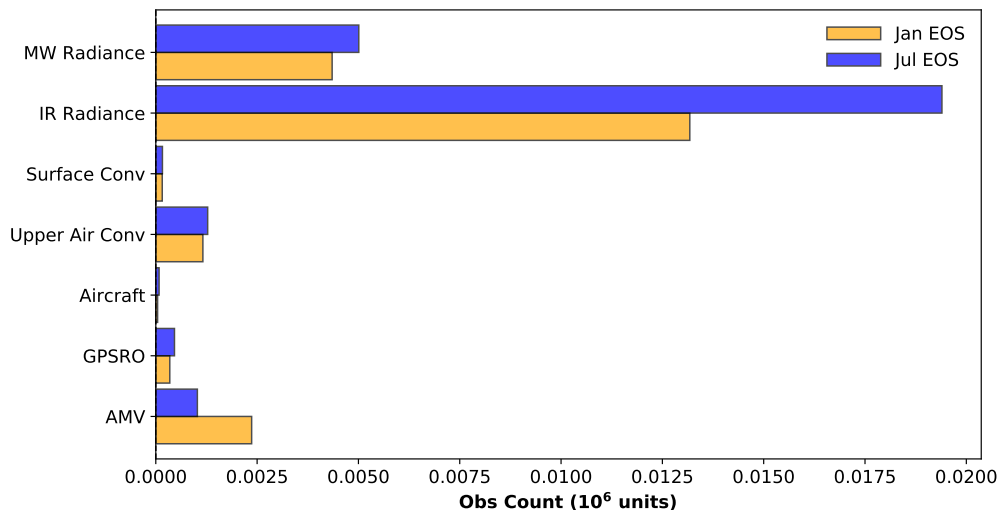
SOURCE: Author's production.

conditions, as it is already the case for how some instruments and channels used in other assimilation systems are treated (see Bauer et al., 2011; Geer et al., 2018).

5.5 Seasonal effect on FSOI

The effectiveness of different components of the observing system and their relationship with corresponding impacts is, in some cases, driven by seasonal effects. This was noticed earlier when examining the zig-zagging pattern in some of the types of observations shown in Figure 5.4 (page 77), and when examining the behavior of MERRA-2 24-hour forecast energy in the fields of sensitivities over the Amazon basin in Figure 5.5 (page 79).

Figure 5.11 - Barplot of monthly mean observation counts for January (orange) and July (blue) during the EOS era (2000-2017). The scale factor for observation count is 10^6 .



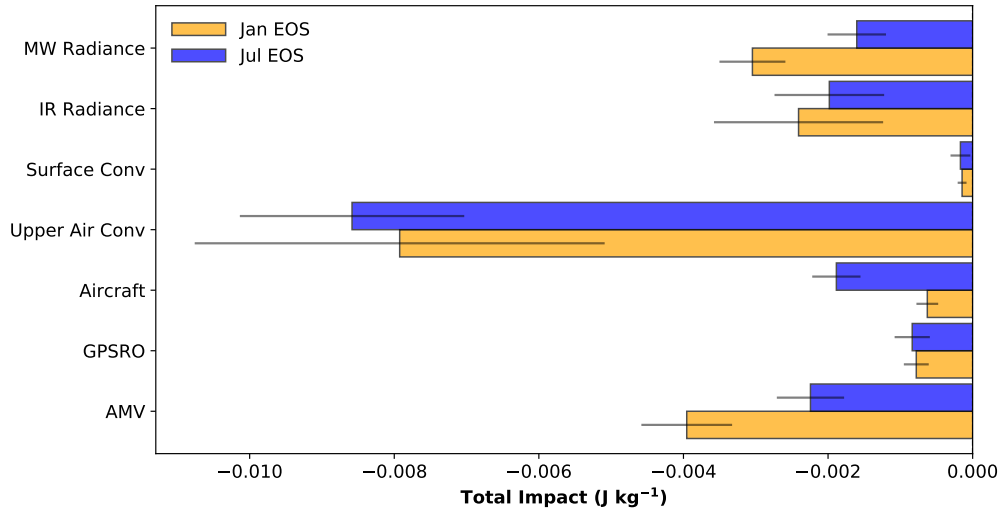
SOURCE: Author's production.

A more specific illustration of the seasonality effect in the observing system is shown in Figures 5.11 and 5.12. Here, observation counts and corresponding total impacts for the 18 years of January and July months over the EOS era are shown in Figures 5.11 and 5.12, respectively, for the Amazon basin. These two periods are the same as considered in panels (b) and (d) of Figure 5.5 (see page 79) when examining the vertically integrated energy in forecast sensitivities in the EOS era. Not all observation types displayed in the bar plots of the present figure are available for the whole of the 18 years; the averaging procedure is calculated according to the availability of the observing types. We notice from the *counts* that the wet Jan-

uary months end up with more AMV observations than the corresponding dry July months. Conversely, wet periods show lower (clear sky) MW and IR counts than dry periods. GPSRO also shows a small seasonal variability. The observation counts of other instruments remain mostly consistent irrespective of the season. Accordingly, Figure 5.12 shows that the *impact* of AMV is larger in the wet periods than in the dry periods, whereas the opposite is true for the *impact* of Upper-Air Conv observations. Although fewer MW observations participate in the wet periods, their *impact* is largest in such periods. Very few aircraft observations are available in either period, but surprisingly their impact is comparable to the impact of other instruments when summed over the whole EOS period. This is perhaps a statement about the importance of such observations. Overall, the relationship of impacts among different instruments here are in agreement with the tropical results of Gelaro and Zhu (2009, their Figures 3 and 4) obtained when comparing FSOI with the alternative approach of observation-system-experiment for two *specific* months of January and July. The whiskers in the bars of Figure 5.12 correspond to the standard error of the mean with 95% confidence intervals calculated using the standard deviation from the averaged spatial variances of the impacts for each January and July months, for each observation category. These show essentially the uncertainty of the monthly mean impacts during the EOS era, and also provides an idea about the variability of this mean. Looking at Figure 5.7 we can infer similar information, with most categories showing relatively small time variability in their impacts with the exception of Upper-Air conventional observations. This latter case is seen to have considerable increase in fractional impact toward the more recent years of the reanalysis, with correspondingly large standard deviations indicated in Figure 5.12.

As mentioned above, Figures 5.11 and 5.12 indicate that GPSRO (bending angle) is another observing system with sensitivity to seasonality. The wet periods have reduced counts and smaller impacts than the dry periods. A closer look at GPSRO appears in Figures 5.13 and 5.14, where the averaged results for January and July are shown in the form of profiles for scaled OmB residual mean (solid curves), standard deviations of the OmB (dashed curves), and corresponding observation impact (bars) and associated standard error of the mean impacts with 95% confidence intervals (whiskers). The scaled means and standard deviations of the OmB residuals are only mildly affected by seasonality, but a more considerable difference is noticed in the observation impacts themselves. In the dry season, the largest impacts from GPSRO occur in the layer between 10-25 km; in the wet season, the largest impacts are confined to a smaller layer between 13-20 km. The former is mainly in agreement with the findings of Cardinali and Healy (2014) on a study done over June 2011

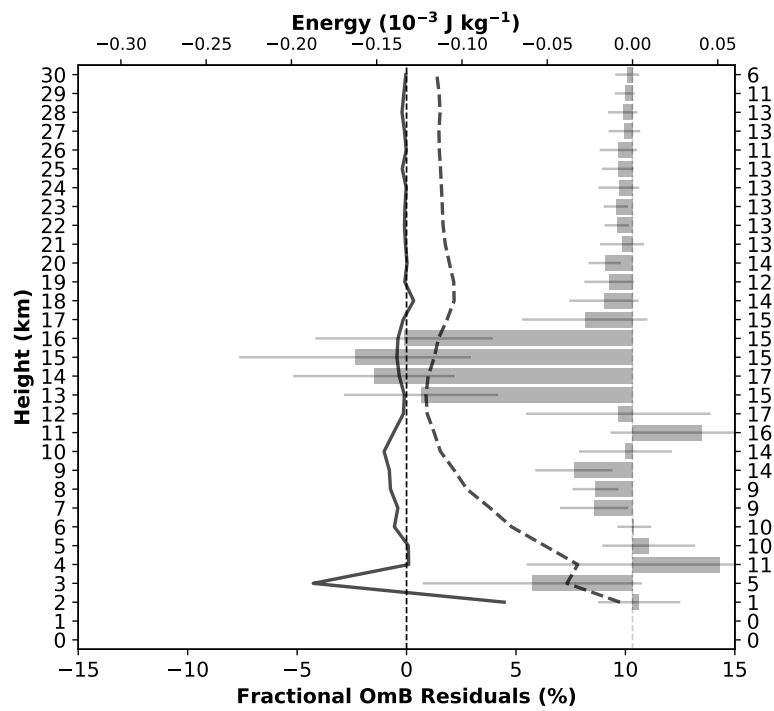
Figure 5.12 - As in Figure 5.11 (page 85), but for total impact. The units of total impact are J kg^{-1} .



SOURCE: Author's production.

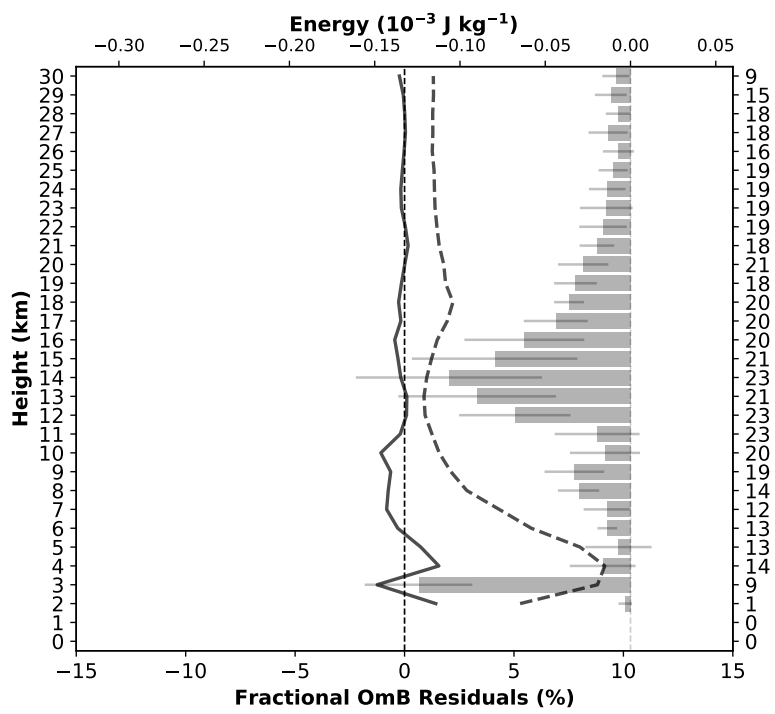
(i.e., dry season). The more sensitive January forecasts sensitivities (Figure 5.5b) affect the tropospheric contribution (up to 13 km) of GPSRO in the wet season, with a large part of the profile showing a deterioration of forecast error reduction (positive impacts), especially in the lower portion of the atmosphere. This reduced effectiveness of GPSRO in wet periods is attributed to the GSI bending angle forward observation operator large sensitivities (reflected in the Jacobian operator) to moisture in the environment (CUCURULL *et al.*, 2013). Cucurull *et al.* (2013) suggest that the incorporation of horizontal gradients of refractivity (mainly caused by water vapor) in the current GPSRO forward operator used in GSI is expected to improve the use of such observations, particularly in the lower troposphere.

Figure 5.13 - Vertical profile of mean (continuous line, bottom axis) and standard deviation (dashed line, bottom axis) of fractional observation-minus-background (OmB) residuals, and total impact (bars, top axis) for GPSRO observations over the Amazon basin. Values represent 13-year average, from 2005 to 2017, during January. The whiskers correspond to the standard error of the mean with 95% confidence intervals calculated using the standard deviation as in Figure 5.12. The column on the right represents mean number of observations per analysis in each layer. The units of mean and standard deviation of fractional OmB residuals are % and of total impact and their standard errors are 10^{-3}J kg^{-1} .



SOURCE: Author's production.

Figure 5.14 - As in Figure 5.13 (page 88), but for July.



SOURCE: Author's production.

6 SUMMARY AND CONCLUSIONS

In this chapter, all of the results and findings of this thesis are summarised. Additionally, some ideas for further work are outlined at the end of the chapter.

The main objective of this thesis was understand the impact of observations on short-range forecasts in the broader context of yearly to decadal time scales of reanalysis. The present study applied the Forecast Sensitivity Observation Impact (FSOI) technique to a multi-year reanalysis. Thus far, FSOI studies have been conducted largely in the context of short month-long experiments. Routine monitoring of FSOI presently carried out by many operational or quasi-operational data assimilation (DA) institutions reflect not only changes in the observing system but also changes in the underlying sub-components of the DA systems which get frequent upgrades with the latest system improvements. Reanalyses provide a convenient framework for FSOI studies given that these only incur changes associated with the observing system.

The GMAO MERRA-2 contains all the ingredients necessary for obtaining FSOI estimates. The approach in this work follows the Trémolet (2008) extension of Langland and Baker (2004) and uses the available adjoint of the MERRA-2 general circulation model and the adjoint of its corresponding 3D-Var. Short-range (24-hour) forecasts required for FSOI, and obtained from the MERRA-2 analyses considered for this study, provide valuable insight for how new observations contribute to such forecasts. As a corroboration of forecasts results from other reanalysis, the MERRA-2 forecasts shows a steady rise in familiar anomaly correlation diagnostics starting from its early days all the way up to present day. Not seen in such single-level, single-variable forecast error diagnostic, but detected in the multi-variate forecast error evaluation required for FSOI in the present work is the sharp improvement in forecast errors when transitioning from the late 1990's to the early 2000's. This improvement is also noticed in the total observation impact obtained from FSOI. Surprisingly, global forecast errors seem to rise somewhat from the mid-1980's to the end of the 1990's. Closer examination reveals the rise to be due to error growth in the Southern Hemisphere. Furthermore, from the mid-1980's until around 2010, errors in the Tropics steadily grow until stabilizing in the more recent years. Though some explanation relates to the sparseness of the observing system in these regions in the early periods of the reanalysis, and on the self-verification nature of the error definition, an ongoing investigation is taking place to better understand the error behavior. Since the forecast error metric employed in the present work has not been

applied to forecast from other reanalyses, no means of corroborating these results is presently available.

Although the study here considers only the months of January and July from 1980 to 2017, and only the 0000 UTC analyses, the results satisfactorily illustrate the contributions from various observing system components in reducing forecast errors along the reanalysis period. In its early days, “Conventional” observations, made up of radiosondes, aircraft, satellite wind retrievals, and a few others, amount to nearly 45% of the total number of available observations and the observation impacts were largely dominated by these instruments, followed by satellite radiances from the Microwave Sounding Unit (MSU) and High-resolution Infrared Radiation Sounder (HIRS) instruments.

As the reanalysis switches from the TIROS-N Operational Vertical Sounder (TOVS) to the Advanced TOVS period, and even more so, from the so-called pre-Earth Observing System (EOS) period into the modern EOS era, the percentage of conventional observations steadily decreases as newer satellite instruments with increased number of channels get in the mix and eventually, with the advent of the hyper-spectral infrared (IR) instruments, satellite radiances completely dominate the data count, bringing the percentage of Conventional observations down into the single digits. Still, the impact of Conventional observations remains among the strongest, being superseded only by the contribution from microwave observations, largely the Advanced Microwave Sounding Unit-A (AMSU-A) instruments, and even so, not by much.

Among the radiance instruments, MSU is found to dominate the impacts during the pre-EOS era, whereas AMSU-A replaces its dominance in the late 1990s and into the EOS era. The HIRS instrument in the pre-NOAA-15 satellites is second to MSU during the pre-EOS era with the impacts of these instruments becoming less significant when hyperspectral IR observations of the Atmospheric Infrared Sounder (AIRS) and eventually the Infrared Atmospheric Sounding Interferometer (IASI) become available. Interestingly, the fractional impact of the hyperspectral instruments remain at about the same levels as the fractional impact of the HIRS instruments. This is attributed to the MERRA-2 analysis giving more weight to the HIRS instruments than to their hyperspectral counterpart; these latter are not being used to better potential given that inter-channel correlations are not accounted for in the analysis of MERRA-2. Much of the impact of satellite radiances is shown to be consistent with the weight given by the underlying MERRA-2 3D-Var analysis to

these observations. That is, mostly, radiance observations given large weights by the 3D-Var procedure tend to have larger fractional impacts. Some exceptions to this are encountered at major instrument transitional periods. During the data rich EOS period, a small decrease in the fractional impact from brightness temperature is found to be explained by a compensating increase due to an increase in the availability of aircraft wind and AMV observations and the introduction of GPSRO.

As a follow up to the work of Chapter 4, we examined the impact of observations in short-range forecasts from the MERRA-2 reanalysis over the Amazon basin in Chapter 5. The study in this chapter also employs the FSOI technique of [Langland and Baker \(2004\)](#), combined with the [Trémolet \(2008\)](#) correction to account for multiple linearizations of the observation operator, to assess the impact of nearly 40 years of assimilation of observations, but over this challenging region of the globe. In some respects, results in this region are found to be not much different from those obtained from the global picture. But its specificity serves as a reminder and motivation for the need to improve upon the usage of certain observation types with much potential over the Amazon in particular, and in the tropics in general

It is especially clear from this work that, even with the advent of a dramatic increase in satellite observations over the past 20 years, 3D-Var reanalysis such as MERRA-2 reveals the importance and heavy reliance on conventional observations. Over the Amazon basin, in particular, the present work shows the dominance of only a minimal set of radiosondes in these same 20 years. The mild increase in the number of radiosonde reports over the basin after 2012 is seen to get the network to contribute to over 50% of the impact in reducing forecast errors as compared to the contribution from all other observations in the region. The relevance of radiosondes in the region has been emphasized in many works, some of which suggest approaches to improve upon the network. Among these, there are innovative ideas to help enhance the availability of such observations on a routine basis, especially over remote regions such as the Amazon basin (e.g., glidersondes of [Lafon et al., 2014](#)).

At the same time, it can be fairly argued that more advanced techniques to take advantage of radiance observations in cloudy and precipitating regions might mitigate the apparent need for an increase in radiosonde-like observations. The relatively low impact of radiance observations in the Amazon basin found in the present MERRA-2-based evaluation is likely different in a system that already treats some of the radiance observations as all-sky. Indeed, *global* results show that radiance observations dominate the overall impact when some are treated as all-sky (see [Cardinali](#)

and Prates, 2011). The potential improvement on the usage of satellite radiance through techniques allowing for all-sky conditions is also expected to affect the interplay found in this work between the clear-sky radiance of MERRA-2 and Atmospheric Motion Vectors (AMVs). The presence of clouds and precipitation in the wet Amazon season should no longer be a reason to find the impact from radiance to be smaller than the impact from AMVs.

From its introduction in the early 2000's, the Global Positioning System Radio Occultation (GPSRO) observations are found to contribute to about 10% to the overall reduction in forecast errors on a global scale. Over the Amazon basin, its contribution is slightly less than 10%, but it is seen to vary somewhat with season. The assimilation of bending angle in the MERRA-2 analysis seems quite sensitive to low and mid-tropospheric water vapor, which in turn contributes to reduce the effectiveness of these observations in wet periods. There is potentially room for improvement in the GPSRO forward operator as implemented in the Gridpoint Statistical Interpolation analysis when it comes to handling sensitivity to water vapor.

All of the results and conclusions drawn in this study are dependent on the metric chosen to evaluate errors in the forecast. As it turns out, the metric in this study essentially focus on the troposphere, giving very little weight to the stratosphere and near surface regions. Also related to the metric is that results in the present work are based on self-verification. A viable extension of this work that chooses an alternative verification would likely inform us on the subtle differences between two different systems. Choosing operational analyses for verification might not be desirable for reanalysis studies since the former have the signature of changes beyond those related to the observing system only. Choosing to verify against a reanalysis other than MERRA-2 might be worth pursuing.

A continuation of this study plans to compare some of the results here with other measures of observation impact, such as, for example, the degrees of freedom for signal (DFS; Lupu et al., 2011; Horányi, 2017). Different methods based on the inverse observation error covariance (e.g., Todling, 2013) can still use FSOI but provide an alternative view of the impact of observations in DA systems. Some additional ideas for the next steps of the present study are already taking place, which includes:

- Further study under the metrics used here considering the effect of the

stratosphere in the Tropics (mainly over convectively active areas), as well as the interaction between Tropics and Extratropics;

- A closer look into single-month specific results comparing with studies available over the literature, and also evaluate the possibility to add our results with those being obtained in the Joint Center for Satellite Data Assimilation (JCSDA) FSOI Intercomparison effort;
- And, investigate the applicability of an augmented version of the total energy accommodating coefficients for additional terms not contemplated by the traditional version (e.g., ozone, precipitation, clouds, bias correction coefficients).

REFERENCES

- ANDERSSON, E.; HASELER, J.; UNDÉN, P.; COURTIER, P.; KELLY, G.; VASILJEVIC, D.; BRANKOVIC, C.; GAFFARD, C.; HOLLINGSWORTH, A.; JAKOB, C.; JANSSEN, P.; KLINKER, E.; LANZINGER, A.; MILLER, M.; RABIER, F.; SIMMONS, A.; STRAUSS, B.; VITERBO, P.; CARDINALI, C.; THÉPAUT, J.-N. The ECMWF implementation of three-dimensional variational assimilation (3D-Var). III: experimental results. **Quarterly Journal of the Royal Meteorological Society**, v. 124, n. 550, p. 1831–1860, 1998. Available from: <<https://rmets.onlinelibrary.wiley.com/doi/abs/10.1002/qj.49712455004>>. 2
- ANDERSSON, E.; SATO, B. Y. **Fifth WMO workshop on the impact of various observing systems on numerical weather prediction**. World Meteorological Organization, Geneva, Switzerland, 2012. v. 5, 25 p. Available from: <www.wmo.int/pages/prog/www/OSY/Reports/NWP-5_Sedona2012.html>. 9
- ATLAS, R. Atmospheric observations and experiments to assess their usefulness in data assimilation. **Journal of Meteorological Society of Japan**, v. 75, n. 1B, p. 111–130, 1997. 10
- AULIGNE, T.; GELARO, R.; MAHAJAN, R.; HOLDAWAY, D.; MCCARTY, W.; COLLARD, A.; BAKER, N.; LANGLAND, R.; HOTTA, D.; ISHIBASHI, T.; EYRE, J.; TENNANT, W.; GROFF, D. Forecast sensitivity observation impact (FSOI) inter-comparison experiment. In: AMS SYMPOSIUM ON THE JOINT CENTER FOR SATELLITE DATA ASSIMILATION AT THE 97TH AMERICAN METEOROLOGICAL SOCIETY ANNUAL MEETING, 97., 2017, Seattle, Washington. **Proceedings...** Washington State Convention Center, Seattle, Washington, 2017. 19
- BAKER, N. L.; DALEY, R. Observation and background adjoint sensitivity in the adaptive observation-targeting problem. **Quarterly Journal of the Royal Meteorological Society**, v. 126, n. 565, p. 1431–1454, 2000. Available from: <<http://dx.doi.org/10.1002/qj.49712656511>>. 11, 18
- BAUER, P.; AULIGNÉ, T.; BELL, W.; GEER, A.; GUIDARD, V.; HEILLIETTE, S.; KAZUMORI, M.; KIM, M.-J.; LIU, E. H.-C.; MCNALLY, A. P.; MACPHERSON, B.; OKAMOTO, K.; RENSHAW, R.; RIISHØJGAARD, L.-P. Satellite cloud and precipitation assimilation at operational NWP centres. **Quarterly Journal of the Royal Meteorological Society**, v. 137, n. 661, p.

1934–1951, 2011. Available from:

<<https://rmets.onlinelibrary.wiley.com/doi/abs/10.1002/qj.905>>. 84

BAUER, P.; THORPE, A.; BRUNET, G. The quiet revolution of numerical weather prediction. **Nature**, v. 525, n. 7567, p. 47–55, 2015. Available from:

<<http://dx.doi.org/10.1038/nature14956>>. 1

BLOOM, S. C.; TAKACS, L. L.; DA SILVA, A. M.; LEDVINA, D. Data assimilation using incremental analysis updates. **Monthly Weather Review**, v. 124, n. 6, p. 1256–1271, 1996. Available from:

<[https://doi.org/10.1175/1520-0493\(1996\)124<1256:DAUIAU>2.0.CO;2](https://doi.org/10.1175/1520-0493(1996)124<1256:DAUIAU>2.0.CO;2)>. 25, 37

BOSILOVICH, M. G.; ROBERTSON, F. R.; TAKACS, L.; MOLOD, A.; MOCKO, D. Atmospheric water balance and variability in the MERRA-2 reanalysis. **Journal of Climate**, v. 30, n. 4, p. 1177–1196, 2017. Available from:

<<https://doi.org/10.1175/JCLI-D-16-0338.1>>. 22

BÖTTGER, H.; P., M.; PAILLEUX, J. **Third WMO workshop on the impact of various observing systems on numerical weather prediction**. World Meteorological Organization, Geneva, Switzerland, 2004. v. 3, 324 p. Available from: <www.wmo.int/pages/prog/www/documents.html>. 9

BOULLOT, N.; RABIER, F.; LANGLAND, R.; GELARO, R.; CARDINALI, C.; GUIDARD, V.; BAUER, P.; DOERENBECHER, A. Observation impact over the southern polar area during the Concordiasi field campaign. **Quarterly Journal of the Royal Meteorological Society**, v. 142, n. 695, p. 597–610, 2016. ISSN 1477-870X. Available from: <<http://dx.doi.org/10.1002/qj.2470>>. 19, 72

BUCHARD, V.; DA SILVA, A. M.; COLARCO, P. R.; DARMENOV, A.; RANGLES, C. A.; GOVINDARAJU, R.; TORRES, O.; CAMPBELL, J.; SPURR, R. Using the OMI aerosol index and absorption aerosol optical depth to evaluate the NASA MERRA aerosol reanalysis. **Atmospheric Chemistry and Physics**, v. 15, n. 10, p. 5743–5760, 2015. Available from:

<<https://www.atmos-chem-phys.net/15/5743/2015/>>. 22

BUCHARD, V.; RANGLES, C. A.; DA SILVA, A. M.; DARMENOV, A.; COLARCO, P. R.; GOVINDARAJU, R.; FERRARE, R.; HAIR, J.; BEYERSDORF, A. J.; ZIEMBA, L. D.; YU, H. The merra-2 aerosol reanalysis, 1980 onward. part ii: Evaluation and case studies. **Journal of Climate**, v. 30,

n. 17, p. 6851–6872, 2017. Available from:

<<https://doi.org/10.1175/JCLI-D-16-0613.1>>. 22

BUEHNER, M.; DU, P.; BÉDARD, J. A new approach for estimating the observation impact in ensemble–variational data assimilation. **Monthly Weather Review**, v. 146, n. 2, p. 447–465, 2018. Available from:

<<https://doi.org/10.1175/MWR-D-17-0252.1>>. 11, 18, 71

CARDINALI, C. **Forecast sensitivity to observation (FSO) as a diagnostic tool**. Berkshire, England: European Centre for Medium Range Weather Forecasts Shinfield Park, 2009. 26 p. Available from:

<<https://www.ecmwf.int/node/8574>>. 5, 71

_____. Monitoring the observation impact on the short-range forecast. **Quarterly Journal of the Royal Meteorological Society**, v. 135, n. 638, p. 239–250, 2009. Available from: <<http://dx.doi.org/10.1002/qj.366>>. 5, 10

_____. Forecast sensitivity observation impact with an observation-only based objective function. **Quarterly Journal of the Royal Meteorological Society**, v. 144, n. 716, p. 2089–2098, 2018. Available from:

<<https://doi.org/10.1002/qj.3305>>. 72

CARDINALI, C.; HEALY, S. Impact of GPS radio occultation measurements in the ECMWF system using adjoint-based diagnostics. **Quarterly Journal of the Royal Meteorological Society**, v. 140, n. 684, p. 2315–2320, 2014. ISSN 1477-870X. Available from: <<http://dx.doi.org/10.1002/qj.2300>>. 5, 11, 68, 69, 86

CARDINALI, C.; PRATES, F. Performance measurement with advanced diagnostic tools of all-sky microwave imager radiances in 4D-Var. **Quarterly Journal of the Royal Meteorological Society**, v. 137, n. 661, p. 2038–2046, 2011. Available from:

<<https://rmets.onlinelibrary.wiley.com/doi/abs/10.1002/qj.865>>. 5, 69, 94

CHEN, Y.; WENG, F.; HAN, Y.; LIU, Q. Validation of the community radiative transfer model by using CloudSat data. **Journal of Geophysical Research**, v. 113, n. D8, 2008. Available from:

<<https://doi.org/10.1029/2007JD009561>>. 23

CHIN, M.; GINOUX, P.; KINNE, S.; TORRES, O.; HOLBEN, B. N.; DUNCAN, B. N.; MARTIN, R. V.; LOGAN, J. A.; HIGURASHI, A.; NAKAJIMA, T.

Tropospheric aerosol optical thickness from the GOCART model and comparisons with satellite and sun photometer measurements. **Journal of the Atmospheric Sciences**, v. 59, n. 3, p. 461–483, 2002. Available from:

<[https://doi.org/10.1175/1520-0469\(2002\)059<0461:TAOTFT>2.0.CO;2](https://doi.org/10.1175/1520-0469(2002)059<0461:TAOTFT>2.0.CO;2)>.

22

COLARCO, P.; DA SILVA, A.; CHIN, M.; DIEHL, T. Online simulations of global aerosol distributions in the NASA GEOS-4 model and comparisons to satellite and ground-based aerosol optical depth. **Journal of Geophysical Research - Atmospheres**, v. 115, n. D14, 2010. Available from: <<https://agupubs.onlinelibrary.wiley.com/doi/abs/10.1029/2009JD012820>>.

22

<<https://agupubs.onlinelibrary.wiley.com/doi/abs/10.1029/2009JD012820>>.

COURTIER, P.; ANDERSSON, E.; HECKLEY, W.; VASILJEVIC, D.; HAMRUD, M.; HOLLINGSWORTH, A.; RABIER, F.; FISHER, M.; PAILLEUX, J. The ECMWF implementation of three-dimensional variational assimilation (3D-Var). I: formulation. **Quarterly Journal of the Royal Meteorological Society**, v. 124, n. 550, p. 1783–1807, 1998. Available from: <<https://rmets.onlinelibrary.wiley.com/doi/abs/10.1002/qj.49712455002>>.

2

<<https://rmets.onlinelibrary.wiley.com/doi/abs/10.1002/qj.49712455002>>.

CUCURULL, L.; DERBER, J. C. Operational implementation of COSMIC observations into NCEP's global data assimilation system. **Weather and Forecasting**, v. 23, n. 4, p. 702–711, 2008. Available from:

<<https://doi.org/10.1175/2008WAF2007070.1>>. 66

CUCURULL, L.; DERBER, J. C.; PURSER, R. J. A bending angle forward operator for global positioning system radio occultation measurements. **Journal of Geophysical Research - Atmospheres**, v. 118, n. 1, p. 14–28, 2013. ISSN 2169-8996. Available from: <<http://dx.doi.org/10.1029/2012JD017782>>.

87

<<http://dx.doi.org/10.1029/2012JD017782>>.

CULLATHER, R. I.; NOWICKI, S. M. J.; ZHAO, B.; SUAREZ, M. J. Evaluation of the surface representation of the Greenland ice sheet in a general circulation model. **Journal of Climate**, v. 27, n. 13, p. 4835–4856, 2014. Available from:

<<https://doi.org/10.1175/JCLI-D-13-00635.1>>. 23

DAESCU, D. N. On the sensitivity equations of four-dimensional variational (4D-Var) data assimilation. **Monthly Weather Review**, v. 136, n. 8, p. 3050–3065, 2008. Available from:

<<http://dx.doi.org/10.1175/2007MWR2382.1>>. 11

_____. On the deterministic observation impact guidance: a geometrical perspective. **Monthly Weather Review**, v. 137, n. 10, p. 3567–3574, 2009. Available from: <<http://dx.doi.org/10.1175/2009MWR2954.1>>. 10

DAESCU, D. N.; LANGLAND, R. H. Error covariance sensitivity and impact estimation with adjoint 4d-var: theoretical aspects and first applications to navdas-ar. **Quarterly Journal of the Royal Meteorological Society**, v. 139, n. 670, p. 226–241, 2013. ISSN 1477-870X. Available from: <<http://dx.doi.org/10.1002/qj.1943>>. 11

DAESCU, D. N.; TODLING, R. Adjoint estimation of the variation in model functional output due to the assimilation of data. **Monthly Weather Review**, v. 137, n. 5, p. 1705–1716, 2009. Available from: <<http://dx.doi.org/10.1175/2008MWR2659.1>>. 10, 12, 25, 72

_____. Adjoint sensitivity of the model forecast to data assimilation system error covariance parameters. **Quarterly Journal of the Royal Meteorological Society**, v. 136, n. 653, p. 2000–2012, 2010. Available from: <<http://dx.doi.org/10.1002/qj.693>>. 11

DEE, D. P.; BALMASEDA, M.; BALSAMO, G.; ENGELEN, R.; SIMMONS, A. J.; THÉPAUT, J. N. Toward a consistent reanalysis of the climate system. **Bulletin of the American Meteorological Society**, v. 95, n. 8, p. 1235–1248, 2013. Available from: <<http://dx.doi.org/10.1175/BAMS-D-13-00043.1>>. 2, 3, 41, 42

DEE, D. P.; UPPALA, S. Variational bias correction of satellite radiance data in the ERA-Interim reanalysis. **Quarterly Journal of the Royal Meteorological Society**, v. 135, n. 644, p. 1830–1841, 2009. Available from: <<https://doi.org/10.1002/qj.493>>. 39

DEE, D. P.; UPPALA, S. M.; SIMMONS, A. J.; BERRISFORD, P.; POLI, P.; KOBAYASHI, S.; ANDRAE, U.; BALMASEDA, M. A.; BALSAMO, G.; BAUER, P.; BECHTOLD, P.; BELJAARS, A. C. M.; BERG, L. van de; BIDLOT, J.; BORMANN, N.; DELSOL, C.; DRAGANI, R.; FUENTES, M.; GEER, A. J.; HAIMBERGER, L.; HEALY, S. B.; HERSBACH, H.; HÓLM, E. V.; ISAKSEN, L.; KÅLLBERG, P.; KÖHLER, M.; MATRICARDI, M.; MCNALLY, A. P.; MONGE-SANZ, B. M.; MORCRETTE, J. J.; PARK, B. K.; PEUBEY, C.; ROSNAY, P. de; TAVOLATO, C.; THÉPAUT, J. N.; VITART, F. The ERA-Interim reanalysis: configuration and performance of the data assimilation

system. **Quarterly Journal of the Royal Meteorological Society**, v. 137, n. 656, p. 553–597, 2011. Available from: <<http://dx.doi.org/10.1002/qj.828>>. 2, 39, 82

DERBER, J.; ROSATI, A. A global oceanic data assimilation system. **Journal of Physical Oceanography**, v. 19, n. 9, p. 1333–1347, 1989. Available from: <[http://dx.doi.org/10.1175/1520-0485\(1989\)019<1333:AGODAS>2.0.CO;2](http://dx.doi.org/10.1175/1520-0485(1989)019<1333:AGODAS>2.0.CO;2)>. 27

DERBER, J. C.; WU, W.-S. The use of TOVS cloud-cleared radiances in the NCEP SSI analysis system. **Monthly Weather Review**, v. 126, n. 8, p. 2287–2299, 1998. Available from: <[https://doi.org/10.1175/1520-0493\(1998\)126<2287:TUOTCC>2.0.CO;2](https://doi.org/10.1175/1520-0493(1998)126<2287:TUOTCC>2.0.CO;2)>. 23, 37, 61

DESROZIERS, G.; BERRE, L.; CHAPNIK, B.; POLI, P. Diagnosis of observation, background and analysis-error statistics in observation space. **Quarterly Journal of the Royal Meteorological Society**, v. 131, n. 613, p. 3385–3396, 2005. Available from: <<http://dx.doi.org/10.1256/qj.05.108>>. 58

DINIZ, F. L. R.; TODLING, R. Assessing the impact of observations in a multi-year Reanalysis (under minor review). **Quarterly Journal of the Royal Meteorological Society**, 2019. 7

_____. Forecast Sensitivity Observation Impact in a global Reanalysis. **JCSDA Quarterly Newsletter**, Spring, n. 63, p. 10–16, 2019. 7

DINIZ, F. L. R.; TODLING, R.; HERDIES, D. L. A brief assessment of the impact of nearly 40 years of assimilated observations over the Amazon basin (submitted). **Earth and Space Science**, 2019. 7

DONLON, C. J.; MARTIN, M.; STARK, J.; ROBERTS-JONES, J.; FIEDLER, E.; WIMMER, W. The operational sea surface temperature and sea ice analysis (OSTIA) system. **Remote Sensing of Environment**, v. 116, p. 140–158, 2012. Available from: <<http://www.sciencedirect.com/science/article/pii/S0034425711002197>>. 23

DRAPER, C. S.; REICHLER, R. H.; KOSTER, R. D. Assessment of MERRA-2 land surface energy flux estimates. **Journal of Climate**, v. 31, n. 2, p. 671–691, 2018. Available from: <<https://doi.org/10.1175/JCLI-D-17-0121.1>>. 22

EHRENDORFER, M. A review of issues in ensemble-based Kalman filtering. **Meteorologische Zeitschrift**, v. 16, n. 6, p. 795–818, 2007. Available from: <<http://dx.doi.org/10.1127/0941-2948/2007/0256>>. 47

EHRENDORFER, M.; ERRICO, R. M.; RAEDER, K. D. Singular-vector perturbation growth in a primitive equation model with moist physics. **Journal of the Atmospheric Sciences**, v. 56, n. 11, p. 1627–1648, 1999. Available from: <[http://dx.doi.org/10.1175/1520-0469\(1999\)056<1627:SVPGIA>2.0.CO;2](http://dx.doi.org/10.1175/1520-0469(1999)056<1627:SVPGIA>2.0.CO;2)>. 15

EL AKKRAOUI, A.; TRÉMOLET, Y.; TODLING, R. Preconditioning of variational data assimilation and the use of a bi-conjugate gradient method. **Quarterly Journal of the Royal Meteorological Society**, v. 139, n. 672, p. 731–741, 2013. Available from: <<http://dx.doi.org/10.1002/qj.1997>>. 23, 27

ERRICO, R. M. Interpretations of an adjoint-derived observational impact measure. **Tellus A**, v. 59, n. 2, p. 273–276, 2007. Available from: <<http://dx.doi.org/10.1111/j.1600-0870.2006.00217.x>>. xv, 10, 12, 17, 72

ERRICO, R. M.; GELARO, R.; NOVAKOVSKAIA, E.; TODLING, R. General characteristics of stratospheric singular vectors. **Meteorologische Zeitschrift**, v. 16, n. 6, p. 621–634, 2007. ISSN 0941-2948. Available from: <<https://www.ingentaconnect.com/content/schweiz/mz/2007/00000016/00000006/art00004>>. 16

ERRICO, R. M.; VUKICEVIC, T. Sensitivity analysis using an adjoint of the PSU-NCAR mesoseale model. **Monthly Weather Review**, v. 120, n. 8, p. 1644–1660, 1992. Available from: <[https://doi.org/10.1175/1520-0493\(1992\)120<1644:SAUAA0>2.0.CO;2](https://doi.org/10.1175/1520-0493(1992)120<1644:SAUAA0>2.0.CO;2)>. 5

GEER, A. J.; LONITZ, K.; WESTON, P.; KAZUMORI, M.; OKAMOTO, K.; ZHU, Y.; LIU, E. H.; COLLARD, A.; BELL, W.; MIGLIORINI, S.; CHAMBON, P.; FOURRIÉ, N.; KIM, M.; KÖPKEN-WATTS, C.; SCHRAFF, C. All-sky satellite data assimilation at operational weather forecasting centres. **Quarterly Journal of the Royal Meteorological Society**, v. 144, n. 713, p. 1191–1217, 2018. ISSN 0035-9009. Available from: <<https://doi.org/10.1002/qj.3202>>. 84

GELARO, R.; LANGLAND, R. H.; PELLERIN, S.; TODLING, R. The THORPEX observation impact intercomparison experiment. **Monthly Weather**

Review, v. 138, n. 11, p. 4009–4025, 2010. Available from:

<<http://dx.doi.org/10.1175/2010MWR3393.1>>. 19, 23, 43, 47, 52, 71

GELARO, R.; MCCARTY, W.; SUÁREZ, M. J.; TODLING, R.; MOLOD, A.; TAKACS, L.; RANDLES, C. A.; DARMENOV, A.; BOSILOVICH, M. G.; REICHLER, R.; WARGAN, K.; COY, L.; CULLATHER, R.; DRAPER, C.; AKELLA, S.; BUCHARD, V.; CONATY, A.; DA SILVA, A. M.; GU, W.; KIM, G.-K.; KOSTER, R.; LUCCHESI, R.; MERKOVA, D.; NIELSEN, J. E.; PARTYKA, G.; PAWSON, S.; PUTMAN, W. M.; RIENECKER, M.; SCHUBERT, S. D.; SIENKIEWICZ, M.; ZHAO, B. The modern-era retrospective analysis for research and applications, version 2 (MERRA-2). **Journal of Climate**, v. 30, n. 14, p. 5419–5454, 2017. Available from:

<<https://doi.org/10.1175/JCLI-D-16-0758.1>>. 22, 33, 39, 56, 78, 82

GELARO, R.; ZHU, Y. Examination of observation impacts derived from observing system experiments (OSEs) and adjoint models. **Tellus A**, v. 61, n. 2, p. 179–193, 2009. Available from:

<<http://dx.doi.org/10.1111/j.1600-0870.2008.00388.x>>. 10, 71, 86

GELARO, R.; ZHU, Y.; ERRICO, R. M. Examination of various-order adjoint-based approximations of observation impact. **Meteorologische Zeitschrift**, v. 16, n. 6, p. 685–692(8), 2007. Available from:

<<http://www.ingentaconnect.com/content/schweiz/mz/2007/00000016/00000006/art00010>>. Access in: 14 nov. 2012. 10

GRIMM, A. M.; DIAS, P. L. S. Analysis of tropical–extratropical interactions with influence functions of a barotropic model. **Journal of the Atmospheric Sciences**, v. 52, n. 20, p. 3538–3555, 1995. Available from:

<[https://doi.org/10.1175/1520-0469\(1995\)052<3538:AOTIWI>2.0.CO;2](https://doi.org/10.1175/1520-0469(1995)052<3538:AOTIWI>2.0.CO;2)>.

72

HAN, Y.; DELST, P. van; LIU, Q.; WENG, F.; YAN, B.; TREADON, R.; DERBER, J. **JCSDA community radiative transfer model (CRTM) – version 1**. Washington, DC, USA, 2006. Available from:

<<https://repository.library.noaa.gov/view/noaa/1157>>. 23

HEALY, S. B.; THÉPAUT, J.-N. Assimilation experiments with CHAMP GPS radio occultation measurements. **Quarterly Journal of the Royal Meteorological Society**, v. 132, n. 615, p. 605–623, 2006. ISSN 1477-870X.

Available from: <<http://dx.doi.org/10.1256/qj.04.182>>. 66

HOLDAWAY, D.; ERRICO, R.; GELARO, R.; KIM, J. G. Inclusion of linearized moist physics in NASA's Goddard Earth observing system data assimilation tools. **Monthly Weather Review**, v. 142, n. 1, p. 414–433, 2014. Available from: <<https://doi.org/10.1175/MWR-D-13-00193.1>>. 25, 27, 71

HORÁNYI, A. Some aspects on the use and impact of observations in the ERA5 Copernicus Climate Change Service reanalysis. **Időjárás – Quarterly Journal of the Hungarian Meteorological Service**, v. 121, n. 4, p. 329–344, 2017. 40, 52, 55, 64, 67, 94

ISHIBASHI, T. Tangent linear approximation based observation data impact estimation in 4d-var. **Quarterly Journal of the Royal Meteorological Society**, v. 137, n. 660, p. 1898–1912, 2011. Available from: <<http://dx.doi.org/10.1002/qj.871>>. 11

_____. Adjoint-based observation impact estimation with direct verification using forward calculation. **Monthly Weather Review**, v. 146, n. 9, p. 2837–2858, 2018. Available from: <<https://doi.org/10.1175/MWR-D-18-0037.1>>. 19

KALNAY, E.; OTA, Y.; MIYOSHI, T.; LIU, J. A simpler formulation of forecast sensitivity to observations: application to ensemble Kalman filters. **Tellus A**, v. 64, n. 1, p. 18462, 2012. ISSN 1600-0870. Available from: <<http://www.tellusa.net/index.php/tellusa/article/view/18462>>. 11, 13, 18

KLEIST, D. T.; PARRISH, D. F.; DERBER, J. C.; TREADON, R.; ERRICO, R. M.; YANG, R. Improving incremental balance in the GSI 3DVAR analysis system. **Monthly Weather Review**, v. 137, n. 3, p. 1046–1060, 2009. Available from: <<http://dx.doi.org/10.1175/2008MWR2623.1>>. 23

KLEIST, D. T.; PARRISH, D. F.; DERBER, J. C.; TREADON, R.; WU, W.-S.; LORD, S. Introduction of the GSI into the NCEP global data assimilation system. **Weather and Forecasting**, v. 24, n. 6, p. 1691–1705, 2009. Available from: <<http://dx.doi.org/10.1175/2009WAF2222201.1>>. 23

KLINKER, E.; RABIER, F.; KELLY, G.; MAHFOUF, J.-F. The ECMWF operational implementation of four-dimensional variational assimilation. III: experimental results and diagnostics with operational configuration. **Quarterly Journal of the Royal Meteorological Society**, v. 126, n. 564, p. 1191–1215, 2000. Available from: <<https://rmets.onlinelibrary.wiley.com/doi/abs/10.1002/qj.49712656417>>. 2

KOTSUKI, S.; KUROSAWA, K.; MIYOSHI, T. On the properties of ensemble forecast sensitivity to observations. **Quarterly Journal of the Royal Meteorological Society**, v. 145, n. 722, p. 1897–1914, 2019. Available from: <<https://rmets.onlinelibrary.wiley.com/doi/abs/10.1002/qj.3534>>. 72

LAFON, T.; FOWLER, J.; JIMÉNEZ, J. F.; CORDOBA, G. J. T. A viable alternative for conducting cost-effective daily atmospheric soundings in developing countries. **Bulletin of the American Meteorological Society**, v. 95, n. 6, p. 837–842, 2014. Available from: <<https://doi.org/10.1175/BAMS-D-13-00125.1>>. 93

LANGLAND, R.; AULIGNÉ, T.; GELARO, R.; MAHAJAN, R.; GROFF, D.; LIU, J.; COTTON, J.; MORGAN, L.; OTA, Y. Forecast sensitivity and observation impact (FSOI) inter-comparison experiment. In: INTERNATIONAL WINDS WORKSHOP (IWW-13), 13., 2016, Monterey, California, USA. **Proceedings...** Asilomar Conference Grounds, California, USA, 2016. 19

LANGLAND, R. H.; BAKER, N. L. Estimation of observation impact using the NRL atmospheric variational data assimilation adjoint system. **Tellus A**, v. 56, n. 3, p. 189–201, 2004. ISSN 1600-0870. Available from: <<http://dx.doi.org/10.1111/j.1600-0870.2004.00056.x>>. 5, 7, 10, 11, 12, 18, 19, 20, 25, 39, 40, 52, 71, 72, 91, 93

LEWIS, J.; LAKSHMIVARAHAN, S.; DHALL, S. **Dynamic data assimilation: a least squares approach**. 2. ed. [S.l.: s.n.], 2009. ISBN 9780521851558. 1

LI, H.; LIU, J.; KALNAY, E. Correction of ‘Estimating observation impact without adjoint model in an ensemble Kalman filter’. **Quarterly Journal of the Royal Meteorological Society**, v. 136, n. 651, p. 1652–1654, 2010. Available from: <<http://dx.doi.org/10.1002/qj.658>>. 11, 13

LIN, S.-J. A “vertically Lagrangian” finite-volume dynamical core for global models. **Monthly Weather Review**, v. 132, n. 10, p. 2293–2307, 2004. Available from: <[https://doi.org/10.1175/1520-0493\(2004\)132<2293:AVLFDC>2.0.CO;2](https://doi.org/10.1175/1520-0493(2004)132<2293:AVLFDC>2.0.CO;2)>. 22

LIU, J.; KALNAY, E. Estimating observation impact without adjoint model in an ensemble Kalman filter. **Quarterly Journal of the Royal Meteorological Society**, v. 134, n. 634, p. 1327–1335, 2008. Available from: <<http://dx.doi.org/10.1002/qj.280>>. 11, 13, 18

LONG, C. S.; FUJIWARA, M.; DAVIS, S.; MITCHELL, D. M.; WRIGHT, C. J. Climatology and interannual variability of dynamic variables in multiple reanalyses evaluated by the SPARC reanalysis intercomparison project (S-RIP).

Atmospheric Chemistry and Physics, v. 17, n. 23, p. 14593–14629, 2017.

Available from: <<https://www.atmos-chem-phys.net/17/14593/2017/>>. 56

LORENC, A. C.; MARRIOTT, R. T. Forecast sensitivity to observations in the Met Office global numerical weather prediction system. **Quarterly Journal of the Royal Meteorological Society**, v. 140, n. 678, p. 209–224, 2014. ISSN 1477-870X. Available from: <<http://dx.doi.org/10.1002/qj.2122>>. 19, 40, 52, 68, 69, 71

LORENZ, E. N. Energy and numerical weather prediction. **Tellus**, v. 12, n. 4, p. 364–373, 1960. ISSN 2153-3490. Available from:

<<https://doi.org/10.1111/j.2153-3490.1960.tb01323.x>>. 15

_____. A study of the predictability of a 28-variable atmospheric model. **Tellus A**, v. 17, n. 3, p. 321–333, 1965. Available from:

<<https://doi.org/10.3402/tellusa.v17i3.9076>>. 4

LUPU, C.; CARDINALI, C.; MCNALLY, A. P. Adjoint-based forecast sensitivity applied to observation-error variance tuning. **Quarterly Journal of the Royal Meteorological Society**, v. 141, n. 693, p. 3157–3165, 2015. ISSN 1477-870X.

Available from: <<https://doi.org/10.1002/qj.2599>>. 5, 11

LUPU, C.; GAUTHIER, P.; LAROCHE, S. Evaluation of the impact of observations on analyses in 3D- and 4D-Var based on information content.

Monthly Weather Review, v. 139, n. 3, p. 726–737, 2011. Available from:

<<https://doi.org/10.1175/2010MWR3404.1>>. 16, 40, 94

MAHAJAN, R.; GROFF, D.; AULIGNÉ, T.; GELARO, R.; HOLDAWAY, D.; MCCARTY, W.; LANGLAND, R.; BAKER, N.; COTTON, J.; MORGAN, L.; BARKER, D.; LORENC, A.; HOTTA, D.; OTA, Y.; ISHIBASHI, T.; MAHFOUF, J.-F.; DOERENBECHER, A.; RASPAUD, D. Forecast sensitivity - observation impact (FSOI) inter-comparison experiment. In: WORKSHOP ON SENSITIVITY ANALYSIS AND DATA ASSIMILATION IN METEOROLOGY AND OCEANOGRAPHY, 11., 2018, Aveiro, Portugal. **Proceedings...** Meliá Ria Hotel, Aveiro, Portugal, 2018. 19

MAHFOUF, J.-F.; RABIER, F. The ECMWF operational implementation of four-dimensional variational assimilation. II: experimental results with improved

physics. **Quarterly Journal of the Royal Meteorological Society**, v. 126, n. 564, p. 1171–1190, 2000. Available from: <<https://rmets.onlinelibrary.wiley.com/doi/abs/10.1002/qj.49712656416>>. 2

MAJUMDAR, S. J. A review of targeted observations. **Bulletin of the American Meteorological Society**, v. 97, n. 12, p. 2287–2303, 2016. Available from: <<http://dx.doi.org/10.1175/BAMS-D-14-00259.1>>. 4

MCCARTY, W.; COY, L.; GELARO, R.; HUANG, A.; MERKOVA, D.; SMITH, E. B.; SIENKIEWICZ, M.; WARGAN, K. **MERRA-2 Input observations: summary and assessment**. Greenbelt, MD, USA, 2016. xvi, 23, 24, 29, 31, 50, 52, 54, 75

MOLOD, A.; TAKACS, L.; SUAREZ, M.; BACMEISTER, J. Development of the GEOS-5 atmospheric general circulation model: evolution from MERRA to MERRA-2. **Geoscientific Model Development**, v. 8, n. 5, p. 1339–1356, 2015. Available from: <<https://www.geosci-model-dev.net/8/1339/2015/>>. 23

NASA's Scientific Visualization Studio. **Evolution of the meteorological observing system in the MERRA-2 reanalysis**. 12 2018. Available from: <<http://svs.gsfc.nasa.gov/4654>>. 29

National Research Council. **Four-dimensional model assimilation of data: a strategy for the Earth system sciences**. Washington, DC, USA: [s.n.], 1991. 88 p. ISBN 978-0-309-04536-0. Available from: <<https://www.nap.edu/catalog/1830/four-dimensional-model-assimilation-of-data-a-strategy-for-the>>. 71

NECKER, T.; WEISSMANN, M.; SOMMER, M. The importance of appropriate verification metrics for the assessment of observation impact in a convection-permitting modelling system. **Quarterly Journal of the Royal Meteorological Society**, v. 144, n. 714, p. 1667–1680, 2018. Available from: <<https://doi.org/10.1002/qj.3390>>. 72

OTA, Y.; DERBER, J.; KALNAY, E.; MIYOSHI, T. Ensemble-based observation impact estimates using the NCEP GFS. **Tellus A**, v. 65, n. 0, 2013. ISSN 1600-0870. Available from: <<http://www.tellusa.net/index.php/tellusa/article/view/20038>>. 19, 71

PAILLEUX, J. **First WMO workshop on the impact of various observing systems on numerical weather prediction**. World Meteorological

Organization, Geneva, Switzerland, 1997. v. 1. Available from:

www.wmo.int/pages/prog/www/documents.html>. 9

PAILLEUX, J.; ANDERSSON, E.; ONDRÁS, M. **Fourth WMO workshop on the impact of various observing systems on numerical weather**

prediction. World Meteorological Organization, Geneva, Switzerland, 2008. v. 4, 214 p. Available from: www.wmo.int/pages/prog/www/documents.html>. 9

PAILLEUX, J.; BÖTTGER, H. **Second WMO workshop on the impact of various observing systems on numerical weather prediction**. World

Meteorological Organization, Geneva, Switzerland, 2000. v. 2. Available from:

www.wmo.int/pages/prog/www/documents.html>. 9

PARRISH, D. F.; DERBER, J. C. The National Meteorological Center's spectral statistical-interpolation analysis system. **Monthly Weather Review**, v. 120,

n. 8, p. 1747–1763, 1992. Available from:

[https://doi.org/10.1175/1520-0493\(1992\)120<1747:TnMCSS>2.0.CO;2](https://doi.org/10.1175/1520-0493(1992)120<1747:TnMCSS>2.0.CO;2)>.

23

PUTMAN, W. M.; LIN, S.-J. Finite-volume transport on various cubed-sphere grids. **Journal of Computational Physics**, v. 227, n. 1, p. 55–78, 2007. ISSN

0021-9991. Available from: [http:](http://www.sciencedirect.com/science/article/pii/S0021999107003105)

www.sciencedirect.com/science/article/pii/S0021999107003105>. 22

RABIER, F. Overview of global data assimilation developments in numerical weather-prediction centres. **Quarterly Journal of the Royal Meteorological**

Society, v. 131, n. 613, p. 3215–3233, 2005. ISSN 1477-870X. Available from:

<http://dx.doi.org/10.1256/qj.05.129>>. 2

RABIER, F.; JÄRVINEN, H.; KLINKER, E.; MAHFOUF, J.-F.; SIMMONS, A. The ECMWF operational implementation of four-dimensional variational

assimilation. I: experimental results with simplified physics. **Quarterly Journal of the Royal Meteorological Society**, v. 126, n. 564, p. 1143–1170, 2000.

Available from: [https:](https://rmets.onlinelibrary.wiley.com/doi/abs/10.1002/qj.49712656415)

rmets.onlinelibrary.wiley.com/doi/abs/10.1002/qj.49712656415>. 2

RABIER, F.; KLINKER, E.; COURTIER, P.; HOLLINGSWORTH, A. Sensitivity of forecast errors to initial conditions. **Quarterly Journal of the Royal**

Meteorological Society, v. 122, n. 529, p. 121–150, 1996. Available from:

[https:](https://rmets.onlinelibrary.wiley.com/doi/abs/10.1002/qj.49712252906)

rmets.onlinelibrary.wiley.com/doi/abs/10.1002/qj.49712252906>. 5

RABIER, F.; MCNALLY, A.; ANDERSSON, E.; COURTIER, P.; UNDÉN, P.; EYRE, J.; HOLLINGSWORTH, A.; BOUTTIER, F. The ECMWF implementation of three-dimensional variational assimilation (3D-Var). II: structure functions. **Quarterly Journal of the Royal Meteorological Society**, v. 124, n. 550, p. 1809–1829, 1998. Available from: <<https://rmets.onlinelibrary.wiley.com/doi/abs/10.1002/qj.49712455003>>. 2

RANGLES, C. A.; DA SILVA, A. M.; BUCHARD, V.; DARMENOV, A.; COLARCO, P. R.; AQUILA, V.; BIAN, H.; NOWOTTNICK, E. P.; SMIRNOV, A.; YU, H.; GOVINDARAJU, R. **The MERRA-2 aerosol assimilation**. Greenbelt, MD, USA, 2016. 22

RANGLES, C. A.; DA SILVA, A. M.; BUCHARD, V.; COLARCO, P. R.; DARMENOV, A.; GOVINDARAJU, R.; SMIRNOV, A.; HOLBEN, B.; FERRARE, R.; HAIR, J.; SHINOZUKA, Y.; FLYNN, C. J. The MERRA-2 aerosol reanalysis, 1980 onward. Part I: system description and data assimilation evaluation. **Journal of Climate**, v. 30, n. 17, p. 6823–6850, 2017. Available from: <<https://doi.org/10.1175/JCLI-D-16-0609.1>>. 22

REICHLE, R. H.; DRAPER, C. S.; LIU, Q.; GIROTTO, M.; MAHANAMA, S. P. P.; KOSTER, R. D.; LANNOY, G. J. M. D. Assessment of MERRA-2 land surface hydrology estimates. **Journal of Climate**, v. 30, n. 8, p. 2937–2960, 2017. Available from: <<https://doi.org/10.1175/JCLI-D-16-0720.1>>. 22

REICHLE, R. H.; LIU, Q.; KOSTER, R. D.; DRAPER, C. S.; MAHANAMA, S. P. P.; PARTYKA, G. S. Land surface precipitation in MERRA-2. **Journal of Climate**, v. 30, n. 5, p. 1643–1664, 2017. Available from: <<https://doi.org/10.1175/JCLI-D-16-0570.1>>. 22

REYNOLDS, R. W.; SMITH, T. M.; LIU, C.; CHELTON, D. B.; CASEY, K. S.; SCHLAX, M. G. Daily high-resolution-blended analyses for sea surface temperature. **Journal of Climate**, v. 20, n. 22, p. 5473–5496, 2007. Available from: <<https://doi.org/10.1175/2007JCLI1824.1>>. 23

RIENECKER, M. M.; SUAREZ, M. J.; GELARO, R.; TODLING, R.; BACMEISTER, J.; LIU, E.; BOSILOVICH, M. G.; SCHUBERT, S. D.; TAKACS, L.; KIM, G.-K.; BLOOM, S.; CHEN, J.; COLLINS, D.; CONATY, A.; DA SILVA, A.; GU, W.; JOINER, J.; KOSTER, R. D.; LUCCHESI, R.; MOLOD, A.; OWENS, T.; PAWSON, S.; PEGION, P.; REDDER, C. R.; REICHLE, R.; ROBERTSON, F. R.; RUDDICK, A. G.; SIENKIEWICZ, M.; WOOLLEN, J.

MERRA: NASA's modern-era retrospective analysis for research and applications. **Journal of Climate**, v. 24, n. 14, p. 3624–3648, 2011. Available from: <<http://dx.doi.org/10.1175/JCLI-D-11-00015.1>>. 22, 37, 39

RIENECKER, M. M.; SUAREZ, M. J.; TODLING, R.; BACMEISTER, J.; TAKACS, L.; LIU, H.-C.; GU, W.; SIENKIEWICZ, M.; KOSTER, R. D.; GELARO, R.; STAJNER, I.; NIELSEN, J. E. **The GEOS-5 data assimilation system – documentation of versions 5.0.1 and 5.1.0, and 5.2.0**. Greenbelt, MD, USA, 2008. 21, 31, 54

SATO, Y.; RIISHOJGAARD, L. P. **Sixth WMO workshop on the impact of various observing systems on numerical weather prediction**. World Meteorological Organization, Geneva, Switzerland, 2016. v. 6, 26 p. Available from: <http://www.wmo.int/pages/prog/www/WIGOS-WIS/meetings/NWP-6_May2016_Shanghai/WMO6-Impact-workshop_Shanghai-May2016.html>. 9

SCHUBERT, S. D.; ROOD, R. B.; PFAENDTNER, J. An assimilated dataset for Earth science applications. **Bulletin of the American Meteorological Society**, v. 74, n. 12, p. 2331–2342, 1993. Available from: <[https://doi.org/10.1175/1520-0477\(1993\)074<2331:AADEFES>2.0.CO;2](https://doi.org/10.1175/1520-0477(1993)074<2331:AADEFES>2.0.CO;2)>. 22

SOMMER, M.; WEISSMANN, M. Ensemble-based approximation of observation impact using an observation-based verification metric. **Tellus A**, v. 68, n. 1, p. 27885, 2016. Available from: <<http://www.tandfonline.com/doi/abs/10.3402/tellusa.v68.27885>>. 72

TAKACS, L. L.; SUÁREZ, M. J.; TODLING, R. Maintaining atmospheric mass and water balance in reanalyses. **Quarterly Journal of the Royal Meteorological Society**, v. 142, n. 697, p. 1565–1573, 2016. ISSN 1477-870X. Available from: <<http://dx.doi.org/10.1002/qj.2763>>. 22, 37, 48

TALAGRAND, O. A study of the dynamics of four-dimensional data assimilation. **Tellus**, v. 33, n. 1, p. 43–60, 1981. Available from: <<http://dx.doi.org/10.1111/j.2153-3490.1981.tb01729.x>>. 15

THEURICH, G.; DELUCA, C.; CAMPBELL, T.; LIU, F.; SAINT, K.; VERTENSTEIN, M.; CHEN, J.; OEHMKE, R.; DOYLE, J.; WHITCOMB, T.; WALLCRAFT, A.; IREDELL, M.; BLACK, T.; SILVA, A. M. D.; CLUNE, T.; FERRARO, R.; LI, P.; KELLEY, M.; ALEINOV, I.; BALAJI, V.; ZADEH, N.; JACOB, R.; KIRTMAN, B.; GIRALDO, F.; MCCARREN, D.; SANDGATHE, S.;

PECKHAM, S.; IV, R. D. The earth system prediction suite: Toward a coordinated u.s. modeling capability. **Bulletin of the American Meteorological Society**, v. 97, n. 7, p. 1229–1247, 2016. Available from: <<http://dx.doi.org/10.1175/BAMS-D-14-00164.1>>. 21

TODLING, R. Comparing two approaches for assessing observation impact. **Monthly Weather Review**, v. 141, n. 5, p. 1484–1505, 2013. Available from: <<https://doi.org/10.1175/MWR-D-12-00100.1>>. xv, 11, 14, 16, 17, 18, 40, 47, 72, 94

TRÉMOLET, Y. First-order and higher-order approximations of observation impact. **Meteorologische Zeitschrift**, v. 16, n. 6, p. 693–694, 2007. Available from: <<http://dx.doi.org/10.1127/0941-2948/2007/0258>>. 10

_____. Computation of observation sensitivity and observation impact in incremental variational data assimilation. **Tellus A**, v. 60, n. 5, p. 964–978, 2008. Available from: <<http://dx.doi.org/10.1111/j.1600-0870.2008.00349.x>>. 10, 13, 27, 39, 40, 71, 91, 93

UPPALA, S. M.; KÅLLBERG, P. W.; SIMMONS, A. J.; ANDRAE, U.; BECHTOLD, V. D. C.; FIORINO, M.; GIBSON, J. K.; HASELER, J.; HERNANDEZ, A.; KELLY, G. A.; LI, X.; ONOGI, K.; SAARINEN, S.; SOKKA, N.; ALLAN, R. P.; ANDERSSON, E.; ARPE, K.; BALMASEDA, M. A.; BELJAARS, A. C. M.; BERG, L. V. D.; BIDLOT, J.; BORMANN, N.; CAIRES, S.; CHEVALLIER, F.; DETHOF, A.; DRAGOSAVAC, M.; FISHER, M.; FUENTES, M.; HAGEMANN, S.; HÓLM, E.; HOSKINS, B. J.; ISAKSEN, L.; JANSSEN, P. A. E. M.; JENNE, R.; MCNALLY, A. P.; MAHFOUF, J. F.; MORCRETTE, J. J.; RAYNER, N. A.; SAUNDERS, R. W.; SIMON, P.; STERL, A.; TRENBERTH, K. E.; UNTCH, A.; VASILJEVIC, D.; VITERBO, P.; WOOLLEN, J. The ERA-40 re-analysis. **Quarterly Journal of the Royal Meteorological Society**, v. 131, n. 612, p. 2961–3012, 2005. Available from: <<https://doi.org/10.1256/qj.04.176>>. 2

ZHU, Y.; GELARO, R. Observation sensitivity calculations using the adjoint of the Gridpoint Statistical Interpolation (GSI) analysis system. **Monthly Weather Review**, v. 136, n. 1, p. 335–351, 2008. Available from: <<http://dx.doi.org/10.1175/MWR3525.1>>. 10

PUBLICAÇÕES TÉCNICO-CIENTÍFICAS EDITADAS PELO INPE

Teses e Dissertações (TDI)

Teses e Dissertações apresentadas nos Cursos de Pós-Graduação do INPE.

Manuais Técnicos (MAN)

São publicações de caráter técnico que incluem normas, procedimentos, instruções e orientações.

Notas Técnico-Científicas (NTC)

Incluem resultados preliminares de pesquisa, descrição de equipamentos, descrição e ou documentação de programas de computador, descrição de sistemas e experimentos, apresentação de testes, dados, atlas, e documentação de projetos de engenharia.

Relatórios de Pesquisa (RPQ)

Reportam resultados ou progressos de pesquisas tanto de natureza técnica quanto científica, cujo nível seja compatível com o de uma publicação em periódico nacional ou internacional.

Propostas e Relatórios de Projetos (PRP)

São propostas de projetos técnico-científicos e relatórios de acompanhamento de projetos, atividades e convênios.

Publicações Didáticas (PUD)

Incluem apostilas, notas de aula e manuais didáticos.

Publicações Seriadas

São os seriados técnico-científicos: boletins, periódicos, anuários e anais de eventos (simpósios e congressos). Constam destas publicações o Internacional Standard Serial Number (ISSN), que é um código único e definitivo para identificação de títulos de seriados.

Programas de Computador (PDC)

São a seqüência de instruções ou códigos, expressos em uma linguagem de programação compilada ou interpretada, a ser executada por um computador para alcançar um determinado objetivo. Aceitam-se tanto programas fonte quanto os executáveis.

Pré-publicações (PRE)

Todos os artigos publicados em periódicos, anais e como capítulos de livros.